

## Ensemble classification methods for autism disordered speech

Zoubir Abdeslem Benselama <sup>a \*</sup>, Mohamed A. Bencherif <sup>b</sup>, Abderrezak Guessoum <sup>a</sup>, Mohamed A. Mekhtiche <sup>b</sup>

<sup>a</sup> Electronic Department, Saad Dahleb University, Blida(09000), Algeria.

<sup>b</sup> King Saud University, CS2R, Riyadh, Kingdom of Saudi Arabia.

### ARTICLE INFO

#### Article history :

Received March 2016

Accepted May 2016

#### Keywords :

Autism ;

Pathology ;

Speech disorder ;

Feature selection ;

Ensemble classifiers.

### ABSTRACT

In this paper, we present the results of our investigation on Autism classification by applying ensemble classifiers to disordered speech signals. The aim is to distinguish between Autism sub-classes by comparing an ensemble combining three decision methods, the sequential minimization optimization (SMO) algorithm, the random forests (RF), and the feature-subspace aggregating approach (Feating). The conducted experiments allowed a reduction of 30% of the feature space with an accuracy increase over the baseline of 8.66% in the development set and 6.62% in the test set.

©2016 LESI. All rights reserved.

## 1. Introduction

Autism is a term for a wide range of developmental brain disorders, called autism spectrum disorder (ASD) in the scientific community. The term spectrum refers to a collection of symptoms, skills, and levels of impairment or disability. Some individuals are impaired whilst others are severely disabled [1]. According to [2], ASD is sometimes called pervasive developmental disorder (PDD), and has been classified into five major classes :

1. Autistic disorder (classic autism)
2. Asperger's disorder (Asperger syndrome)
3. Pervasive developmental disorder not otherwise specified (PDD-NOS)
4. Rett's disorder (Rett syndrome)
5. Childhood disintegrative disorder (CDD).

The symptoms of ASD vary from one child to another, but can be classified into three areas :

\*Email : benselamaabd@hotmail.com

1. Social impairment
2. Communication difficulties
3. Repetitive and stereotyped behaviors.

In general, parents are the first to notice the abnormal behavior of their child. Sometimes ASD can be found in very young babies, when the infant starts focusing on fixed objects and fails to engage in play with his or her parents. Sometimes children behave normally until the age of two or three, at which point the symptoms of ASD appear, such as being silent, unsocial, indifferent, and displaying a loss of development (which is called regression).

Aiming to contribute to the early detection of speech impairments, many hospitals and speech departments have recorded speech databases in order to automatize the process of pathology detection and classification. Likewise, many research papers have also dealt with the detection of impaired speech, such as [3] and [4] on stigmatism classification, [5] on prosodic assessment of language impaired children, and [6] on automatic classification.

The need to investigate using computerized automatic methods requires assessed recorded pathological databases. For this autism related work, the Child Pathological Speech Database (CPSD) has been used; this database was recorded in two university departments (pediatrics and psychiatry) in Paris, France. The first is located at the “Université de Pierre et Marie Curie/Pitié Salpêtrière Hospital, while the second department belongs to the Université Rene Descartes/Necker Hospital.

The database consists of 99 children aged from 7 to 19 years and of both genders. The pathological database has been segmented into two main classes, defined as typical and atypical autism, and a second deep segmentation includes PDD, Dysphasia (DYS), and Not-Otherwise Specified (NOS). The set of distributed recorded files is presented in Table 1. [7].

**Table 1** – CPSD pathological speech database distribution.

	Autism	Train	Dev.	Test	Total
Typical (TYP)	TYP	566	543	542	1651
Atypical (ATY)	PDD	104	104	99	307
	NOS	104	68	75	247
	DYS	129	104	104	337
	Total	903	819	820	2542

In section 2, we will describe the classification methods, and section 3 presents the feature selection scheme. The implementations and results are described in section 4, which is followed by a discussion in section 5, before the paper concludes.

## 2. Classification methodology

Classifiers have the ability to split the space of features into low-level boundary spaces, thus allowing an expert decision of the probability of a feature vector belonging to one

or more subspaces. The error in the decision is more related to the correlation of the feature space and the overlap between the sub/spaces; in this order of idea, the use of multiple experts improves the “point of view” of the decision and lowers the probability of belonging to more than one space. Many classifiers, such as support vector machines and decision trees, can show exceptional results on some datasets and very low accuracies on others. In this conjecture, using different voters can handle the disparity between the classifiers; the better approach is to have an expert for each subspace or class. Unfortunately, with the increasing number of classes and problems, other decision methods have to be implemented.

In this paper we have opted for strong and weak classifiers, and experiments showed that by a tuned voting principle, the overall accuracy is better than each classifier alone.

### 2.1. Sequential minimization optimization (SMO) algorithm

The John Platt’s SMO algorithm for training a support vector classifier has been investigated in the pathological or emotional context [7]. The support vector machines have tremendously shown their ability to use intrinsically high dimensional hyper-planes to separate classes using binary splits. In such situations, the problem is to find a solution to the optimization equation [8]

$$\min_{w,b,\xi} \left\{ \frac{1}{2} \|w\|^2 + C \cdot \sum_i \xi_i \right\} \quad (1)$$

under the constraints defined by :

$$l_i (w \cdot x_i - b) \geq 1 - \xi_i, \quad 1 \leq i \leq n, \quad \xi_i \geq 0 \quad (2)$$

where C is the penalty for mislabeled examples and n the number of training files within the dataset. Once the model is built, it can be generalized to the development and test sets.

In our experiments, a polynomial kernel of degree one was used, as shown in equation 3.

$$K(x, y) = \langle x, y \rangle \quad (3)$$

### 2.2. Random Forest (RF)

In [9], Breiman proposed a variant of bagging called random forests (RF), which is an ensemble of decision trees built upon independent and identically distributed random vectors induced in a growing decision tree. Each tree uses a set of m features selected from the whole set of features, and grows until convergence. The sub-trees use an ensemble technique to decide on the class of the new instance.

The RF model in [10] is a predictor of a set of regression trees  $r_n\{X, \Theta_m, D_n, m \geq 1\}$ , where X are the random variables, and the  $\Theta_i, i = 1...m$  are i.i.d. outputs issued from a randomized variable  $\Theta$ . The set of trees are then aggregated or combined to form the regression estimation defined as :

$$\bar{r}_n(X, D_n) = E_{\Theta} [r_n(X, \Theta_m, D_n)] \tag{4}$$

where  $E_{\Theta}$  is the expected value of the random parameter  $X$  and the data  $D_n$ .

Each individual random tree will be built in the following manner :

At each node, a coordinate of  $X$ , from the  $d$  dimension vector is selected, with the  $k$ -th feature having a probability  $p_{n,k}$  of being selected. Once the coordinate is chosen, a division or split is initiated at the midpoint of the selected side.

The randomized tree  $r_n(X, \Theta_m, D_n)$  generates the output for which the corresponding vector  $X_i$  falls within the same cluster of the random partition as  $X$ .

Each individual tree will contain approximately  $k_n$  terminal nodes and each single leaf will have a Lebesgue measure of  $1/k_n$ . If  $X$  has a uniform distribution on the interval  $[0, 1]^d$ , it will result in  $n/k_n$  observations per terminal node.

### 2.3. Feature subspace aggregating ('Feating')

The technique is itself an ensemble approach [11]; it is a generic concept that can enhance the predictive performance of learners, and it is a generalized form of the Average One-Dependence Estimators (AODE) method. It uses a local model rather than a global one, and is formed by splitting the feature sub-space into non-overlapping local regions and ensuring that different subdivisions provide the distinct local neighborhoods for each point in the feature space. The problem is tackled by [11] in the way that solving a small aggregated problem is easier than solving a global problem.

The proposed feature-subspaces, issued from exhaustive subdivisions, are the backbone of an ensemble method that groups or aggregates all the sub-models known as local models, or a randomized part of them.

The feating is based on the following algorithm 1 :

**Algorithm 1 :** Feating ( $D, A, h$ )

– Build a set of Level Trees based on Feating

**INPUT D :** Training set,  $A$  : Set of given attributes,  $h$  : Maximum Level Tree

**OUTPUT E :** Collection of Level Trees

$E \leftarrow$  Start by an empty tree,  $n \leftarrow |A|$  /\* Number of features.

$N \leftarrow C_n^h$ ,  $P \leftarrow \text{rankAttribute}(A)$ ,

for  $i = 1$  to  $N$  do /\* Construct an attribute list from  $P$  based on index  $i$  \*/

$L \leftarrow \text{attributeList}(P, i)$ ,

$E \leftarrow E \cup \text{BuildLevelTree}(D, L, 0)$ ,

end for

Return  $E$

The feating technique has two main advantages :

- Decreases the execution time as the level of localization is increased
- Best fit for large data size as in our case.

### 2.4. Voting techniques

In decision theory, combining classifiers rests on two main schemes :

- a- Use of optimal (sub-optimal) basic classifiers.
- b- Use of strong combination rules.

Many classifiers pretend good accuracies over the training data, essentially due to large training data and repeated training sessions, leading unfortunately to a limited generalization process over newer test data. In order to avoid this type of problem, let us start with the assumption that each classifier uses a dissimilar approach to tackle the training data. The decision will be “classifier dependent” and tends to be more favorable to part of the data rather than to the other parts. Thus, adding different classifiers or expert decision makers will improve the decision, under the constraint of having strong combining rules : “The use of combination of multiple classifiers was demonstrated to be effective, under some conditions, for several pattern recognition applications” [12].

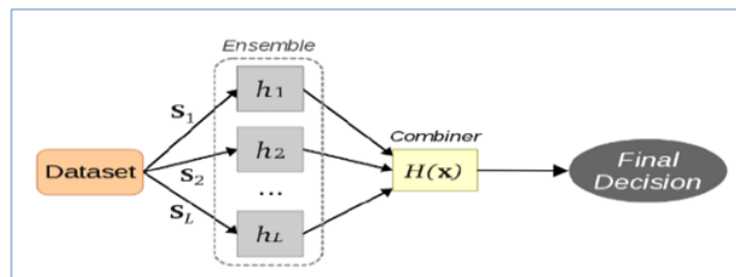


**Fig. 1** – Ensemble selection in a parallel scheme.

Fixed rules such as majority vote, minimum, and maximum probability rules have been tested and show performance increase in the development set. The majority rule encompasses that classifiers can decide on an autism case in a majoritarian manner, and there are cases where the majority vote [12] can lead to a decrease of the overall accuracy; the highest probability supposes that an expert per class can win. Other rules are also listed in the experiment tables, but they fluctuate between majority and maximum probabilities.

### 3. Features

The different speech features have been generated from the opensmile software [13]. The precompiled configurations included in the software contain different combinations of features, as in the proposed TUM baseline [7]. These features follow the Attribute Relation File Format (ARFF) and can be used in the Weka data mining java platform [14].

The predefined speech features are also called low-level descriptors (LLD), as they describe the basic features of speech such as the MFCC, the LPC, the ZCR, and the voice probability. All the LLD parameters are shown in Table 2.

**Table 2** – Speech low-level descriptors (LLD).

<b>LLD</b>	<b>Process / parameters</b>	<b>Qty.</b>
Log Energy	After Hamming windowing and pre-emphasis (0.97)	1
MFCC 0-12	Pre-emphasis 0.97, Ham. window	13
Critical band spectrum	Over 26bands	26
Zero crossing Rate	Frames of 25ms,10ms overlap	1
Voice Probability		1
F0	F0+F0envelope	2
Spectral band energies	[0-250], [0-650],[250-650], [1000-4000][3010-9123]	5
Spectral	Roll-Off Point 25 , 50, 75,90	4
Spectral Flux	Over successive frames	1
Spectrum	Spectral Centroid, Max, Min, Energy	4
Total		58

The LLD parameters are smoothed by a moving average filter of length three before being sent to a regression module, in order to compute the delta regression coefficients from the data contour. Then, statistical functional methods are applied, and the total number of coefficients is computed as follows :  $(58 \text{ LLD} + 58 \text{ DELTA\_LLD}) * 39 \text{ Functionals} = 4524$ , as presented in Table 3.

**Table 3** – LLD Functionals.

<b>Functionals</b>	<b>Type</b>	<b>Qty.</b>
Extremes	Max position, min position, amplitude, norm per frame	5
Regression	Linear regression coefficients, centroid, quadratic error, quadratic regression	9
Moments	Variance, std. dev., skewness, kurtosis,	5
Percentiles	Quartiles, inter quartile, percentile (0.95, 0.98)	8
Crossings	Zero crossing rate	1
Peaks	Number of peaks, mean peak distance.	4
Means	Mean, abs. mean, non-zero mean, non-zero geometric mean	7
Total		39

A detailed view of the spanning features is presented in Fig. 2., where the input wave file is fed to different blocks such as framing and vector emphasizing. Then, all the data are collected into a smoother and a regression module, and finally all types of functionals are generated and output to Weka.

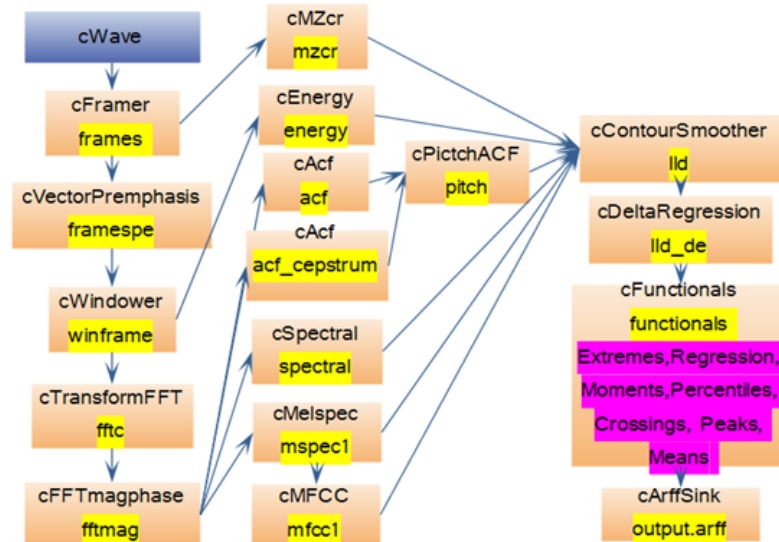


Fig. 2 – Selected features flowchart computation.

#### 4. Experimentation

In all the following experiments, three datasets are used. The train and development datasets have known classes while the test set has unknown classes, and the TUM website generates the accuracy of the test set for each of our models.

As an initial baseline investigation, the SMO has been adopted, with penalty parameters ranging from 0.0001 to 0.15, with different opensmile speech configurations, as illustrated in Fig. 4.

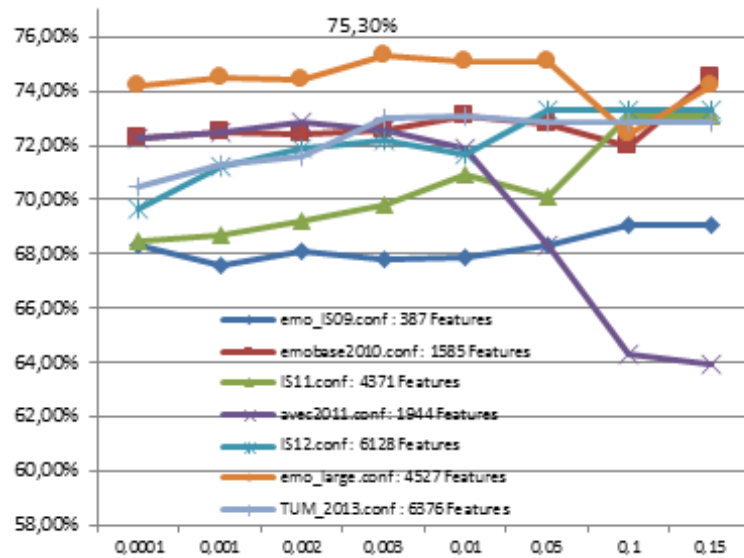


Fig. 3 – SMO recognition accuracies for the autism-diagnosis using different speech configurations.

The SMO best per-class results are shown in Table 4.

**Table 4** – SMO development set results.

	DYS	NOS	PDD	TYP	Sum
DYS	71	6	16	11	104
NOS	12	16	17	23	68
PDD	25	30	34	15	84
TYP	3	14	30	496	543
Autism (Diagnosis) total accuracy = 75.34%					

The same SMO model has been applied to the test set, giving an accuracy of 75.61%, with an increase of 5.81% over the TUM baseline, as presented in Table 5.

**Table 5** – Test set results using SMO.

	DYS	NOS	PDD	TYP	Sum
DYS	38	4	35	27	104
NOS	0	37	9	29	75
PDD	24	17	25	33	99
TYP	3	7	12	250	542
Autism (Diagnosis) total accuracy = 75.61%					

The different classifiers (SMO, RF, and Feating) have been trained and tested independently and then embedded in a vote module, as shown in Fig. 6. Let us remark that the classifiers have been added to the vote process incrementally. In order to see the effect of incremental vote process, the development results of the SMO-RF are presented in Table 6.

**Table 6** – Classification scheme using the vote process on the development set (819 instances).

	Development set							
	Single classifiers		Ensemble voting classifiers					
	SMO	RF	Maj. Vote	Avg. Prob.	Maj. vote	Product Prob.	Min prob.	Max prob.
Correctly classified	629	600	612	632	611	630	619	641
Incorrectly classified	190	219	207	187	208	189	200	178
Kappa statistic	0.546	0.390	0.471	0.515	0.468	0.507	0.476	0.546
Mean absolute error	0.281	0.211	0.1264	0.2462	0.127	0.163	0.208	0.264
Accuracy (%)	76.80	73.26	74.72	<b>77.16</b>	74.60	76.92	75.58	<b>78.26</b>

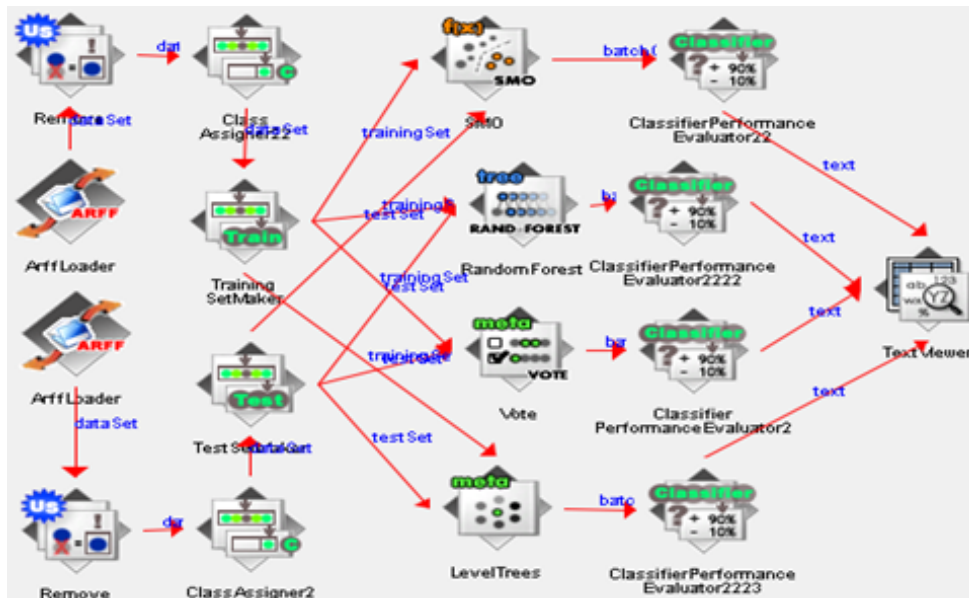


Fig. 4 – WEKA Knowledge flow voting process.

Further additional investigation on the optimization of the SMO classifier has led to an accuracy of 76.8% for the development set. The voting with average and maximum probabilities improved the best accuracy by 0.36% and 1.46%, respectively, as presented in Table 6.

Adding the Level-Trees classifier to the vote process, noted as “SMO-RF-Feating,” provided the results presented in Table 7. (development and test sets).

Table 7 – Development / test sets autism classification results (Baseline accuracy : 69.8%).

	SMO		Vote(max prob.) SMO-RF		Feating		Vote : (max.prob.) SMO/RF/ Feating	
	devel.	test	devel.	test	devel.	test	devel.	test
Classified Instances	616	620	641	616	629	625	627	615
Correctly	616	620	641	616	629	625	627	615
Incorrectly	203	200	178	204	190	195	192	205
Accuracy (%)	75.3	75.60*	78.26	75.12*	76.80	76.22*	76.55	75.00*
*Test results have been generated from the TUM website [7]								

## 5. Discussion of the results

The autism TUM-baseline [7] was developed on the basis of an SMO, with a per class up-sampling of the instances, using 6,374 attributes. The set of features was built using two framing techniques (20ms and 60ms), as presented in [7].

The TUM2013 proposed set of features, including the 60ms pitch based on the Gaussian window, the regression coefficients, and the subsequent functional coefficients, did not contribute to the autism classification. Instead, they mislead the SMO in some classes

and kept the accuracy around 69.8%, while using our proposed set of features, but by removing redundant and non-useful features, the accuracy increased by 5.80% (test set) via the SMO algorithm and by 6.42% (test set) through the feating technique.

The vote between the different classifiers improved the development results, but did not improve the test results. This is mainly due to the high similarity of the instances and the difficulties that human experts had in the manual recognition of the classes.

## 6. Conclusion

In this paper, we focused on a two-fold process. The first fold deals with the feature selection scheme in order to illustrate and determine the features that contribute to the autism classification, whilst the second fold concerns the vote between three different classifiers : the SMO, the RF, and the feating (Level Trees) techniques.

The final space of features decreased by 30% compared with the proposed one, with an increase of 6.42% in the classification accuracy. The vote by majority and max probability has shown good results for the SMO-Random Forest vote classifier, but decreased the overall classification by the use of the three classifiers.

The feating technique showed the best results because it is intrinsically an ensemble method, where the sublevel trees vote depends on sub-space ranked features.

The autism classification can be improved by further work on specialized autism features, and a weighted or fuzzy vote between the SMO and the feating technique.

## Acknowledgements

This project was supported by NSTIP strategic technologies programs, number (12-MED2474-02) in the Kingdom of Saudi Arabia

## REFERENCES

- [1] National Institute of mental health, publication n°.11-5511 2011. “A Parent’s Guide to Autism Spectrum Disorder”.2011.
- [2] American Psychiatric Association. “Diagnostic and Statistical Manual of Mental Disorders”, Fourth Edition - Text Revision (DSM-IV-TR).
- [3] Benselama Z., Guerti M., and Bencherif M., 2007. “Arabic speech pathology therapy computer aided system,” J. of Computer Science, vol. 3, no. 9, pp. 685–692.
- [4] Valentini-Botinhao C., Degenkolb-Weyers S., Maier A., Noeth E., Eysholdt U., and T. Bocklet. 2012. Automatic detection of sigmatism in children. In Proc. WOCCI, Portland, USA, pp. 1-4.
- [5] Ringeval F., Demouy J., Szasz’ak G., Chetouani M., Robel L., Xavier J., Cohen D., and Plaza M., 2011., “Automatic intonation recognition for the prosodic assessment of language impaired children,” IEEE Transactions on Audio, Speech & Language Processing, vol. 19, pp. 1328–1342,
- [6] Emily T. Prud’hommeaux, Brian Roark, Lois M. Black, Jan van Santen. 2011. Classification of atypical language in autism. In Proceedings of the 2nd Workshop on Cognitive Modeling and Computational Linguistics (CMCL), 88-96.
- [7] Schuller B., Steidl S., Batliner A., Vinciarelli A., Scherer K., Ringeval F., Chetouani

- M., Weninger F., Eyben F., Marchi E., Mortillaro M., Salamin H., Polychroniou A., Valente F., Kim S. 2013. : “The Interspeech 2013 Computational Paralinguistics Challenge : Social Signals, Conflict, Emotion, Autism”, Proc. Interspeech 2013, ISCA, Lyon, France.
- [8] Tomas Pfister, Peter Robinson., 2010. “Speech emotion classification and public speaking skill assessment”, Workshop on Human Behaviour Understanding, International Conference on Pattern Recognition, Istanbul, Turkey, August
- [9] Breiman L., 2001. “Random forests”, Machine Learning Journal, Vol., 45 :5-32,
- [10] Kai Ming Ting, Jonathan R. Wells, Swee Chuan Tan, Shyh Wei Teng, 2011. "Feature-subspace aggregating : ensembles for stable and unstable learners", Machine Learning Vol.82, pp :375–397,
- [11] Ponti, M.P., 2011 "Combining Classifiers : From the Creation of Ensembles to the Decision Fusion" Conference on Graphics, Patterns and Images Tutorials (SIBGRAPI-T), 2011 24th SIBGRAPI, vol., no., pp. 1,10, 28-30., DOI : 10.1109/SIBGRAPI-T.2011.9.
- [12] Ludmila I. Kuncheva, 2004. “Combining Pattern Classifiers : Methods and Algorithms”, Wiley Editions,
- [13] Florian Eyben, Martin Wöllmer, Björn Schuller : "openSMILE - The Munich Versatile and Fast Open-Source Audio Feature Extractor", Proc. ACM Multimedia (MM), ACM, Florence, Italy, ISBN 978-1-60558-933-6, pp. 1459-1462, 25.-29.10.2010.
- [14] Mark Hall, Eibe Frank, Geoffrey Holmes, Bernhard Pfahringer, Peter Reutemann, Ian H. Witten (2009) ; The WEKA Data Mining Software : An Update ; SIGKDD Explorations, Volume 11, Issue 1.

# Electromagnetic Comparison of 3-, 5- and 7-phases Permanent-Magnet Synchronous Machines : Mild Hybrid Traction Application

D. Ouamara <sup>a, b \*</sup>, F. Dubas <sup>a †</sup>, S.A. Randi <sup>c</sup>, M.N. Benallal <sup>b</sup>, C.  
Espanet <sup>d</sup>

<sup>a</sup> ENERGY Department, FEMTO-ST Institute, UMR CNRS 6174, UBFC, Belfort, France

<sup>b</sup> LESI Laboratory, University Djilali Bounaama of Khemis Miliana, Algeria

<sup>c</sup> Renault S.A., Guyanourt, France

<sup>d</sup> UBFC, Belfort, France

## ARTICLE INFO

### Article history :

Received July 2016

Accepted September 2016

### Keywords :

Energy balance ;

Harmonic analysis ;

Numerical ;

Permanent-magnet ;

Synchronous Machines ;

Star of slots.

## ABSTRACT

Authors compare the electromagnetic performances of three multi-phases permanent-magnet (PM) synchronous machines (PMSM) for Mild Hybrid-traction application. This comparison was made using two-dimensional (2-D) numerical simulations in transient magnetic with eddy-current reaction field in the PMs. The best machine was determined using an energetic analysis (i.e., losses, torque and efficiency) according specifications. In this study, the non-overlapping winding with double layer (i.e. all teeth wound type) was used. The winding synthesis is based on the "Star of slots" method as well as the Fourier series decomposition of the magnetomotive force (MMF).

©2016 LESI. All rights reserved.

## 1. Introduction

The humanity energy consumption has generally been growing. The latter is accompanied by emission of greenhouse gases. In this context, the automotive sector, which represents about a third part of the overall world energy consumption, may well evolve to become a contributor to reduction of emissions by developing and selling hybrid vehicles. Depending on the degree of hybridization, which corresponds to the quantity of power that can provide the electrical energy source compared to fossil energy source, different types of drive have been developed [1] :

- Full Hybrid : combination of a combustion engine and an electric motor, the latter

\*Email : daoud.ouamara@gmail.com

†Email : Fdubas@gmail.com

provide a power more than 30 % of the total power. The electric motor is rather used for low-speed operation, while the combustion engine is used at high-speed.

- Mild Hybrid :the part of electric motor is between 10 % and 30 % of the total power. This version is equipped by a kinetic energy recovery system, consisting of electrical machine in the generator operating mode. Contrary to the Full Hybrid, the electric motor is only used to assist the vehicle during the acceleration phases.
- Micro Hybrid :it is not strictly a hybrid. Known as "Stop & Start",it ensures a modest electric energy consumption and reduction of CO2 emissions. At stop, the combustion engine shuts down and restart when the accelerator is pushed. The electric part is less than 10 % of the total power.

In this article, we are considering only electric motorization of Mild Hybrid powertrain.

The studied electrical machines are multi-phases (3-phases included) surface-mounted PMSM with concentrated all teeth wound (two layers) winding. This topology of machines is assumed to be a good candidate for this kind of application : good torque density, lower maintenance costs, and simple construction . . . [2-3]. In addition to advantages associated to this structure, the multi-phase system ensure operation in degraded mode if phase's number is greater than 3, which is a powerful asset in automotive traction [4-7]. The comparison via an energy balance will be carry out considering three electrical machines :

- **Machine A** : 12-slots/10-poles/3-phases ;
- **Machine B** : 20-slots/18-poles/5-phases ;
- **Machine C** : 28-slots/26-poles/7-phases.

**Machine A** is well known in literature [8]. From this topology, **Machine B** and **Machine C** are deduced. It should be noted that **Machine B** was studied in [9]. The comparative study of those machines will be subdivided into two parts, namely :

- The winding analysis based on the "Star of slots" method as well as the Fourier series decomposition : winding distribution, MMF waveform and winding factor ;
- and the electromagnetic numerical modeling, viz., electromagnetic torque, torque ripple, back electromotive force (EMF), in order to compare the machines via an energy balance (i.e., iron/copper/PMs losses and efficiency).

The terms of reference for this comparative study are :

- Identical mass ;
- Dimension :  $D_{ex} = 138.4 \text{ mm}$  and  $L_z = 136 \text{ mm}$  ;
- Rotating speed : 3,000 rpm.

## 2. Winding Synthesis

Fig. 1 represents the topology of the machines and the spatial distribution of various phases. The phases of winding are star-connected and the studied machines are supplied by sinusoidal current. The direction of PMs magnetization is supposed to be radial.

Machines that have  $2p = N_d \pm 2$  (where  $p$  and  $N_d$  are respectively the pole pairs and slots number) are generally characterized by low detent torque [10]. Consequently, the number of poles chosen is : 18 poles for **Machine B** (with 20 teeth) and 26 poles for **Machine C** (with 28 teeth).

In order to synthesize a winding with higher performances, the "star of slots" method

is used [11-12]. The phases distribution of the machines via this method is defined on Fig. 2.

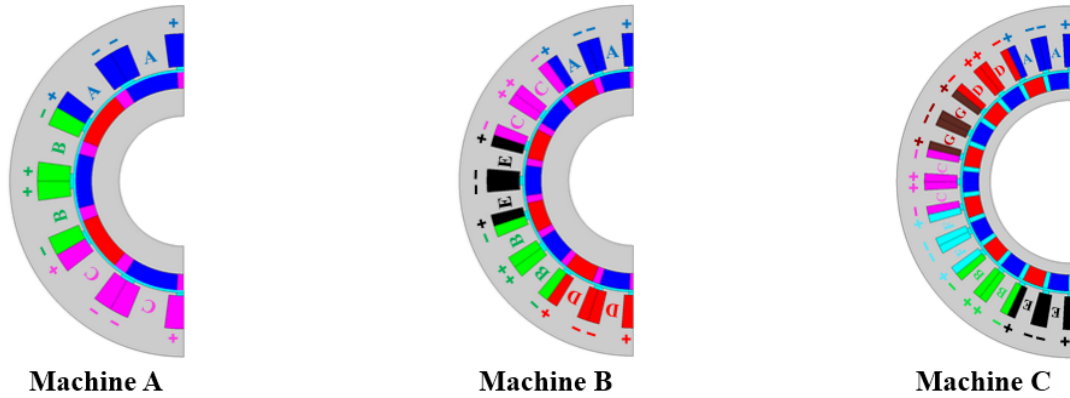


Fig. 1 – Description of machines : Topology & Winding distribution.

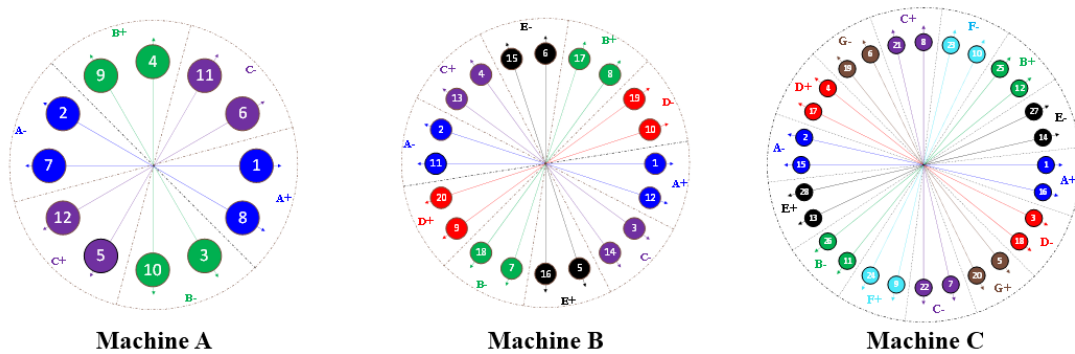
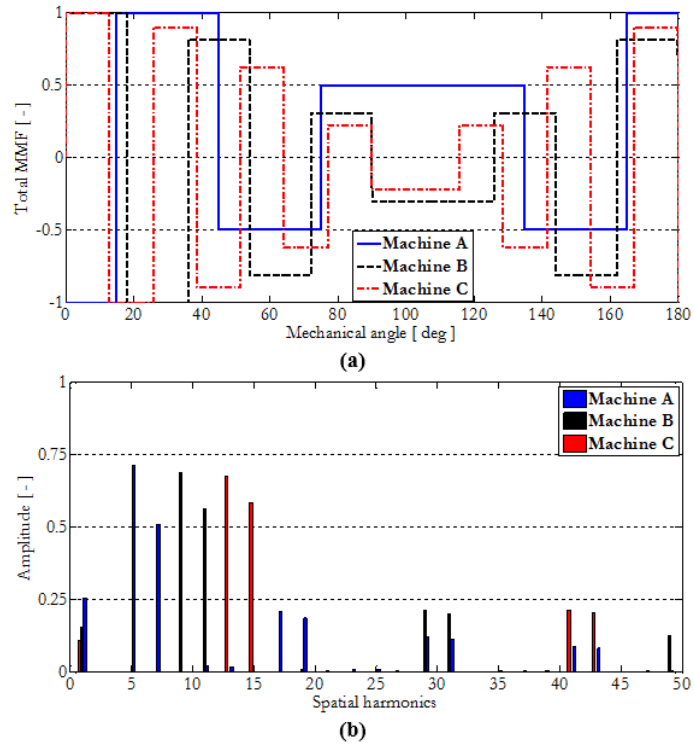
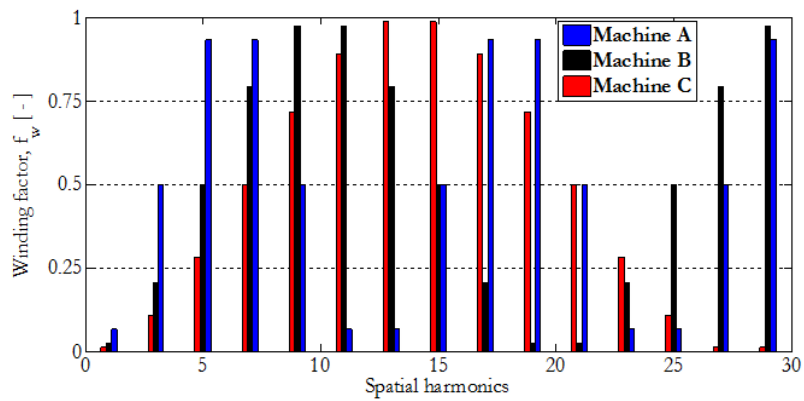


Fig. 2 – Distribution of phases via the "Star of slots" method.

Fig. 3 shows the pattern of total MMF [see Fig. 3(a)] and its corresponding harmonic spectrum [see Fig. 3(b)] of the two layers concentrated winding of the machines. Spatial harmonics spectrum shows the 5th harmonic order is higher than fundamental for the **Machine A**, 9<sup>th</sup> for the **Machine B** and 13th for the **Machine C** that confirms our choice about poles number of machines studied.



**Fig. 3** – Total MMF : (a) Waveform and (b) Harmonic spectrum.



**Fig. 4** – Winding factor.

Another element of significant importance is the winding factor, and it will be calculated. The calculation of this latter will be done by comparing MMF harmonics of the studied winding [see Fig. 1], by Fourier series decomposition, with harmonics of the diametric winding associated. Fourier series decomposition of studied and diametric winding is given by :

$$\varepsilon = \sum_{k=1}^{\infty} \frac{NI}{k\pi} \cdot A_k^* \cdot \cos(k \cdot \theta) \quad (1)$$

with  $N$  the number of turns,  $I$  the RMS current, and

$$A_k^e = \sin\left(\beta^+ \cdot \frac{k\pi}{2}\right) + \sin\left(\beta^- \cdot \frac{k\pi}{2}\right) - 2\sin\left(\frac{k\pi}{2}\right) \quad (2)$$

for the studied winding with  $\beta^\pm = ((m \pm 1))/m$  where  $m$  is the number of phases, and

$$A_k^d = 2 \cdot \left\{ 1 - \sin\left[(1 - 2k) \cdot \frac{\pi}{2}\right] \right\} \quad (3)$$

for the diametric winding.

The winding factor is calculated by  $f_w = |A_k^e| / |A_k^d|$  (estimated between 0 and 1) and results of calculation are given on Fig. 4; whose winding factor is equal to 0.933 for **Machine A**, 0.9875 for **Machine B**, and 0.9755 for **Machine C**. Even harmonics have a winding factor null. The periodicity of the winding factor is equal to  $N_d$  for the studied machines [see Fig. 4].

In conclusion of this part, the choice of poles number of studied machines is consistent with obtained results. The 5<sup>th</sup>, 9<sup>th</sup> and 13<sup>th</sup> harmonics order of **Machine A**, **Machine B** and **Machine C** respectively, are characterized by higher amplitudes in Fourier series decomposition of MMF and by higher winding factor. Notice that we could have also chosen 7 pole pairs for **Machine A**, 11 pole pairs for **Machine B** and 15 pole pairs for **Machine C**. In order to have a lower frequency, the first choice was selected for the comparative study.

### 3. 2-D Numerical Simulation

The comparison via an energy balance is performed using 2-D numerical simulations in transient magnetic with taken into account eddy-current reaction field in the PMs[13]. For the studied machines, the magnetic steel M270-35A of Arcelor Mittal has been considered. The PMs type is N37H whose remanent flux density is equal to 1.1 T at 100 °C. No-load/Load simulations will determine the back EMF, the electromagnetic torque as well as the torque ripple, the iron/copper/PMs losses and the efficiency.

Fig. 5 represents the distribution map of magnetic flux densities in the three machines. It should be noticed that the maximum value of magnetic flux density in the teeth reach 1.6 T for **Machine A**, 1.4 T for **Machine B**, and 1.2 T for **Machine C**; while in the tooth-tips, the magnetic material is saturated. It is due to the fact that surface tip is not large.

Fig. 6 shows the electromagnetic torque and torque ripple for the three machines. Considering weakness of torque ripple, the cogging torque is neglected. The mean value of electromagnetic torque is 71.5 Nm, what satisfy the requirements specification. The torque ripple rate is defined by

$$\Delta T_{em} (\%) = \frac{T_{em_{max}} - T_{em_{min}}}{T_{em_{moy}}} \times 100 \quad (4)$$

It should be noted that ripple value is less than 1 % for Machine B and Machine C.

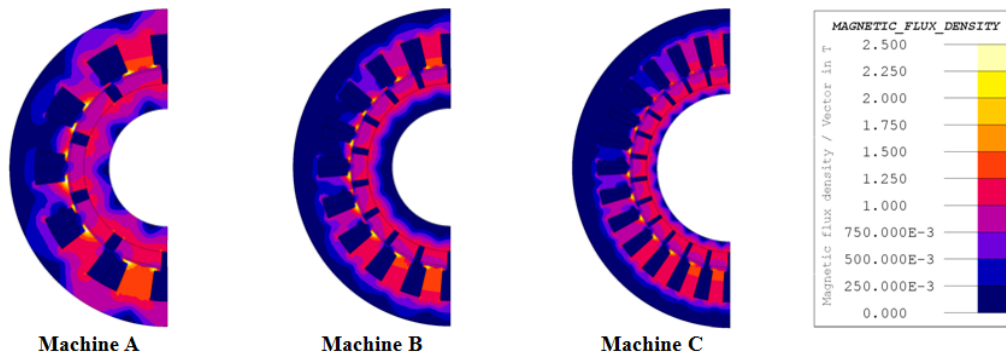


Fig. 5 – Distribution map of magnetic flux densities.

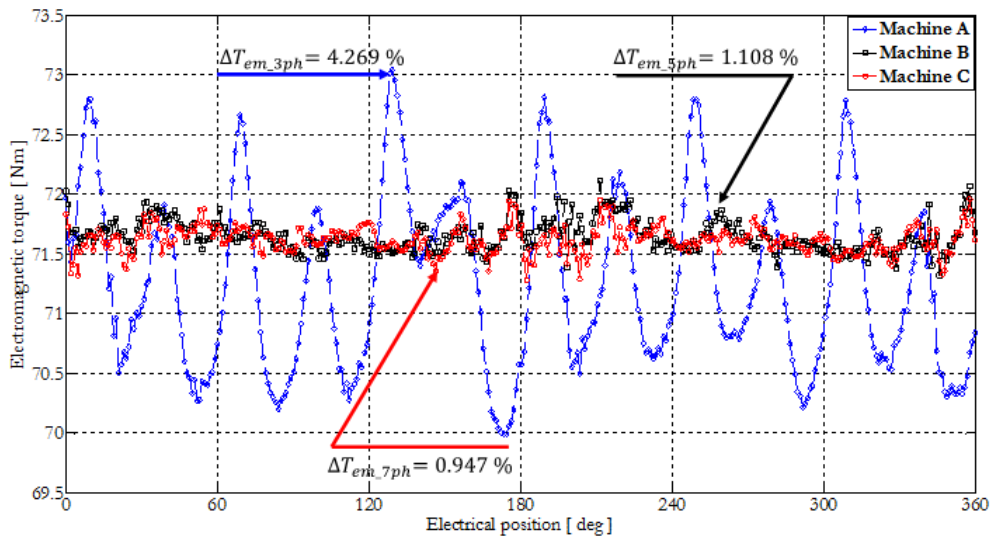
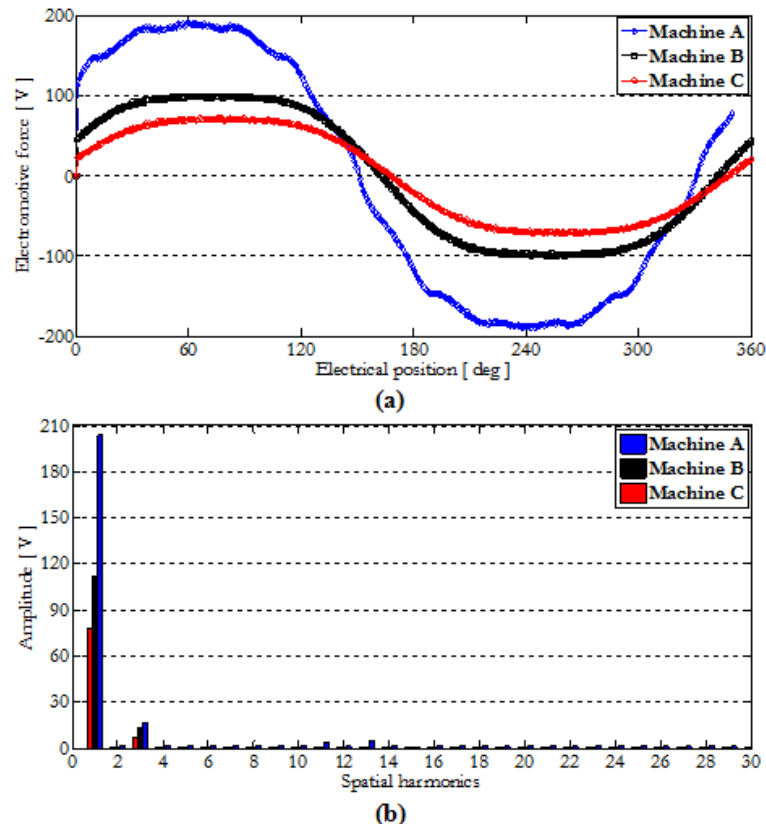


Fig. 6 – Electromagnetic torque.



**Fig. 7** – Back EMF : (a) Waveform and (b) Harmonic spectrum.

Fig. 7 shows the back EMF waveform of phase A at no-load [see Fig. 7(a)] as well as the harmonic spectrum [see Fig. 7(b)]. **Machine A** has a higher amplitude against **Machine B** and **Machine C** respectively.

To estimate the PM eddy-current losses, the electrical circuit used for simulation is represented in Fig. 8. Based on Kirchhoff's current law in the  $\sum I = 0$  form, no current flowing outside the PM should be provided. In order to take into account the eddy-current reaction field, each PM has been modeled as a solid conductor (i.e., SC1-SC2) with a high value resistance ( $\approx 10^9 \Omega$ ) at the ends of the PMs (i.e., R6-R7) in the electrical circuit. Without the eddy-current reaction field, the solid conductive regions in the electrical circuit are not necessary. It can be noted that the PMs are finely meshed (i.e., more than three elements in the skin depth of the PMs) to take into account the skin effect [14]. The mesh has been optimized so that the PMs eddy-current losses can converge numerically. The PMs eddy-current losses for the three machines are illustrated in Fig. 9. **Machine B** is better than its counterparts in terms of PMs eddy-current losses.

The DC copper losses (i.e., without the skin effect) in the windings at  $I = 30$  are 108 W for **Machine A**, 180 W for **Machine B**, and 252 W for **Machine C**. The increase of the phase's number causes additional losses.

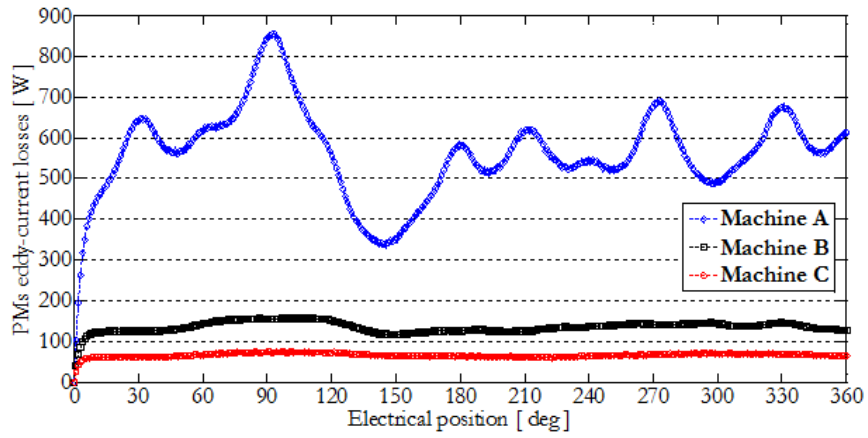


Fig. 8 – PMs eddy-current losses.

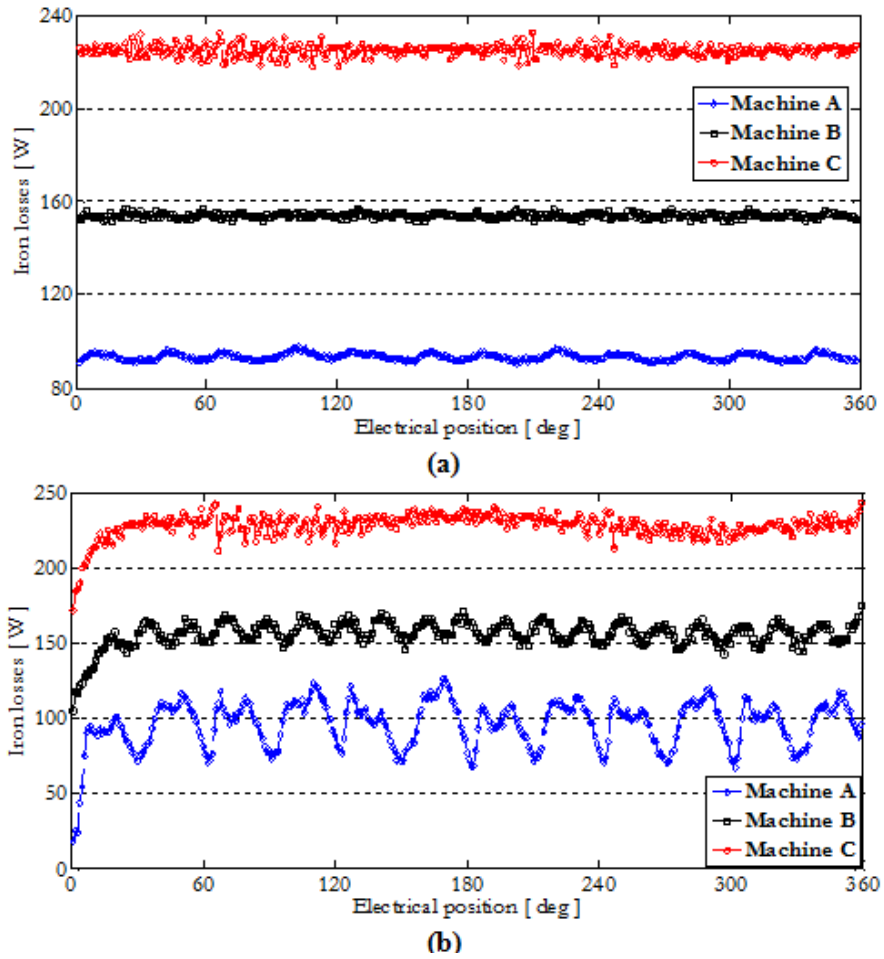


Fig. 9 – Iron losses : (a) Bertotti method, and (b)LS module.

Iron losses are separated on three types of losses : i) hysteresis, ii) eddy-current, and iii) excess. Those magnetic losses are determined numerically from Bertotti method [15] and with using “Loss Surface” (LS) module [16]. Various losses per volume, defined by Bertotti method, are given by :

$$dP_H = K_h B_m^2 f \quad (\text{Hysteresis}) \quad (5)$$

$$dP_J = \frac{\pi^2 \sigma d^2}{6} (B_m f)^2 \quad (\text{Eddy - current}) \quad (6)$$

$$dP_E = 8,67.K_e (B_m f)^2 \quad (\text{Excess}) \quad (7)$$

**Table 1** – Data of the sheet M270-35A (Bertotti Method).

Designation	Symbols	Machine A	Machine B	Machine C
Volumetric mass density	$\rho$		7650 $Kg.m^{-3}$	
Electrical conductivity	$\sigma$		$1.92 \times 10^6 S.m^{-1}$	
Thickness	$d$		0.35 mm	
Hysteresis coef.	$K_h$	123.313	126.12	128.686
Excessive coef.	$K_e$	0.739	0.738	0.739

**Table 2** – Summary of the comparison.

	Machine A	Machine B	Machine C
Slots number	12	20	28
Phases number	3	5	7
Poles number	10	18	26
Winding	Concentrated all teeth wound (two layers)		
Outside diameter		138.4 mm	
Iron length		136 mm	
Total volume		1.615 L	
Rotation speed		3,000 rpm	
Torque		71.5 Nm	
DC copper losses	108 W	180 W	252 W
PMs eddy-current losses	561.4 W	134.42 W	74.44 W
Iron losses (LS)	96.7 W	156.45 W	228.55 W
Iron losses (Bertotti)	93.36 W	153.86 W	224.8 W
Output power		22.45 kW	
Efficiency	96.3 %	97.29 %	96.6 %

The physical parameters and the coefficients are given in Table 1 for M270-35A sheet. Fig. 10 represents the iron losses with Bertotti method [see Fig. 10(a)] and LS module. [see Fig. 10(b)]. As that magnetic losses are linked to magnetic flux density and to frequency, it is clear that **Machine C** will have more losses than **Machine B** and **Machine A** respectively. The flux density value of the three machines are close, so the frequency is the element causing the difference in magnetic losses. Results of this study are summarized in Table 2 with the calculation of efficiency of suited machines.

#### 4. Conclusion

This comparative study is a part of modeling and design of multi-phases PMSMs. It is shown that for same quantities of iron/copper/PMs losses, torque ripple is less important for **Machine B** (5-phases) and **Machine C** (7-phases) in comparison with **Machine A** (3-phases), and it is obtained for the same average electromagnetic torque.

At end of this study, **Machine C** is more suitable by having less PMs eddy-current losses against **Machine B** and **Machine C**. Iron losses are more important in **Machine C** due to poles number, which is, greater than the two others studied machines. However, the machine having 5-phases, may be interesting in terms of control (less complicated against the one having 7-phases). **Machine A** is not selected because of important PMs eddy-current losses and torque ripple in comparison with **Machine B** and **C**.

Different outlooks may be considered, viz., a comparative study for different PMs disposals, magnetization direction or other windings patterns.

#### Acknowledgements

This work is supported by RENAULT-SAS, Guyancourt, France.

#### REFERENCES

- [1] C.C. Chan, A Bouscayrol, K. Chen, « Electric, Hybrid and fuel Cell Vehicles : Architectures and Modelling », IEEE Transactions on Vehicular Technology, vol. 59, no. 2, pp. 589-598, 2010.
- [2] J. Wang, X. Yuan, K. Atallah, « Design Optimization of a Surface-Mounted Permanent-Magnet Motor With Concentrated Windings for Electric Vehicle Applications », IEEE Transactions on Vehicular Technology, vol. 62, no. 3, pp. 1053-1064, 2013.
- [3] A. Cassat, C. Espanet, R. Coleman, L. Burdet, E. Leleu, D. Torregrossa, J. M'Boua, A. Miraoui, « A Practical Solution to Mitigate Vibrations in Industrial PM Motors Having Concentric Windings », IEEE Transactions on Industry Applications, vol. 48, no. 5, pp. 1526-1538, 2012.
- [4] E. Levi, « Multiphase Electric Machines for Variable-Speed Applications », IEEE Transactions on Industrial Electronics, vol. 55, no. 5, pp. 1893-1909, 2008.
- [5] K.T.J.E. Miller, M.I. McGilp, « Analysis of Multi-Phase Permanent-Magnet Synchronous Machines », International Conference on Electrical Machines and Systems, ICEMS 2009, Tokyo (Japan).
- [6] L. Parsa, H.A. Toliyat, « Five-Phase Permanent-Magnet Motor Drives », IEEE Transactions on Industry Applications, vol. 41, no. 1, pp. 30-37, 2005.

- [7] F. Scuiller, J-F. Charpentier, E. Semail, S. Clénet « Comparison of two 5-phase Permanent Magnet machine winding configurations. Application on naval propulsion specifications », IEEE International Electric Machines & Drives Conference, IEMDC 2007, Antalya (Turkey).
- [8] I. Petrov, P. Ponomarev and J. Pyrhönen, « Torque ripple reduction in 12-slot 10-pole fractional slot permanent magnet synchronous motors with non-overlapping windings by implementation of unequal stator teeth widths », International Conference on Electrical Machines, ICEM 2014, Berlin (Germany).
- [9] B. Aslan, E. Semail, J. Korecki and J. Legranger, « Slot/pole combinations choice for concentrated multiphase machines dedicated to mild-hybrid applications », 37th Annual Conference on IEEE Industrial Electronics Society, IECON 2011, Melbourne (VIC).
- [10] A. Soualmi, F. Dubas, A. Randria, C. Espanet, « Comparative Study of Permanent-Magnet Synchronous Machines with Concentrated Windings for Railway Application », International Conference on Electrical Machines and Systems, ICEMS 2011, Beijing (China).
- [11] N. Bianchi, M. Dai Pré, « Use of the Star of Slots in Designing Fractional-Slot Single-Layer Synchronous Motors », IEE Proceedings-Electric Power Applications, vol. 153, no. 3, pp. 459-466, 2006.
- [12] M. Hörz, H-G. Herzog, A. Haas, « Axial Flux Machine with Single Tooth Fractional Slot Winding – Comparaison of Different Winding Design Approaches », International Symposium on Power Electronics, Electrical Drives, Automation and Motion, SPEEDAM 2006, Taormina (Italy).
- [13] Flux2D, « General operating instructions – Version 12.1. », Cedrat S.A. Electrical Engineering, 2015, Grenoble, France.
- [14] F. Dubas, A. Rahideh, « Two-Dimensional Analytical Permanent-Magnet Eddy-Current Loss Calculations in Slotless PMSM Equipped With Surface-Inset Magnets », IEEE Transactions on Magnetics, vol. 50, no. 3, 6300320, 2014.
- [15] G. Bertotti, « General properties of power losses in soft ferromagnetic materials », IEEE Transactions on Magnetics, vol. 24, no. 1, pp. 621-630, 1988.
- [16] T. Chevalier, A. Kedous-Lebouc, B. Comut, « A new dynamic hysteresis model for electrical steel sheet », Physica B : Physic of Condensed Matter, vol. 275, no. 1-3, pp. 197-201, 2000.

# Elimination of Harmonics in Modified 5-Level CHB Inverter Using DE Algorithm

Fayçal Chabni <sup>a \*</sup>, Rachid Taleb <sup>a</sup>, Abdelkader Mellakhi <sup>a</sup>

<sup>a</sup> Electrical Engineering Department, Hassiba Benbouali University. Laboratoire Génie Electrique et Energies Renouvelables (LGEER), Chlef, Algeria

## ARTICLE INFO

### Article history :

Received September 2016

Accepted September 2016

### Keywords :

Selective harmonic elimination ;

Modified 5-level CHB inverter ;

Differential evolution ;

Optimization.

## ABSTRACT

The main objective of this paper is to demonstrate the application of Selective Harmonic Elimination PWM (SHEPWM) based on Differential Evolution (DE) optimization algorithm to improve the AC output voltage quality of modified 5-level Cascaded H-Bridge (CHB) inverter. The DE optimization algorithm is used to solve non-linear transcendental equations necessary for the SHEPWM. Computational results obtained from computer simulations presented a good agreement with the theoretical predictions. A laboratory prototype based on STM32F407 microcontroller was built in order to validate the simulation results. The experimental results show the effectiveness of the proposed modulation method.

©2016 LESI. All rights reserved.

## 1. Introduction

Several modulation strategies have been proposed and studied for the control of multi-level inverters such as Sinusoidal Pulse width modulation (SPWM) [1] and space vector pulse width modulation (SVPWM) [2]. A more efficient method called selective harmonic elimination pulse width modulation (SHE-PWM) is also used; the method offers a lot of advantages such as operating the inverters switching devices at a low frequency which extends the lifetime of the switching devices. The main disadvantage of this method is that a set of non-linear equations must be solved to obtain the optimal switching angles to apply this strategy.

Multiple computational methods have been used to calculate the optimal switching angles such as Newton-Raphson (N-R) [3], this method depends on initial guess of the angle values in such a way that they are sufficiently close to the global minimum (desired solution). And if the chosen initial values are far from the global minimum, non-convergence can occur.

Selecting a good initial angle, especially for a large number of switching angles can

\*Email : chabni.fay@gmail.com

be very difficult. Another approach is to use optimization algorithms such as Genetic Algorithm (GA) [4], FireFly algorithm (FFA) [5] and Particle Swarm Optimization (PSO) [6]. The main advantage of these methods is that they are free from the requirement of good initial guess.

The differential evolution (DE) is one of the most powerful optimization algorithms. Since its introduction in 1997 [7], the algorithm has drawn the attention of many scientists over the world, resulting in multiple variants derived from the original basic algorithm, with improved performance. The DE is a simple yet powerful algorithm; it is composed of three main operations mutation, crossover and selection [8]. The algorithm uses the difference of solution vectors to create new candidate solutions using the above-mentioned operators. This work investigates the use of (DE) as an optimization tool to implement the (SHEPWM) for a five level inverter.

This paper presents a simple and fast optimal solution of harmonic elimination of a modified five level inverter with equal DC sources using the differential evolution algorithm. The algorithm is used to solve a system of non-linear equations that describes the waveform of the output voltage in order to obtain the optimal switching angles, to improve the output voltage quality.

This paper is organized as follows : the next section explains briefly the structure of the proposed multilevel inverter and its control, the third section covers the application of the differential evolution algorithm for the selective harmonic elimination, this section details the procedures to obtain the optimal switching angles and the formulation of the objective function, the fourth section presents the simulation results obtained from the mathematical model of the system and the optimization method. The effectiveness of the selective harmonic elimination using DE is verified using a small scale laboratory five level inverter based on STM32F407 Microcontroller unit, the section also presents and discusses the hardware implementation and the experimental results in details. The conclusion is presented in the last section.

## 2. Modified 5-level cascaded H-bridge inverter

The main objective of the proposed multilevel inverter is to reduce the number of semiconductor switches, without changing the staircase nature of the output voltage. The topology was originally proposed by Kh. El-Naggar in [9]. The proposed inverter should have the same number of input DC voltage sources as a traditional five level cascade H-bridge inverter. When compared to a conventional cascade topology, the proposed inverter provides a lot of advantages; this configuration does not require a large number of components and does not need clamping diodes or balancing capacitors, the simplicity of its topology allows easier maintenance.

The proposed inverter presented in Fig.1 has a main H-Bbridge inverter formed by  $S_1$ ,  $S_2$ ,  $S_3$  and  $S_4$ , two auxiliary switching devices  $S_5$  and  $S_6$  and two input DC voltage sources  $V_{dc1}$  and  $V_{dc2}$ . The function of the auxiliary switching devices is to control the connection of the dc sources so as to construct the staircase output voltage. The valid switching states for all possible combination are given in Table.1.

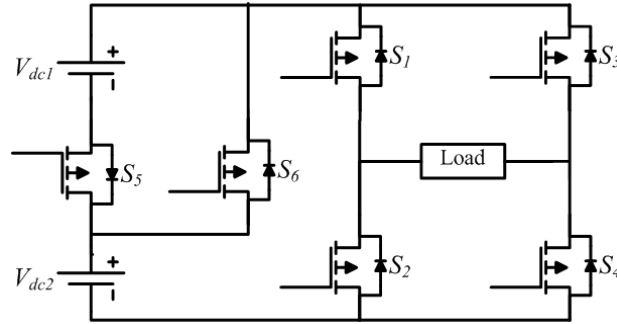


**Fig. 1** – Structure of the proposed multilevel inverter.

**Table 1** – Switching states of semiconductor devices for 5-level inverter.

Voltage levels (p.u.)	Switches state					
	S1	S2	S3	S4	S5	S6
2	on	off	off	on	on	off
1	on	off	off	on	off	off
0	on	off	off	on	on	on
-1	off	on	on	off	off	off
-2	off	on	on	off	on	off

### 3. Selective harmonic elimination using DE algorithm

The number of voltage levels that can be generated by CMLIs is generally presented by  $2P + 1$  where  $P$  represents the number of voltage levels or switching angles in a quarter waveform of the signal, and  $P - 1$  is the number of undesired harmonics that can be eliminated from the generated waveform. In a five level inverter, the number of voltage levels in quarter waveform is two which means the number of harmonics that can be eliminated is one ( $3^{rd}$  harmonic).

In order to eliminate the undesired harmonics, the switching angles  $\theta_1$  and  $\theta_2$  represented in Fig. 2 must be computed.

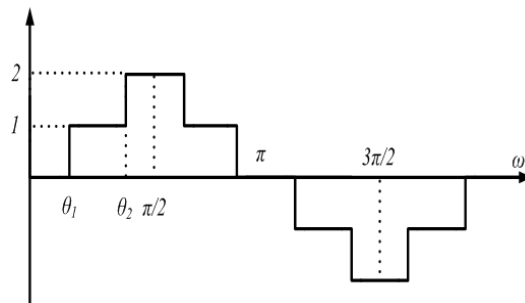


**Fig. 2** – Quarter waveform of a five-level inverter.

For the staircase output voltage waveform of multilevel inverter as shown in Fig. 2 there are 2 voltage levels (in quarter waveform) and 1 undesired harmonic.

To control the peak value of the output voltage to be  $V_1$  and eliminate the  $3^{rd}$  harmonic the resulting equations and since the voltage waveform has quarter and half wave symmetry characteristics, the Fourier series expansion is given as :

$$V(\omega t) = \sum_{n=1,3,5,\dots}^{\infty} \left[ \frac{4V_{dc}}{n\pi} \sum_{i=1}^p \cos(n\theta_i) \right] \sin(n\omega t) \quad (1)$$

where  $n$  is rank of harmonics,  $n = 1, 3, 5, \dots$ , and  $p = (N - 1)/2$  is the number of switching angles per quarter waveform, and  $\theta_i$  is the  $i$ th switching angle, and  $N$  is the number of voltage levels per half waveform. The optimal switching angles  $\theta_1$  and  $\theta_2$  can be determined by solving the following system of non-linear equations :

$$\begin{cases} H_1 = \cos(\theta_1) + \cos(\theta_2) + \cos(\theta_3) = M \\ H_3 = \cos(3\theta_1) + \cos(3\theta_2) + \cos(3\theta_3) = 0 \end{cases} \quad (2)$$

where  $M = (((N - 1)/2)r/4)$ ,  $r$  is the modulation index.

The obtained solutions must satisfy the following constraint :

$$0 < \theta_1 < \dots < \theta_p < \pi/2 \quad (3)$$

An objective function is necessary to perform the optimization operation, the function must be chosen in such way that allows the elimination of low order harmonics while maintaining the amplitude of the fundamental component at a desired value Therefore the objective function is defined as :

$$F(\theta_1, \theta_2 \dots \theta_p) = \left( \sum_{n=1}^p \cos(\theta_n) - M \right)^2 + \left( \sum_{n=1}^p \cos(3\theta_n) \right)^2 \quad (4)$$

The optimal switching angles are obtained by minimizing Eq. (4) subject to the constraint Eq. (3). The main problem is the non-linearity of the transcendental set of Eq. (2), the differential algorithm is used to overcome this problem.

The differential evolution algorithm (DE) is an optimization method is composed of three main steps initialization, mutation and crossover. The general structure of a DE program is shown in Fig. 3. The algorithm perturbs the population of vectors by employing the mutation, whereas its diversity is controlled by the cross-over process [10].

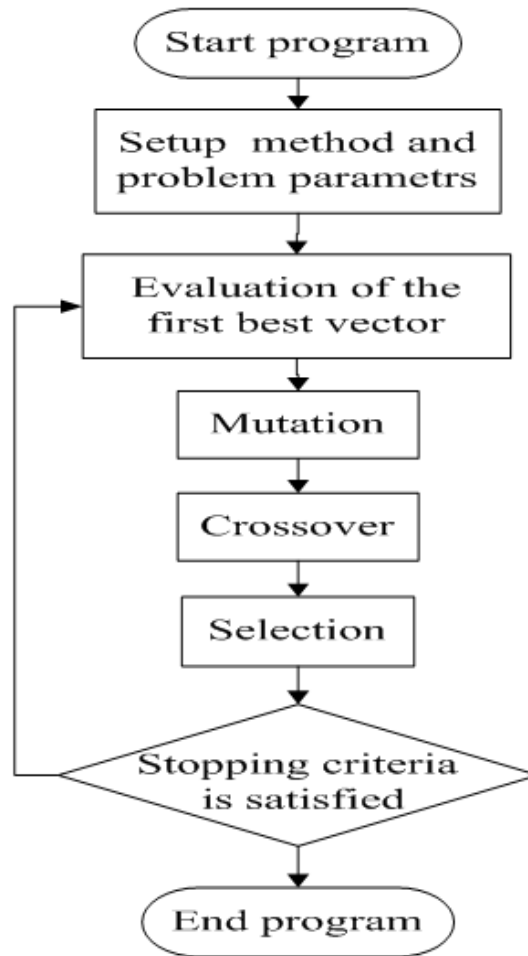


**Fig. 3** – Flowchart of DE algorithm.

In the case of SHEPWM, differential evolution algorithm is used as an optimization tool to perform a random search for the global minima, which is forcing the objective function (4) towards an allowable error value.

The optimization process starts by initializing the necessary parameters of the algorithm, such as the population size (NP), crossover probability (CP), upper and lower bounds ( $\theta_{min}$  and  $\theta_{max}$ ) and the maximum number of iterations. It should be noted that the boundaries must satisfy Eq. (3). The next step is to randomly generate an initial population of switching angles in this process the algorithm creates

$$\theta_{ij}^{(0)} = \theta_{min\ ij} + rand_i (\theta_{max\ j} - \theta_{min\ j}) \quad (5)$$

with  $i = 1, 2, \dots NP$  and  $j = 1, 2, \dots N$

where  $\theta_{ij}^{(0)}$  is the initial population,  $i$  presents the population size in this study  $NP = 50$ ,  $j$  is the number of decision variables which represents the number of switching angles, in case of a five level inverter  $N = 2$ . After the initialization process, the generated

population is evaluated, the evaluation of the fitness of each individual is carried out by using (4).

The mutation process creates a mutant  $v_{ij}$  vector based on the initial population ; this process is described by the following expression

$$v_{ij} = X_{r1} + F (X_{r2} - X_{r3}) \tag{6}$$

$X_{r1}$ ,  $X_{r2}$  and  $X_{r3}$  are vectors randomly sampled from the generated population,  $X_r = [\theta_{i1}, \theta_{i2}, \dots, \theta_{iN}]$ , the indices  $r1$ ,  $r2$  and  $r3$  are integers randomly chosen from the range [1 NP], they are also chosen to be different from the index  $i$ , the parameter  $F$  is the mutation constant which controls the amplification of the differential variation ( $X_{r2} - X_{r3}$ ), the value of this parameter is randomly generated from the range [0 1], it should be noted that multiple mutation methods were reported in [11].

To improve the diversity of the population, the crossover operation comes into play, after generating the mutant vector  $v_{ij}$  through mutation, this operation assures the production of fitter individuals, the result of this process is a vector  $u$  obtained by mixing the components of  $v_{ij}$  and  $X_i$  the process can be expressed as :

$$u = \begin{cases} v_{ij} & \text{if } rand \leq CP \text{ or } j = j_{rand} \\ X_i & \text{otherwise} \end{cases} \tag{7}$$

where  $rand$  is a random number in the range of [0 1],  $CP$  is the crossover probability constant, it controls the diversity of the population and it has a value between 0 and 1 [12],  $j_{rand}$  is randomly chosen index. Once the crossover process is completed, the selection process comes into play to decide whether the  $u_i$  or  $X_i$  vector survives for the next generation, this process is carried out to choose the fittest individual. The selection process can be expressed mathematically as :

$$X_i^{G+1} = \begin{cases} u_i^{G+1} & \text{if } f(u_i^{G+1}) < f(X_i^G) \\ X_i^G & \text{otherwise} \end{cases} \tag{8}$$

where  $f(X)$  is the objective function to be minimized and  $G$  is the generation count. Once the selection operation is completed, the algorithm loop is repeated until the stopping criteria is satisfied, in this study the DE algorithm is limited by maximum number of iterations  $Nitr = 1000$ .

#### 4. Simulation results

In order to prove the theoretical predictions and to test the effectiveness of the proposed algorithm, the control method and the proposed inverter were developed and simulated using MATLAB/SIMULINK scientific programming environment ; the optimization program was executed on a computer with Intel(R) Core(TM) i3 CPU@ 2.13GHz Processor and 4GB of RAM, the optimization algorithm takes 974.463 seconds to complete the computation process.

To verify the effectiveness of the proposed method, total harmonic distortion (THD) is used as a performance indicator to evaluate the quality of output AC voltage waveform generated from the multilevel inverter, the THD is defined as the total amount of harmonics related to the fundamental, it can be calculated using the following formula :

$$THD\% = \frac{\sqrt{\sum_{n=3}^{19} H_n^2}}{H_1} \times 100 \quad (9)$$

The differential evolution algorithm is used to find the switching angles for each value of modulation index  $r$ ; the total harmonic distortion is computed also for each  $r$ , Fig. 4 illustrates optimal switching angles (in degrees) versus modulation index  $r$  with  $r \in [0.2, 1.2]$ , the angles are computed with a fine step-size of 0.01, and it can be seen that in some ranges of the modulation index, the obtained solutions exceeded the 90 degrees limit, those solutions are not going to be taken in consideration. Fig. 5 shows the variation of the total harmonic distortion (THD) versus the modulation index, these results are obtained by using equations (9) and (2).

To confirm the validity of the proposed algorithm, angles extracted from the obtained switching angles were applied to a mathematical model of a five-level inverter. The fundamental frequency used in this simulation is 50Hz, the input DC voltages are set to be;  $V_{dc1} = 15V$  and  $V_{dc2} = 15V$  the switching angles to be applied (in degrees) are :  $\theta_1 = 5.08^\circ$  and  $\theta_2 = 54.9^\circ$  and which correspond to the modulation index  $r = 1$ .

Fig. 6 shows the output voltage obtained from the multilevel inverter for  $r = 1$ . Fig. 7 shows its spectra of the output voltage. As expected, the  $3^{rd}$  harmonic is successfully eliminated, the total harmonic distortion  $THD = 23.73\%$ .

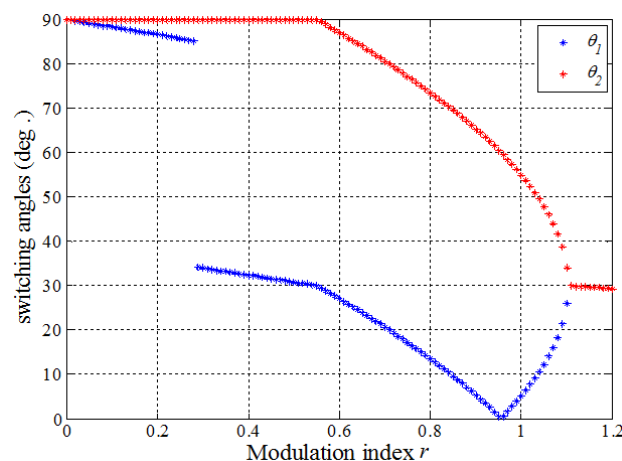


**Fig. 4** – Switching angles versus modulation index.

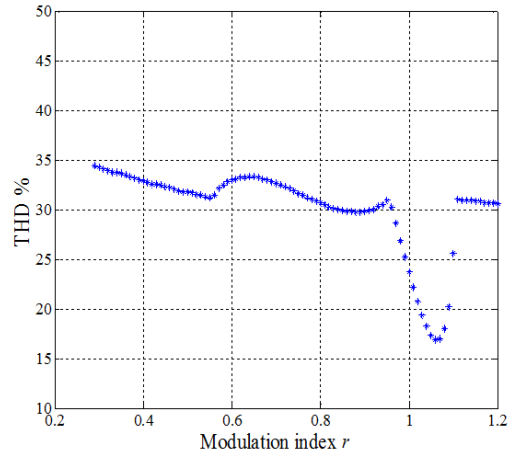


Fig. 5 – THD versus modulation index.

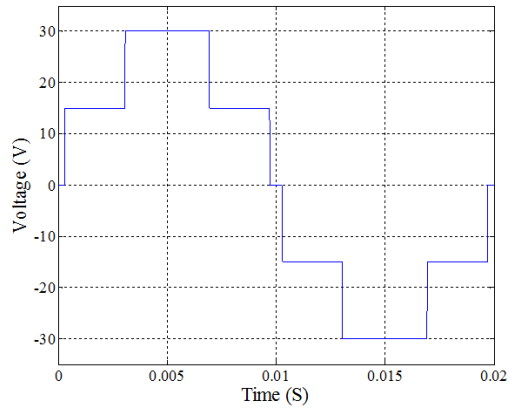


Fig. 6 – Output voltage generated by the inverter.

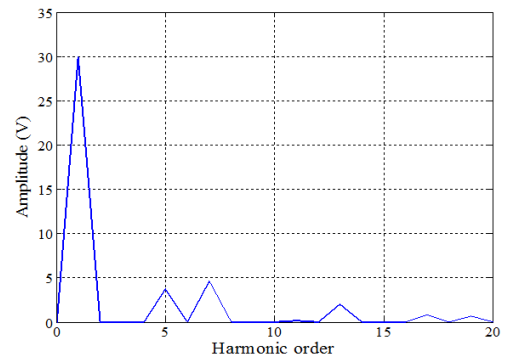
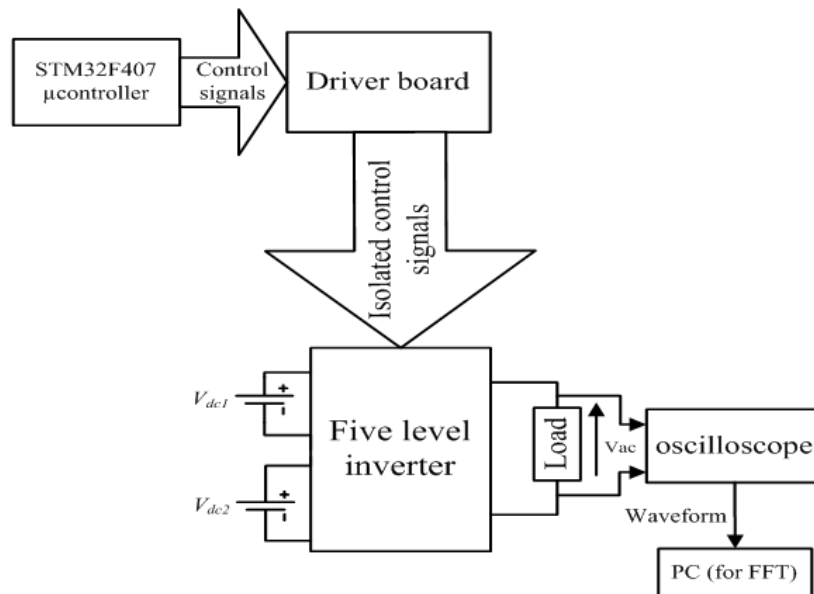


Fig. 7 – FFT of 5-level inverter voltage output.

## 5. Experimental results

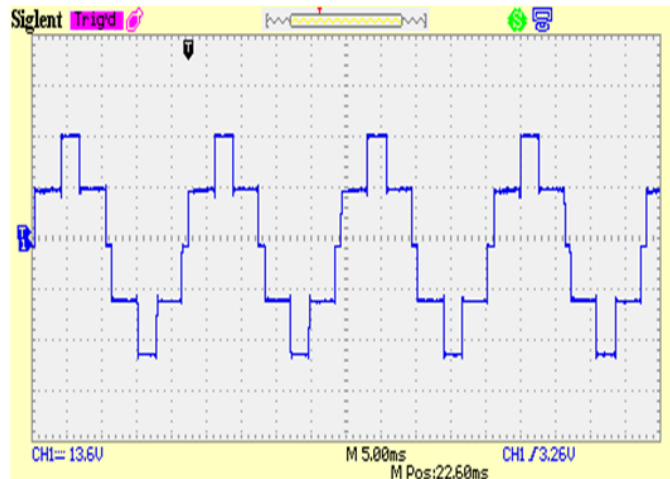
The proposed method was validated by building a small scale laboratory prototype, IRF640(200V,18A) MOSFETs were used as switching devices SDS1000 oscilloscope100MHz 500Ms/s was used to capture the voltage waveforms, an STM32F407 microcontroller was used to generate control signals for the switching devices, the FFT analysis was performed by computer connected to the oscilloscope trough USB.

Fig. 8 presents the block diagram of the laboratory prototype of the five level inverter that is implemented as mentioned before with eight IRF 640 Metal Oxide Semiconductor Field Effect Transistors (MOSFET), it should be noted that those switching devices are also equipped with freewheeling diodes. TLP250 photocouplers are used to provide electrical isolation between the MCU and the power circuits, and also to provide proper and conditioned gate signals to the MOSFETs. The switching angles are calculated using differential evolution algorithm by a computer, once the switching angles are obtained, the switching patterns for each switching device will be stored inside the memory of the MCU as a look-up table.



**Fig. 8** – Block diagram of the hardware setup.

The single phase five level voltage pattern obtained in simulation shown in Fig. 6 is experimentally validated and the result is shown in Fig. 9. Fig. 10 illustrates the FFT analysis of the experimentally obtained voltage waveform; it can be clearly seen that the 3rd harmonic was successfully eliminated. This result matches perfectly the simulation result presented in Fig. 7. The total harmonic distortion of the experimental voltage waveform is 22.85% which is very close to the simulation result.



**Fig. 9** – Output voltage waveform generated the proposed multilevel inverter.

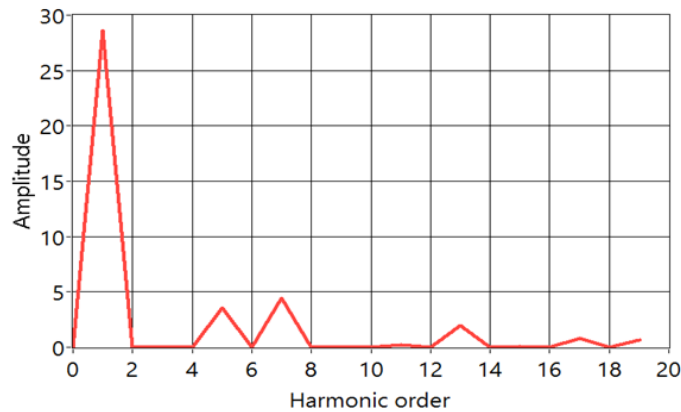


**Fig. 10** – FFT of 5-level inverter experimental voltage output.

## 6. Conclusion

This paper illustrates the use of differential evolution algorithm in selective harmonic elimination for a modified single phase five level CHB inverter to improve the harmonic quality of the generated output voltage. The proposed multi-level inverter with equal DC sources has the advantage of generating multiple voltage levels with less switching components. The differential evolution algorithm is used to solve a set of non-linear equations in order to obtain the optimal switching angles to perform the (SHE) modulation strategy. The total harmonic distortion (THD) was chosen as a performance indicator in order to examine the effectiveness of the proposed algorithm. The validity of the method has been proven by computer simulation using Matlab/Simulink scientific programming environment and verified by experimental hardware set-up based on STM32F407 microcontroller. The obtained results from the simulation and hardware show a good agreement with the theoretical prediction.

## REFERENCES

- [1] B. Karami, R. Barzegarkhoo, A. Abrishamifar and M. Samizadeh, "A switched-capacitor multilevel inverter for high AC power systems with reduced ripple loss using SPWM technique," *Power Electronics, Drives Systems & Technologies Conference (PEDSTC)*, Tehran, 2015, pp. 627-632.
- [2] K. C. Jana and S. K. Biswas, "Generalised switching scheme for a space vector pulse-width modulation-based N-level inverter with reduced switching frequency and harmonics," in *IET Power Electronics*, vol. 8, no. 12, pp. 2377-2385, 2015.
- [3] T. Mistry, S. K. Bhatta, A. K. Senapati and A. Agarwal, "Performance improvement of induction motor by Selective Harmonic Elimination (SHE) using Newton Raphson (N-R) method," *International Conference on Energy Systems and Applications*, Pune, India, 2015, pp. 364-369.
- [4] Erkan Deniz, Omur Aydogmus, Zafer Aydogmus, Implementation of ANN-based Selective Harmonic Elimination PWM using Hybrid Genetic Algorithm-based optimization, *Measurement*, Volume 85, May 2016, Pages 32-42.
- [5] M. Gnana Sundari, M. Rajaram, Sujatha Balaraman, Application of improved firefly algorithm for programmed PWM in multilevel inverter with adjustable DC sources, *Applied Soft Computing*, Volume 41, April 2016, Pages 169-179.
- [6] Shimi Sudha Letha, Tilak Thakur, Jagdish Kumar, Harmonic elimination of a photovoltaic based cascaded H-bridge multilevel inverter using PSO (particle swarm optimization) for induction motor drive, *Energy*, Volume 107, 15 July 2016, Pages 335-346.
- [7] S. Das and P. N. Suganthan, "Differential Evolution : A Survey of the State-of-the-Art," in *IEEE Transactions on Evolutionary Computation*, vol. 15, no. 1, pp. 4-31, Feb. 2011.
- [8] H. Suryoatmojo, A. M. B. Zakariya, S. Anam, A. Musthofa and I. Robandi, "Optimal controller for doubly fed induction generator (DFIG) using Differential Evolutionary Algorithm (DE)," *International Seminar on Intelligent Technology and Its Applications (ISITIA)*, Surabaya, 2015, pp. 159-164.
- [9] Kh. El-Naggar, T. H. Abdelhamid, " Selective harmonic elimination of new family of multilevel inverters using genetic algorithms", *Energy Conversion and Management*, Volume 49, Issue 1, pp 89–95, January 2008.
- [10] A. Hiendro, "Multiple switching patterns for SHEPWM inverters using Differential evolution algorithms" in *International Journal of Power Electronics and Drive Systems*, vol.1, no2, pp94-103, Dec 2011.
- [11] R. Vijayakumar, C. Devalalitha, A. Nachiappan and R. Mazhuvendhi, "Selective harmonic elimination PWM method using two level inverter by differential evolution optimization technique," *International Conference on Science Engineering and Management Research (ICSEMR)*, Chennai, 2014, pp. 1-6.
- [12] M. I. Mohd Rashid, A. Hiendro and M. Anwari, "Optimal HE-PWM inverter switching patterns using differential evolution algorithm," *IEEE International Conference on Power and Energy (PECon)*, Kota Kinabalu, 2012, pp. 32-37.

# On-line trajectory planning of time-jerk optimal for robotic arms

Nadir Bendali <sup>a \*</sup>, Mohammed Ouali <sup>a</sup>

<sup>a</sup> Structural Mechanics Research Laboratory, Department of Mechanical Engineering, University Blida, Algeria

## ARTICLE INFO

### Article history :

Received May 2016

Accepted July 2016

### Keywords :

Arm vibration ;  
Trajectory planning ;  
Time intervals ;  
Cubic splines ;  
Genetic algorithms.

## ABSTRACT

A method based on the computation of the time intervals of the knots for time-jerk optimal planning under kinematic constraints of robot manipulators in predefined operations is described in this paper. In order to ensure that the resulting trajectory is smooth enough, a cost function containing a term proportional to the integral of the squared jerk (defined as the derivative of the acceleration) along the trajectory is considered. Moreover, a second term, proportional to the total execution time, is added to the expression of the cost function. A Cubic Spline functions are then used to compose overall trajectory. This method can meet the requirements of a short execution time and low arm vibration of the manipulator and the simulation provides good results.

©2016 LESI. All rights reserved.

## 1. Introduction

The resolve of the problem of time-jerk optimal trajectory planning for robot manipulators along specified tasks is very important, these tasks can be the case of the handling of objects, the drilling/spot welding tasks or the installation of the electronic components. Decreased the execution time of the task is important to increase the productivity of the robot manipulators. Also, limiting the jerk is very important, because high jerk values can wear out the robot structure, and heavily excite its resonance frequencies ; vibrations induced by non-smooth trajectories can damage the robot actuators, and introduce large errors while the robot is performing tasks such as trajectory tracking moreover low-jerk trajectories can be executed more rapidly and accurately.

Many work in the field of robot manipulators has been devoted to study the problem of motion planning along specified tasks, we cite in this context the work of [1-2] the authors have treated the problem of trajectory planning of robot manipulator in imposed tasks by considering the kinematic constraints, they were used the sequential quadratic

\*Email :b1102@yahoo.com

programming (SQP) to minimize the cost function which represents a weighting between the execution time of the task and the interval squared jerk, the upper bounds on the absolute values of velocity, be specified, but the total execution time was not set a priori. In [3] a new approach called interval analysis is used to develop an algorithm that minimizes the maximum absolute value of jerk along the trajectory, the cubic splines were used to represent the trajectory in imposed tasks. In [4-5] the authors proposed a fast and unified approach based on particle swarm optimization (PSO) with K-means clustering to solve the near optimal solution of a minimum-jerk joint trajectory constrained by a fixed traverse time of a robot manipulator, the cubic splines were used to interpolate between the nodes of the trajectory in an imposed tasks. In [6-7] the authors has been described an experimental validation of the minimum time-jerk trajectory planning algorithm, the trajectories have been implemented on Cartesian 3-axes manipulator equipped with a piezoelectric accelerometer, the obtained experimental results have been discussed by considering the measure of the acceleration (directly related to the vibration induced on the mechanism) as the comparison parameter. In [8] the authors developed an approach based on fuzzy genetic algorithm using real coding and elitism approach for treat the problem of trajectory planning of robotics arm along specified tasks to minimize time-jerk by considering the kinematic constraints. The authors [9] studied the relationship between the maximum vibratory amplitude and the jerk limit ; they formulated the influence of a jerk-controlled movement. In [10] the authors used trigonometric splines to interpolate the trajectories of 3-axes manipulator, where the spline parameters were considered to minimize the jerk by a close form solution.

In this study thus, we propose a unified and fast method for find the minimum time-jerk trajectory planning of robotics arm based on the computation of the time intervals of the knots. To validate the proposed method, an objective function [8] is used and the results demonstrate that our proposed method achieves the best results by less computation time than [8].

This paper is organized as follows. In Section 2, the minimum time-jerk joint trajectory optimization problem is formulated. In section 3, the kinematic constraints are presented. In section 4, the proposed method based on the time intervals and genetic algorithms is discussed. In section 5, numerical application on a three degree-of-freedom glass substrate handling robot is presented. Discussions and comparisons results are presented in Section 6. Conclusions are summarized in Section 7.

## 2. Problem formulation

In our joint trajectory planning, we assume the robot manipulator has N joints and the trajectory for each joint has M+1 knot points including the first and last. Thus, for each joint, there exist M time intervals and we choose the second and penultimate knot points as the extra points to represent the robot trajectory [11].

We apply cubic splines function to each joint to interpolate the joint trajectory between every two neighbor knot points. The velocities and accelerations of the initial and terminal conditions ( $v_1, v_m, a_1,$ and  $a_m$ ) are specified to be zero. These conditions cause two equations of the spline algorithm becoming zero and the path pattern cannot be solved. Therefore, two extra knots (position values at time  $t_2$  and  $t_{m-1}$ ) are added and their



Where,

$$K_1 = \left( h_{m-2} - \frac{h_{m-1}^2}{h_{m-2}} \right), K_2 = \left( 3h_{m-1} + 2h_{m-2} + \frac{h_{m-1}^2}{h_{m-2}} \right)$$

And the vector  $B$  is given by :

$$B = \begin{bmatrix} 6(q_3/h_2 + q_1/h_1) - 6(1/h_1 + 1/h_2) [q_1 + h_1\dot{q}_1 + (h_1^2/3)\ddot{q}_1] - h_1\ddot{q}_1 \\ (6/h_2) [q_1 + h_1\dot{q}_1 + (h_1^2/3)\ddot{q}_1] + 6q_4/h_3 - 6(1/h_2 + 1/h_3)q_3 \\ 6[(q_{i+1} - q_i)/h_i - (q_i - q_{i-1})/h_{i-1}] \\ \vdots \\ (6/h_{m-2}) [q_m - h_{m-1}\dot{q}_m + (h_{m-1}^2/3)\ddot{q}_m] \\ -6(1/h_{m-2} + 1/h_{m-3})q_{m-2} + 6q_{m-3}/h_{m-3} \\ -6(1/h_{m-1} + 1/h_{m-2}) [q_m - h_{m-1}\dot{q}_m + (h_{m-1}^2/3)\ddot{q}_m] \\ +6(q_m/h_{m-1} + q_{m-2}/h_{m-2}) - h_{m-1}\ddot{q}_m \end{bmatrix}$$

After these  $M + 1$  parameters are solved, we derive the jerk of the trajectory of the  $i - th$  joint by the equation :

$$J_i(t) = -\frac{1}{h_i}\ddot{Q}_i(t_i) + \frac{1}{h_i}\ddot{Q}_i(t_{i+1}); \quad i = 1, 2, \dots, m - 1 \quad (7)$$

From (7), we determine that the jerk depends on the length of the time interval  $h_i$ . Once we derive the jerk, the minimum jerk joint trajectory optimization problem can be formulated by an objective function described as : solve the maximum value of the jerk of each joint along the trajectory and minimize the summation of every maximum value of the jerk that is :

$$\min \left[ \sum_{i=1}^N \max_{h_i} |J_i(t)| \right] \quad (8)$$

The jerk is the key factor that causes robot arm vibration mainly when decreased the execution time of the task is important. In the paper, we adopt the objective function used in [8] which minimize two terms composed by the term proportional to the total execution time and the other one proportional to the total jerk. So the mathematic expression of the objective function model can be defined as :

$$F_{obj} = \min \left( k_T \sum_{i=1}^N T_i + k_J \sum_{i=1}^N \max_{h_i} |J_i(t)| \right) \quad (9)$$

The subjects are :

- Joint velocities :  $\left| \dot{Q}_{ij}(t) \right| \leq \dot{Q}_{ij}^{\max}$  for  $i = 1, \dots, n$  and  $j = 1, \dots, m - 1$

- Joint accelerations :  $\left| \ddot{Q}_{ij}(t) \right| \leq \ddot{Q}_{ij}^{\max}$  for  $i = 1, \dots, n$  and  $j = 1, \dots, m - 1$
- Joint jerks :  $|J_{ij}(t)| \leq J_{ij}^{\max}$  for  $i = 1, \dots, n$  and  $j = 1, \dots, m - 1$

Here,  $T_i$  is the total execution time of the tasks;  $k_T$  and  $k_J$  are the weight coefficient change according to the user needs can favor either the execution time of the task is the jerk. Also,  $\dot{Q}_{ij}^{\max}$ ,  $\ddot{Q}_{ij}^{\max}$  and  $J_{ij}^{\max}$  are limit kinematics performances of the  $i - th$  joint deduced from technological and design data.

### 3. Constraints formulation

The velocity constraints of the optimization problem are formulated into the maximum absolute value of velocities at the extreme points  $t_i$  and  $t_{i+1}$  or  $t_i^{\otimes}$  where  $\dot{Q}_{ji}^{\otimes} = \dot{Q}_{ji} \left( t_i^{\otimes} \right) = 0$  in each interval [2]. The velocity is calculated using equation (2). The velocity constraints become :

$$\max \left\{ \left| \dot{Q}_{ji}(t_i) \right|, \left| \dot{Q}_{ji}(t_{i+1}) \right|, \left| \dot{Q}_{ji}^{\otimes} \right| \right\} \leq \dot{Q}_{ji}^{\max}; \quad j = 1, \dots, N; \quad \text{and} \quad i = 1, \dots, m-1 \quad (10)$$

The acceleration is the solution of system (6). The acceleration constraints are formulated from the acceleration linear function and the maximum absolute value exists at  $t_i$  or  $t_{i+1}$ . The acceleration constraints become :

$$\max \left\{ \left| \ddot{Q}_{j,1} \right|, \dots, \left| \ddot{Q}_{j,n} \right| \right\} \leq \ddot{Q}_j^{\max}; \quad j = 1, \dots, N \quad (11)$$

## 4. Proposed approach based in Genetic Algorithm

### 4.1. Initialization and route of generation

Let  $h$  be defined as the vector of design variables  $h_i = [h_1, h_2, \dots, h_{m-1}]$ . To initialize the optimization process it is considered that :

$$h^{(0)} = \max_{j=1, \dots, m-1} \left[ \left( \frac{|q_{i2} - q_{i1}|}{\dot{Q}_i^{\max}} \right), \left( \frac{|\dot{Q}_{i2} - \dot{Q}_{i1}|}{\ddot{Q}_i^{\max}} \right), \dots, \left( \frac{|\ddot{Q}_{im} - \ddot{Q}_{i,m-1}|}{J_i^{\max}} \right) \right]$$

As two extra knots are needed they are initially taken as :

$$q_{i2} = (q_{i1} + q_{i3})/2 \quad \text{and} \quad q_{i,m-1} = (q_{j,m-2} + q_{im})/2$$

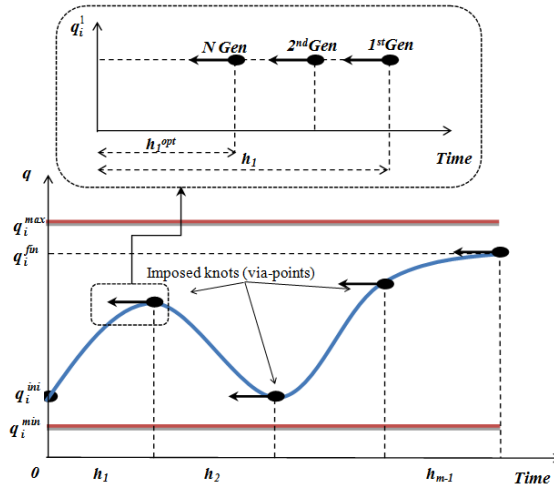


**Fig. 1** – Representation of the Cubic Spline Trajectory with the horizontal movement of the intermediate knots and the end point after generation.

During the optimization process the intermediate knots and the end point will generate only horizontally as seen in Fig.1, consequently the trajectory changes and moves also horizontally by minimizing the objective function and obtaining the best optimal vector as :

$$h^{opt} = [h_1^{opt}, h_2^{opt}, \dots, h_{m-1}^{opt}] \quad (12)$$

#### 4.2. Genetic algorithms

The use of a genetic algorithm starts with the creation of an initial population or chromosome in genetics, this chromosome is composed by genes or their number ( $G$ ) is defined according to the number of the knots ( $k$ ) used to generate the trajectories where  $k = G + 1$ ; it should be noted that this stage requires a coding of the genes, for that we have a real coding of these genes.

Thereafter this initial population will be generated by chance and we obtain for each chromosome a solutions corresponding with his performance index. For create the next generation, three genetic operators are applied :

- Reproduction : Usually the general strategy of reproduction is that the chromosomes (parents) with better performance index have the possibility of reproducing more.
- The crossover. It is the operator who will allow the mixing of the genetic characters of the population, this operator will create two children by carrying out a mixture of the chromosomes of two parents. In the simulation we will fix the rate or the probability of crossover equal to 65%.
- The mutation. It consists in deteriorating the coding of a chromosome. Its role is to make emerge new genes by exploring zones of the space of research which could not be visited by simple application of the operator of crossover ; in practice there exist many manners of transferring a chromosome by the modification of one or more gene, or by change of position of a gene, or the suppression by adding a gene. In the simulation we will fix the probability of mutation equal 4%.

## 5. Numerical application

The numerical application was implemented on a three degree-of-freedom glass substrate handling robot considered by authors in [8] to find the near optimal solution of a minimum-jerk joint trajectory using our proposed method.

The trajectory was given by four knot points and five time intervals ( $M = 5$ ) for all the three joints. Table 1 shows the interpolation point positions of each joint and Table 2 shows the maximum kinematic limits of velocity and acceleration of each joint.

**Table 1** – Interpolation point of each joint.

Joint	Interpolation point (deg)					
	1	2	3	4	5	6
1	120	Virtual	90	45	Virtual	0
2	-10	Virtual	60	40	Virtual	100
3	0	Virtual	-20	30	Virtual	70

**Table 2** – Kinematics constraints of each joint.

Joint	Velocity (deg/s)	Acceleration (deg/s <sup>2</sup> )
1	100	70
2	95	75
3	100	75

To represent the trajectory and solve the two unknown extra knot points in Table 1 we use both Eq. (4-5). We computed the jerk  $J_{ii}$  of the trajectory by Eq. (7) and formulated the minimum-jerk optimization problem by Eq. (9). In this optimization problem, the solution was transformed and denoted as Eq. (14). In the beginning, we created the initial population (chromosomes), and to seek the optimal trajectory, we must generate by chance according to the genetic algorithms technique a trajectories, the latter candidate of chromosome will be evaluated then compared with others, this operation is repeated for all the introduced chromosomes, and the best result is which satisfies the given objective function. It should be noted that any trajectory which would violate one of the velocities or accelerations constraints indicated in Table 2 will be automatically rejected by Eq. (10-11) respectively. These results were validated by the results obtained in [8].

## 6. Comparison of results and discuss

Each joint of cubic spline trajectories including their derivatives (velocities, accelerations and jerk) for  $K_J/K_T = 0.02$  and  $K_J/K_T = 0.3$  are illustrated in Fig. 2(a) and Fig. 2(b) respectively. For the first case we obtained a vector of time intervals  $h_i = [0.6017, 1.6992, 1.4349, 1.2623, 1.0895]$  equal to execution time  $\sum_{i=1}^5 h_i = 6.0876$  sec, for the second case we obtained a vector of time intervals  $h_i = [1.0301, 2.9256, 2.3687, 1.9771, 1.4761]$

equal to execution time  $\sum_{i=1}^5 h_i = 9.777\text{sec}$  this results show that the technique described in this paper obtains the better solution than [8] used Fuzzy genetic algorithm which obtained the execution time of task equal  $\sum_{i=1}^5 h_i = 6.72\text{sec}$  for the first case and  $\sum_{i=1}^5 h_i = 10.262\text{sec}$  for the second case.

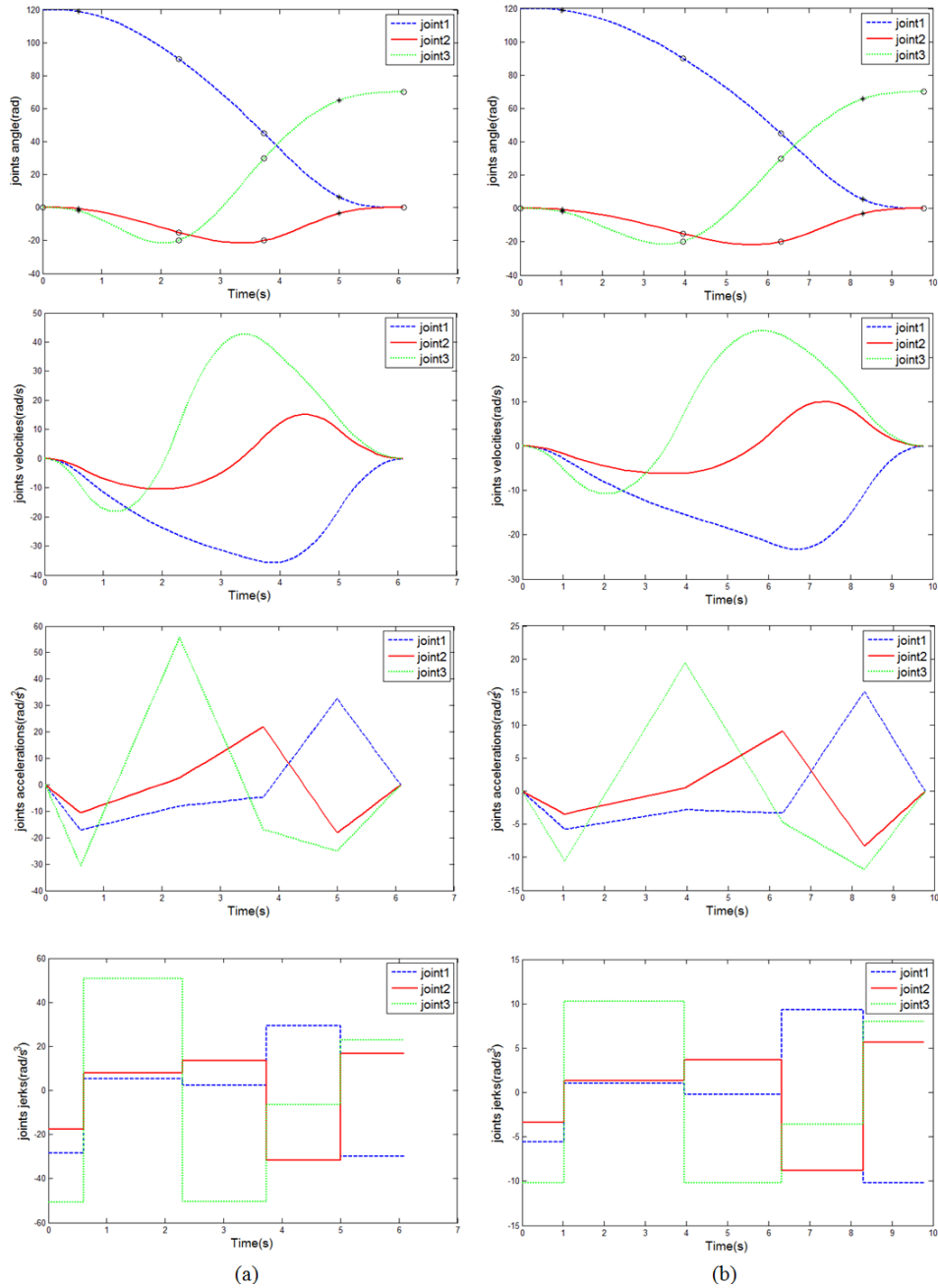


**Fig. 2** – The results of the simulation showing the trajectories of each joints angles (the circles indicate the knot positions and the crosses indicate the two dummy knots), velocities, accelerations and jerks of the glass substrate handling robot (a) :  $K_J / K_T = 0.02$  and (b) :  $K_J / K_T = 0.03$

Fig.3 shows the results histories of the optimization process of glass substrate handling robot for  $K_J/K_T = 0.02$  and  $K_J/K_T = 0.3$ , for the first case we obtained an objective function  $F_{obj} = 7.1025$  and for the second case the objective function  $F_{obj} = 12.846$ . These results were obtained with the fixed number of generation is 50 corresponding of 1/10 number of generation used in [8]; meanwhile our proposed method converges quickly and have faster calculation speed.

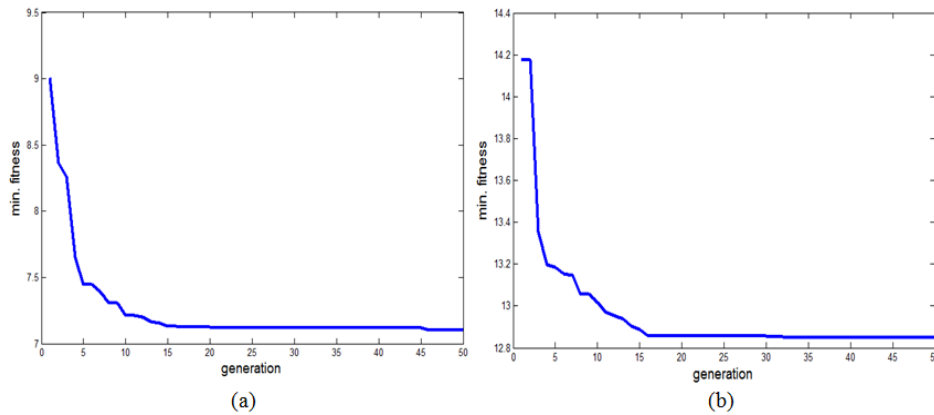


**Fig. 3** – Result histories of the proposed method of the glass substrate handling robot (a) :  $K_J/ K_T = 0.02$  and (b) :  $K_J/ K_T = 0.03$

**Table 3** – Results of the optimal time intervals and the maximum jerks obtained by our proposed method and compared with [8].

$K_J/K_T$	Proposed method				Cong's method [8]			
	$h_i$ (s)	$J_1^{\max}$ ( $^{\circ}/s^3$ )	$J_2^{\max}$ ( $^{\circ}/s^3$ )	$J_3^{\max}$ ( $^{\circ}/s^3$ )	$h_i$ (s)	$J_1^{\max}$ ( $^{\circ}/s^3$ )	$J_2^{\max}$ ( $^{\circ}/s^3$ )	$J_3^{\max}$ ( $^{\circ}/s^3$ )
0.5	11.483	6.33	5.56	6.32	11.484	5.235	6.467	11.60
0.4	10.284	8.71	7.85	8.74	10.976	5.764	7.152	13.83
0.3	9.777	10.22	8.82	10.23	10.262	6.714	8.399	17.85
0.2	8.665	14.78	12.75	14.80	9.371	8.088	10.21	25.94
0.15	8.389	15.99	14.63	16.11	8.939	9.486	11.97	30.31
0.1	7.433	23.86	18.21	23.86	8.111	12.60	15.97	43.40
0.05	6.884	29.66	23.15	30.08	7.13	17.78	25.46	70.65
0.02	6.087	29.94	31.77	50.74	6.72	27.72	46.01	79.28
0	4.896	79.76	58.89	99.86	6.29	99.21	135.6	103.0

Table 3 reports the maximum jerk values resulting from the optimization procedure with different values of weighting coefficients  $K_J/K_T$ ; such values are compared with those yielded by the method proposed by [8]. Considering the value of  $K_J/K_T$  if it is over 0.3 the robot will be put more time for execution of the task and if the value is less of

0.02 the robot will undergo more of vibration in their joints; so the optimal values are between the interval [0.02, 0.3]. It can be noticed that the results yielded by the method described in this paper are well comparable with those provided by the method [8] with respect to the maximum values of velocity and acceleration.

## **7. Conclusion**

This research work deals with optimal trajectory planning using time intervals method to solve the problems of optimal imposed motion of robotics arm.

Minimum objective function computed and it is composed of two terms : the first term is proportional to the total execution time directly affected production efficiency and the latter term is proportional to the maximum jerk of each joint based on the minimax approach that ensures the optimal trajectory is smooth enough, taking into account the main constraints imposed on the robot kinematic (velocity and acceleration) performance. The trajectories were modeled using Cubic splines functions who allow guaranteeing the smoothing of the trajectory and at the same time the continuity of velocities, accelerations and the jerks.

Finally, the proposed method has been run in simulation, taking as input data those found in the work by [8]. Comparison of the results with those provided in [8] has shown that the effectiveness of our method is effective in performing an optimal trajectory planning to solve the problem between high production efficiency and low structure vibration.

This work opens the door for further investigations such as using the B-Spline functions or Non Uniform Rational B-Spline (NURBS) functions and considering an obstacle in workspace and taking account the dynamic constraints of the industrial robots, so as to evaluate the applicability the proposed method and its results.

## **REFERENCES**

- [1] Gasparetto, A., Zanatto, V., 2007. A New Method for Smooth Trajectory Planning of Robot Manipulators, *Mechanism and Machine Theory* 42, p455-471.
- [2] Gasparetto, A., Zanatto, V., 2008. A technique for time-jerk optimal planning of robot trajectories, *Robotics and Computer-Integrated Manufacturing* 24, 415–426.
- [3] Piazzzi, A., Visioli, A., 2000. Global minimum-jerk trajectory planning of robot manipulators, *IEEE Transactions on Industrial Electronics* 47 (1), 140-149.
- [4] Lin, H., 2014. A Fast and Unified Method to Find a Minimum-Jerk Robot Joint Trajectory Using Particle Swarm Optimization, *Journal of Intelligent & Robotic Systems - Springer*.
- [5] Lin, H., Liu, Y. C., 2011. “Minimum-Jerk Robot Joint Trajectory Using Particle Swarm Optimization,” *First International Conference on Robot, Vision and Signal Processing*.
- [6] Zanotto, V., Gasparetto, A., Lanzutti, A., Boscariol, P., Vidoni, R., 2011. Experimental Validation of Minimum Time-jerk Algorithms for Industrial Robots, *J Intell Robot Syst*, 64, 197–219.
- [7] Gasparetto, A., Lanzutti, A., Vidoni, R., Zanotto, V., 2012. Experimental Validation and Comparative Analysis of Time-jerk Algorithms for Trajectory Planning, *Robotics and Computer-Integrated Manufacturing* 28, 164-181.

- [8] Cong, M., Xu, X., Xu, P., 2010. Time-jerk synthetic optimal trajectory planning of robot based on fuzzy genetic algorithm, *Int. J. Intelligent Systems Technologies and Applications*, Vol. 8, Nos. 1-4.
- [9] Barre, P. J., Bearee, R., Borne, P., Dumetz, E., 2005. Influence of a jerk controlled movement law on the vibratory behavior of high-dynamics systems. *J. Intell. Robot. Syst.* 42, 275–293.
- [10] Simon, D., Isik, C., 1993. A trigonometric trajectory generator for robotic arms. *Int. J. Control* 57(3), 505–517.
- [11] Lin, C. S., Chang, P. R., Luh, J. Y. S., 1983. Formulation and optimization of cubic polynomial joint trajectories for industrial robots. *IEEE Trans. Autom. Control* 28(12), 1066–1073.

# The prediction of the surface quality based on the stability lobes and the optimization of the cutting parameters in the vibration restraining

Nesrine Melzi <sup>a \*</sup>, Mustapha Temmar <sup>a</sup>, Mohamed Ouali <sup>a</sup>, Abdelkader Melbous <sup>a</sup>

<sup>a</sup> Laboratory of structures, Department of Mechanical Engineering, University of Blida 1, Algeria

## ARTICLE INFO

### Article history :

Received April 2016

Accepted August 2016

### Keywords :

Machining ;

Turning process ;

Cutting parameters ;

Vibrations ;

Stability lobes.

## ABSTRACT

The turning process is one of the best used processes in the mechanical industry. Therefore, the choice of the cutting parameters is very important in order to obtain a good machined surface quality. During the machining operation, the occurrence of vibrations cannot be avoided since these vibrations represent usually the periodic movements of the elastic system around its equilibrium position. The present article proposes to study the chatter vibration during a turning process by using new cutting conditions and using the stability lobes to optimize the surface quality. The main objective is to determine the best solution in the stability area during a turning process where the chatter is nonexistent, because the quality of a final product depends on the stability of the system piece / tool / machine. The proposed work shows its advantages by using a simulation and an experiment work. For the dynamic modeling of our work ; analytical, experimental and numerical methods were used.

©2016 LESI. All rights reserved.

## 1 Introduction

Chatter vibration is the most important problems during machining since it is a kind of self excited vibration common. It is also a vibration of the tool excited by cutting parameters. It originates from the coupling between cutting force and vibration of the work piece-cutting tool-machine system. It also causes a short life of the cutting tool and a poor quality surface.

Chatter vibration is divided in two parts : forced chatter vibration and self excited chatter vibration. The first one is caused by large cutting resistance and the second one is caused by regenerative effect. [1]. [2]. [3]. [4].

Historically, the system vibrations have been known since a long time. Many studies

\*Email : nesrinemeca@yahoo.fr

have been made by different scholars. Taylor was the first who identified the chatter vibration. Tobias and Tlustý were able to explain the causes of these self-sustained vibrations in the case of an orthogonal cutting applied to turning process[5]. [6]. [7].

Thereafter, Merrit and Altintas developed the feedback loop to represent the delay effect that is currently used unanimously by the community. [8]. [9]. These results are the basis of the theory of stability lobes. This theory permits for a selected a rotation speed fixed to choose an axial depth of cut in order to avoid the instability. The development of this method was well adapted to the case of the turning process since the cutting efforts are constant depending on time. In practice, Thevenot showed that the machining causes a gradual removal of the material with a rapid change of its dynamic characteristics. Also, the work piece material has several modes of vibration[10].

Different methods were proposed in order to analyze and control the work piece-cutting tool-machine system. Therefore, and since the choice of the cutting parameters is strongly related to the process of fabrication, it becomes necessary to optimize the machining parameters by using a numerical modeling of machining. To obtain the best conditions of machining, we have to take in consideration three important parameters : the machine tool, the cutting tool and the work piece.

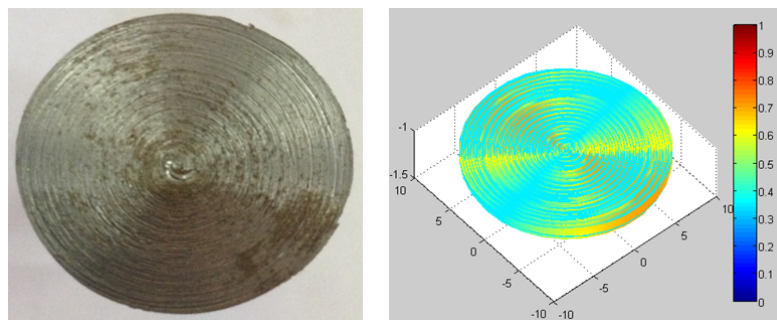


**Fig. 1** – Real image and simulated image of a workpiece.

The dynamic parameters of the turning machine tool, affected by its structure and all the components taking part during the cutting process, play an important role to obtain a perfect machined surface quality. In case of an instable cutting process due to the vibration, the cutting process leads for example to the premature failure of the cutting edge by tool chipping. The machine tool vibration is generated by the interaction of the elastically machining system and the machining process associated to the functioning of the machine tool. This interaction and the machining process constitute the dynamic system of the machining system. Also, this vibration cannot be avoided. It represents periodical movements of the elastic system about its equilibrium position and the value of the displacements depends on the characteristics of all elements of the dynamic system as the intensity of the interaction between these elements. The characteristic parameters of the couple cutting tool-work piece material can be identified whatever the cutting tool geometry.

While applying numerical methods, we use two different approaches : the periodical or analytical and the temporally approach. Several mathematical models have been develo-

ped in order to produce the geometric structure of the machined surfaces such as [11]. These models are established based on a geometric description of the machined surface, the various geometric parameters and the cutting kinematic parameters.

Our literature search allowed us to identify several sets of the existing models in the various machining with metal removal process. [12]. [13]. [14].

These models once developed, allow the study of the machined surface quality and the surface state of the machining parts. In our case, it may be noted that the model does not introduce any interaction between the calculated efforts and the construction of the surface. It means that we should not take into account the bending of the tool due to the cutting efforts. However, this bending tool is a significantly parameter which affects the final texture of the final machined surface quality. The bending tool should easily be considered integrated while we developed our approach.

## 2 Experimental approach

During machining, the stability of the machine tool has an important role. Therefore, we should use the perfect parameters in order to obtain this stability. Among these parameters, we have the rotation speed of the work piece, the displacement of the cutting tool, the exceeded depth, the selected power, the accuracy and the state surface of the work piece.

Our system is modeled by a set composed of mass/spring and where the characteristics of the dynamic system are the mass ( $m$ ), the amortization ( $c$ ) and the stiffness ( $k$ ). In the proposed experience, we used a Heckert parallel turning machine (DZFG 200 with a power of 5.5 KW). The work cylindrical piece material was made by steel XC 48. Its dimensions were 30x100mm.

Our work is based entirely on tests for a cutting tool and a work piece. The goal is to establish a correlation between the cutting parameters and the tool geometry with modeled values (cutting efforts, wear, quality of the surface of the machining part,).

The analytical approach will be detailed in this paragraph for the case of the orthogonal turning process. The system is supposed to admit only one degree of freedom. This approach was addressed and detailed by many scholars. [15]. Others, like Shamoto, presented novel strategies to optimize cutting tool path/posture and to avoid chatter vibration in various machining operations. [16].

The model is represented in figure 2.

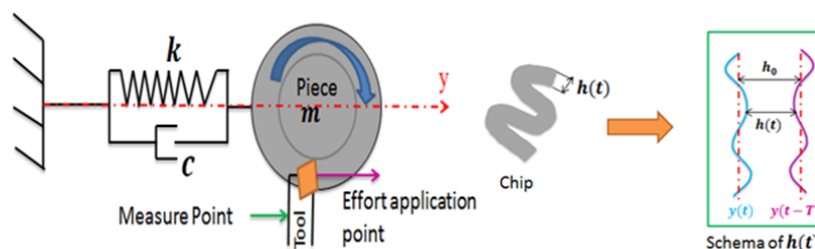


**Fig. 2** – Schematic figure of the turning process.

The dynamic modeling was studied according to the works of Ehmann [17].

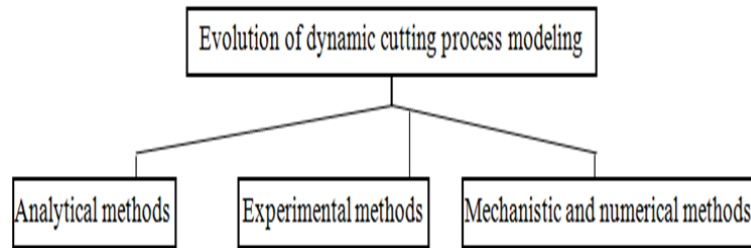


**Fig. 3** – Dynamic model.

The transfer function is obtained by the simplified properties of the block diagrams and by a direct calculation. Different methods using the Nyquist criterion are applied to calculate the stability of the system. For this, we will first consider the case where the cutting tool is sufficiently flexible and the work piece considered sufficiently rigid.

If  $F_f(t)$  = feed effort,

$K_f$  = specifically coefficient of cutting,

$b$  = width of chip

$h(t)$  = the instantaneous thickness of chip,

The dynamic equation becomes :

$$F_f(t) = m\ddot{y}(t) + c\dot{y}(t) + ky(t) \quad (1)$$

$$F_f(t) = K_fbh(t) \quad (2)$$

The expression of instantaneous thickness of chip  $h(t)$  is given by :

$$h(t) = h_0 + [y(t - T) - y(t)] \quad (3)$$

Where :

$h_0$  = nominal thickness of chip,

$T$  = revolution period of the work piece during the turning process,

$[y(t - T) - y(t)]$  = variation thickness of chip.

Therefore :

$$m\ddot{y}(t) + c\dot{y}(t) + ky(t) = K_fb(h_0 + [y(t - T) - y(t)]) \quad (4)$$

Applying Laplace-Carson transform :

$$ms^2y(s) + csy(s) + ky(s) = k_fb[h_0 + (e^{-sT} - 1)y(s)]y(s)[ms^2 + cs + k] = F_f(s) \quad (5)$$

Such as :

$$F_f(s) = K_f b h(s)$$

$$\frac{y(s)}{F_f(s)} = \frac{1}{[ms^2 + cs + k]} = \Psi(s) \tag{6}$$

$$\Leftrightarrow y(s) = F_f(s) \cdot \Psi(s)$$

The transfer function of the system of one degree of freedom  $\Psi(s)$  is therefore :

$$\Psi(s) = \frac{1/k}{\left[ \frac{1}{\omega_n^2} s^2 + \frac{2\xi}{\omega_n} s + 1 \right]} \tag{7}$$

$\xi$  : Damping ratio

$\omega_n$  : Natural frequency

### 3 The study of the stability system

The study of the stability system is done by searching the ratio between the non deformed thickness of the chip  $h_0$  and the average thickness of the chip  $h(s)$ .

For the case where the work piece is considered rigid and the cutting tool is considered flexible, we will calculate the transfer function and the stability by an analytical method. Our method is only used for the case of an orthogonal cut. Then, we will develop the stability criteria's and simulate afterwards.

The determination of  $\frac{h(s)}{h_0}$  :

$$h(s) = h_0 + (e^{-sT} - 1) y(s) \tag{8}$$

With :

$$y(s) = F_f(s) \cdot \Psi(s)$$

$$\text{and } F_f(s) = K_f b h(s)$$

$$\Leftrightarrow \frac{h(s)}{h_0} = \frac{1}{[1 + (1 - e^{-sT})] \cdot K_f b \Psi(s)} \tag{9}$$

This equation allows us to model the dynamic behavior of the turning process as a diagram shown in figure 4.

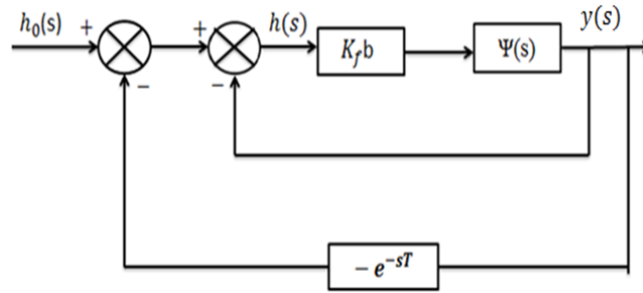


**Fig. 4** – Dynamic model of one degree of freedom for a turning process.

The stability of the transfer function depends on its poles  $s = \sigma + j\omega_c$ .  
 During the critical regime,  $s = j\omega_c$  and  $b = b_{lim}$ .

$$[1 + (1 - e^{-j\omega T})] \cdot K_f b \Psi(j\omega_c) = 0 \tag{10}$$

$$\text{If } \Psi(j\omega) = G + jH \tag{11}$$

$$1 + k_f b_{lim} [G(1 - \cos\omega_c T) - H(\sin\omega_c T)] + j(k_f b_{lim} [G \sin\omega_c T - H[1 - \cos\omega_c T]]) = 0 \tag{12}$$

The rotation speed is expressed as a -function of the chatter pulsation and the phase shift  $\varphi$  :

$$N(\omega_c) = \frac{60\omega_c}{3\pi + 2\varphi(\omega_c) + 2k\pi} \tag{13}$$

The equation 13 is used in order to let the associations of the critical pulsation with the different rotation speeds. From this, we can have a form of a lobe which can be repeated depending on the variation  $K$  ( $K = (1, 2, 3, \dots, n)$ ).

The expression of the depth of the pass limit ( $b_{lim}$ ) is derived from the real part of the characteristic equation :

$$b_{lim} = \frac{-1}{2K_f G(\omega_c)} \tag{14}$$

With :

$$G(\omega_c) = \text{Re}(\Psi(j\omega_c))$$

$\omega_c$  : Pulse chatters (vibration pulsation of the system)

These equations constitute a parameterized system of equations. It is then possible to draw the stability lobes for each vibration mode of the machined face.

Finally, these equations can define the stability limits of our case that is a compliant cutting tool and work piece behavior during machining. Dynamic characteristics of both parameters (cutting tool and work piece) should be identified and substituted in these equations. Afterwards, the stability charts of our process and the optimum cutting conditions can be defined.

## 4 Results

The compliance between the cutting tool and the work piece in a case of a turning process was studied through a system supposed to admit only one degree of freedom. Chatter experiments were conducted in order to verify the proposed stability model. The transfer function is obtained by the simplified properties of the block diagrams and by a direct calculation. Also, the transfer function of the tool and the work piece were measured by the modal test setup. Different experiments were done. The dynamic properties and cutting conditions can be found in Table 1.

**Table 1** – Dynamic properties.

Mass ( $m$ ) Kg	0.55
Dynamical stiffness ( $k$ ) N/m	$23.82 \cdot 10^6$
Dynamic snubbing ( $c$ ) N.s/m	$1.36 \cdot 10^3$
Damping ratio ( $\xi$ )	0.05
Cutting coefficient ( $K_f$ ) MPa	2 400

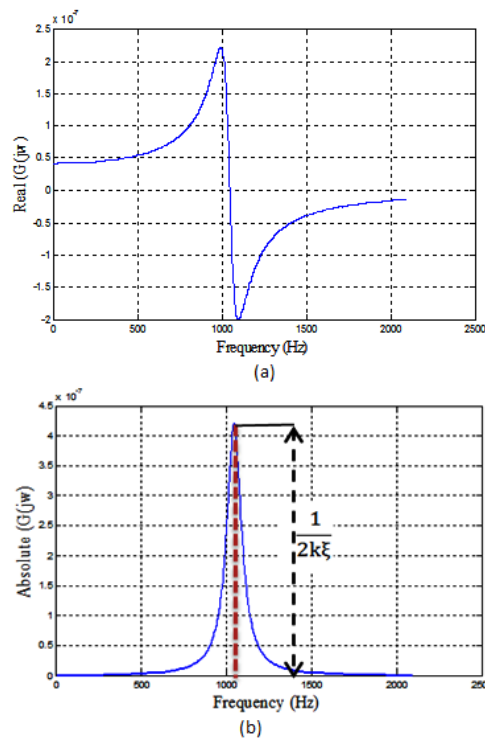


**Fig. 5** – Frequency response function of the cutting : a) real part ; b) magnitude.

Determining the dynamic stiffness was conducted by modeling the work piece in the form of a clamped beam in order to determine analytically its stiffness.

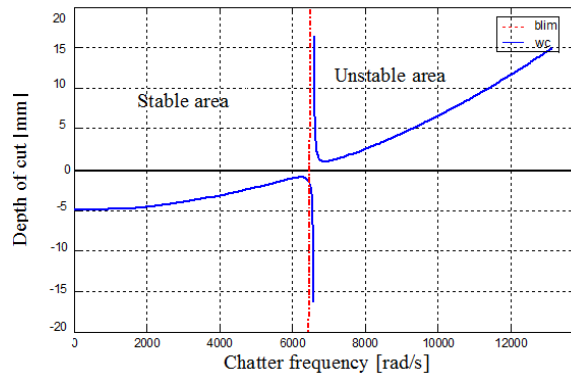
Figure 5 represents the real part of the response function depending on the cutting tool frequency. It is possible to note that the analyzed natural frequency  $f_n$  is close to 1050 Hz.

$f_n$  is calculated by :

$$\omega_n = \sqrt{\frac{k}{m}} \tag{15}$$

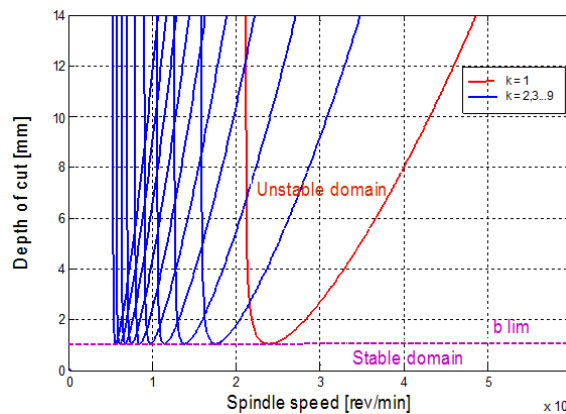
$$\omega_n = 2\pi \cdot f_n$$

$$f_n = \frac{1}{2\pi} \sqrt{\frac{k}{m}}$$



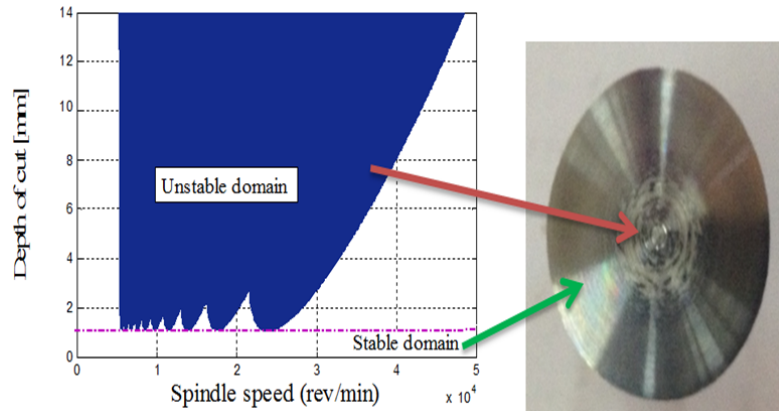
**Fig. 6** –  $b_{lim}$  evolution in function of  $\omega_c$ .

The evolution of  $b_{lim}$  (blimite) depending on  $\omega_c$  gives some negative values which cannot then be conserved.



**Fig. 7** – Stability lobes curves.

Figure 7 shows a good agreement in predicting the unconditionally stable cutting depth at the bottom of each lobe. Stability limits of both models were also in good agreement at low spindle speed. The width of the lobes increases in parallel with the spindle speeds and this is one of the principal criteria of the stability theory. The curves show the evolution of the influence of the different parameters used such as the mass ( $m$ ), the dynamic stiffness ( $k$ ) and the snubbing ( $c$ ) on the stability of the piece-tool-machine system.



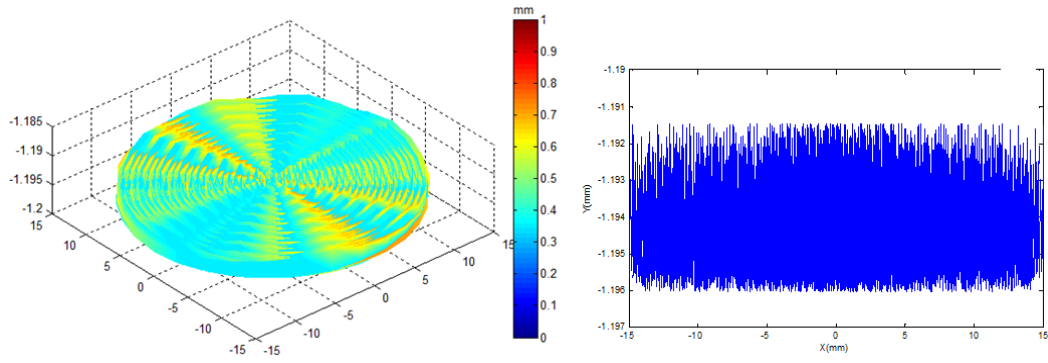
**Fig. 8** – The stable and unstable areas.

Figure 8 shows the stable and unstable areas of the cutting in function of the spindle speed and the depth of cut. At the beginning of our work, we considered that the work piece is considered flexible and the cutting tool is considered rigid. But sometimes, it happens that this assumption cannot be verified, and both of the work piece and the cutting tool are mobile. In this case, the coupling phenomenon can occur if both proper modes of the work piece and the cutting tool are close. We should then vary the spindle speed during machining in order to ensure complete stability of the system. Therefore, the theory of stability that we used before, will not be valid, and we should use one more time the equation 1 but with the new configuration. Indeed, the change of one of the dynamic parameters of the equation 1 requires repeating the whole calculation explained above.

Then, and as a solution, a diagram of the lobes of stability was adopted. Its aspect is shown in the different figures for the proper mode of the cutting tool. Under some conditions of machining, the facing operation is stable. Conversely, beyond certain values, the machining becomes unstable. Under no circumstances, this method predicts the vibration in terms of amplitudes or frequency.

## 5 Illustrative example and result

The stability limits for both cases were determinate after. We did not find a big error for both results. The two examples used for comparison are shown on the system stability lobe diagram in Figure 9 and 10, where example 1 is expected to be unstable, and example 2 is expected to be stable.



**Fig. 9** – Simulated and measured surface topographies for face cutting of the work piece under the cutting conditions :  $N = 6000$  rev/min , depth of cut( $a$ ) = 2 mm,  $f = 0.2$  mm/rev ,  $re = 1.2$  mm (presence of chatter vibration).

Selected points	Cutting conditions		Surface topography of work piece (surface finish)	Virtual image	Results
	N (rev/min)	b (mm)			
a	4000	1.5			Chatter
b	6000	2			Chatter
c	6000	1			Stable
d	20000	0.5			Stable

**Fig. 10** – Verification results of cutting conditions : a,b,c and d.

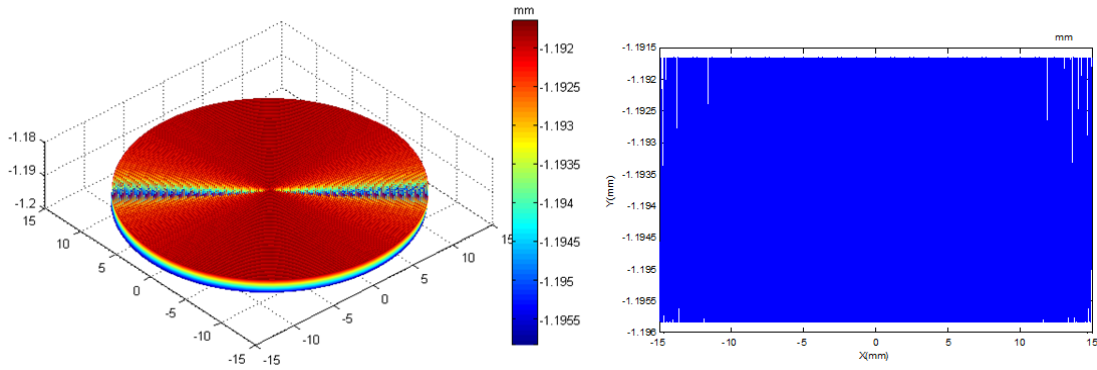


**Fig. 11** – Simulated and measured surface topographies for face cutting of the work piece under the cutting conditions :  $N = 20000$  rev/min , depth of  $cut(a) = 0.5$  mm,  $f = 0.05$  mm/rev,  $re = 1.2$  mm (absence of vibration).

We notice that the cutting parameters during machining affect in a major way on the surface condition. However, proper use of cutting parameters can improve the surface finish, a bad choice of a cutting parameter leads to obtaining a poor surface finish.

We present the use of the intelligent programming with particle swarm Optimization (PSO) , in order to obtain the appropriate machining parameters, so we can minimize the surface roughness.

Several researches have been done about this method, the goal is to take a mathematical approach and solve the machining cutting parameters.

The most important criterion for the assessment of the surface quality is roughness,  $Ra$ , calculated according to :

$$Ra = kV_c^{x_1} * f^{x_2} * a_p^{x_3}$$

Where  $x_1, x_2, x_3$  and  $k$  are the constants relevant to a specific tool-workpiece combination.

In our case, we will apply the experience design method,

This method is one of mathematical methods to obtain maximum information by minimizing the number of experiments to be performed. We are only interested to minimize cutting conditions to find the optimal roughness from the stability lobes plot.

In general form it can be expressed as follows :

$$Ra = function(V_c, a_p, f)$$

To implement our optimization objective and choose the optimum cutting conditions, we measured the surface roughness  $Ra(\mu m)$  using a type TR100 Surface Roughness Tester.

The average values of roughness  $Ra$  measured for each part corresponding to each cutting procedure are presented in the following table :

**Table 2** – values of roughness  $Ra$ .

Pieces	Cutting speed $V_c$ [m/min]	Depth of cut $a_p$ [mm]	Feed rate $f$ [mm/rev]	Roughness $Ra$ [ $\mu\text{m}$ ]
1	150	0.3	0.05	2.85
2	150	0.8	0.2	3.18
3	1000	0.3	0.2	1.48
4	150	0.8	0.05	3.01
5	1000	0.8	0.2	1.39
6	1000	0.8	0.05	1.25
7	1000	0.3	0.05	1.05
8	150	0.3	0.2	2.37

Limiting the cutting tool is very important to the safety of machining; the cutting parameters are limited with the bottom and top allowable limit.

Allowable range of cutting conditions is :

$$150 \leq V_c \leq 1000 \text{ m/min}; 0.05 \leq f \leq 0.2 \text{ mm/rev}; 0.3 \leq a_p \leq 0.8 \text{ mm}$$

With the data processing, our equation is :

$$\left\{ \begin{array}{l} \text{minimize } Ra \\ Ra = 3.45259 - (2.72395e^{-003}V_c) - (0.23804.a_p) - (7.53412.f) \\ + (8.31373e^{-004}e - 004.V_c.a_p) + (0.011561.V_c.f) + (10.87843.a_p.f) - (0.014745.V_c.a_p.f) \\ \text{with} \\ 0.05 \leq f \leq 0.2 \\ 0.3 \leq a_p \leq 0.8 \\ 150 \leq V_c \leq 1000 \end{array} \right.$$

The best result is :  $f = 0.1$  mm/tr,  $a_p = 0.3$ mm ,  $V_c = 1000$  m/min ,  $Ra = 1$   $\mu\text{m}$

## 6 Conclusion

In this study, dynamic characteristics of the cutting tool and the work piece were taken into account in order to obtain the best approach of the physical phenomena during vibration. We were interested in the prediction of the lobes of stability with regard to the vibration instability through a dynamic model. For the dynamic modeling of our work ; analytical, experimental and numerical methods were used.

Our model provides an approach to the dynamic system by solving the stability limit. The effect of the process parameters on the stability is demonstrated. This process is verified by a simulation method and overall, the results are the same. Several trails were carried out for the verification of our method. The obtained results show a perfect agreement with the theory of the lobe of stability since the width of the lobes increases according to the rotation speeds. Also, the measurement of surface roughness allowed us

to qualify the quality of machining, for that you optimize cutting conditions to avoid appearances of vibrations and surface defects.

The reliability of the proposed mathematical model has been tested by the optimization (PSO) method. The results showed that the model is highly significant and good fit with the stability lobe path and also with the experimental results.

## REFERENCES

- [1] H. Chen, D. Li, S. Huang and P. Fu, Study on the cutting force prediction of supercritical material milling, ICNC, Vol. 3, pp.1148–1152, 2010
- [2] Y.Lakinuma, Y.SudoS and T.Aoyama, Detection of chatter vibration in end milling applying disturbance observer, Annals of the CIRP, Vol 60, N° 1, pp 109-112, 2011
- [3] E. Shamoto, K. Akawzawa, Analytical prediction of chatter Stability in ball end milling with tool inclination, CIRP annals, Vol 58 N° 1, pp 351-354, 2009
- [4] Y.Altintas,Z.M.Kilic,Generalizeddynamicmodelofmetalcuttingoperations,CIRP Annals, Vol. 62, No. 1, pp. 47–50, 2013
- [5] S.A. Tobias, W. Fishwick, A Theory of Regenerative Chatter, The Engineer, 1958
- [6] J. Tlusty, M. Polacek, The stability of machine tools against self excited vibrations in machining, Int. Res, 465-474, 1963
- [7] F.W.Taylor, On the art of cutting metals, Transactions of the American Society of Mechanical Engineers, pp. 31–35, 1907
- [8] H.E. Merritt, Theory of Self-Excited Machine Tool Chatter, ASME J. Eng. Industry 87, pages 447–454, 1965
- [9] Y. Altintas. Manufacturing Automation, Metal Cutting Mechanics, Machine Tool Vibration and CNC Design. Cambridge University, ISBN-13 : 978-0521659734, 2000
- [10] V.Thevenot V, L.Arnaud, G.Dessein, G.Cazenave-Larroche, Influence of material removal on dynamic behavior of thin walled structure in peripheral milling, Machining Science and Technology 10, pages 275-287, 2006
- [11] M.C.Shaw., Metal cutting principles, Oxford university press, 2004
- [12] C.Peng, L.Wang, T.W.Liao, A new method for the prediction of chatter stability lobes based on dynamic cutting force simulation model and support vector machine, Journal of sound and vibration, Elsevier, 2015
- [13] M.Mousseigne, Y.Landon, S.Seguy, G.Dessein, J.M.redonnet, Predicting the dynamic behavior of torus milling tools when climb milling using the stability lobes theory, International journal of machine tools and manufacture, Elsevier, 2012
- [14] A.Otto, S.Rauh, M.Kolouch, G.Radons, Extension of Tlusty’s law for the identification of chatter stability lobes in multi-dimensional cutting processes, International journal of machine tools and manufacture, Elsevier, 2014
- [15] M. Segreti, Vibrations en coupe orthogonale, Modélisation, étude de stabilité et validation expérimentale, Thèse, Université de Metz, 2002
- [16] E.Shamoto, S.Fujimaki, B.Sencer, N.Suuki, T.Kato, R.Hino, A novel tool path/posture optimization concept to avoid chatter vibration in machining – Proposed concept and its verification in turning, CIRP Annals, Manufacturing Technology, Volume 61, Issue 1, pages 331–334, 2012
- [17] K.F.Ehmann, S.G.Kapoor, R.E.Devor and I.Lazoglu, Machining process modeling, A

review, *Journal of manufacturing science and engineering*, vol 119/4B, pages 655-663, 1997.

# On Some Fractional Integral Inequalities Involving Generalized Riemann-Liouville Fractional Integral Operator

Mohamed Houas<sup>a\*</sup>, Mohamed Bezzou<sup>a</sup>

<sup>a</sup> Laboratory FIMA, UDBKM, University of Khemis Miliana, Algeria.

## ARTICLE INFO

### Article history :

Received April 2016

Accepted September 2016

### Keywords :

Riemann-Liouville integral ;

Fractional integration ;

Integral inequalities ;

Positive functions.

## ABSTRACT

In this paper, the generalized Riemann-Liouville fractional integral operator is used to generate some new fractional integral inequalities. By using the generalized Riemann-Liouville fractional integral operator, we also generate new classes of fractional integral inequalities using a family of  $n$ , ( $n \geq 1$ ) positive functions.

©2016 LESI. All rights reserved.

## 1. Introduction

Integral inequalities play a very important role in the theory of differential equations and applied mathematics. These inequalities have gained considerable popularity and importance during the past few decades due to their distinguished applications in numerical quadrature, transform theory, probability, and statistical problems. For details, we refer to [ 8, 9, 10, 11, 12, 14, 16, 18] and the references therein. Moreover, the study of fractional type inequalities is also of great importance. A detailed account of such fractional integral inequalities along with their applications can be found in the research contributions by many author see [ 1, 3, 4, 13, 19]. In the past several years, many author have studied on fractional integral inequalities using Riemann-Liouville, Hadamard fractional integral and  $q$ -fractional integral, see [ 2, 5, 6, 17]. In this paper we present some new fractional integral inequalities using generalized Riemann-Liouville fractional integral.

## 2. Preliminaries

Firstly, we give some necessary definitions and mathematical preliminaries of fractional calculus theory which are used further in this paper.

\*Email : houasmed@yahoo.fr

**Definition 1** A real valued function  $f(t)$ ,  $t \geq 0$  is said to be in the space  $\mathbb{C}_v(0, \infty)$ ,  $v \in \mathbb{R}$ , if there exists a real number  $p > v$  such that  $f(t) = t^p f_1(t)$ , where  $f_1(t) \in \mathbb{C}([0, \infty[)$ .

**Definition 2** A function  $f(t)$ ,  $t > 0$  is said to be in the space  $\mathbb{C}_v^n$ ,  $n \in \mathbb{R}$ , if  $f^{(n)} \in \mathbb{C}_v$ .

**Definition 3** The Riemann-Liouville fractional integral operator of order  $\alpha \geq 0$ , for a continuous function  $f$  on  $[a, b]$  is defined as

$$J_a^\alpha [f(t)] = \frac{1}{\Gamma(\alpha)} \int_a^t (t - \tau)^{\alpha-1} f(\tau) d\tau, \quad \alpha > 0, \quad a < t \leq b, \tag{2.1}$$

$$J_a^0 [f(t)] = f(t),$$

$$\text{where } \Gamma(\alpha) := \int_0^\infty e^{-u} u^{\alpha-1} du.$$

For the convenience of establishing the results, we give the following properties :

$$J_a^\alpha J_a^\beta [f(t)] = J_a^{\alpha+\beta} [f(t)], \tag{2.2}$$

and

$$J_a^\alpha J_a^\beta [f(t)] = J_a^\beta J_a^\alpha [f(t)]. \tag{2.3}$$

**Definition 4** Consider the space  $L_{p,k}(a, b)$  ( $k \geq 0$ ,  $1 \leq p < \infty$ ) of those real-valued Lebesgue measurable functions  $f$  on  $[a, b]$  for which

$$\|f\|_{L_{p,k}(a,b)} = \left( \int_a^b |f(x)|^p x^k dx \right)^{\frac{1}{p}} < \infty, \quad k \geq 0, \quad 1 \leq p < \infty. \tag{2.4}$$

**Definition 5** Consider the space  $X_c^p(a, b)$  ( $c \in \mathbb{R}$ ,  $1 \leq p < \infty$ ) of those real-valued Lebesgue measurable functions  $f$  on  $[a, b]$  for which

$$\|f\|_{X_c^p(a,b)} = \left( \int_a^b |x^c f(x)|^p \frac{dx}{x} \right)^{\frac{1}{p}} < \infty, \quad c \in \mathbb{R}, \quad 1 \leq p < \infty, \tag{2.5}$$

and for the case  $p = \infty$

$$\|f\|_{X_c^\infty} = \text{ess sup}_{a \leq x \leq b} [x^c f(x)], \quad c \in \mathbb{R}. \tag{2.6}$$

In particular, when  $c = \frac{k+1}{p}$  ( $k \geq 0$ ,  $1 \leq p < \infty$ ) the space  $X_c^p(a, b)$  coincides with the  $L_{p,k}(a, b)$  -space and also if we take  $c = \frac{1}{p}$  ( $1 \leq p < \infty$ ) the space  $X_c^p(a, b)$  coincides with the classical  $L^p(a, b)$  -space.

**Definition 6** Let  $f \in L_{1,k}[a, b]$ . The generalized Riemann-Liouville fractional integral  $J_a^{\alpha,k}$  of order  $\alpha \geq 0$  and  $k \geq 0$  is defined by

$$J_a^{\alpha,k} f(t) = \frac{(k+1)^{1-\alpha}}{\Gamma(\alpha)} \int_a^t (t^{k+1} - \tau^{k+1})^{\alpha-1} \tau^k f(\tau) d\tau, \quad \alpha > 0, \quad a < t \leq b, \tag{2.7}$$

$$J_a^{0,k} [f(t)] = f(t),$$

For more details on can consult [ 7, 10, 13].

### 3. Main Results

In this section, we prove some inequalities concerning the generalized Riemann-Liouville fractional integral.

**Theorem 7** *Let  $f, h$  and  $g$  be three positive continuous functions on  $[a, b]$ , such that*

$$h(x) \frac{f(y)}{g(y)} + h(y) \frac{f(x)}{g(x)} \geq h(x) \frac{f(x)}{g(x)} + h(y) \frac{f(y)}{g(y)}; \quad x, y \in [a, t], \quad a < t \leq b. \quad (3.1)$$

*Then the generalized fractional integral inequality*

$$J_a^{\alpha,k} [g(t)] J_a^{\alpha,k} [f(t) h(t)] \leq J_a^{\alpha,k} [f(t)] J_a^{\alpha,k} [h(t) g(t)], \quad (3.2)$$

*holds for all  $a < t \leq b$ ,  $\alpha > 0$ ,  $k \geq 0$ .*

**Proof.** Suppose that  $f, h$  and  $g$  are positive and continuous functions on  $[a, b]$  satisfying the condition (3.1). Then we define

$$\begin{aligned} \phi(x, y) := & \varphi_\alpha^k(t, x) (f(y) g(x) h(x) + g(y) h(y) f(x) \\ & - g(y) h(x) f(x) - h(y) f(y) g(x)). \end{aligned} \quad (3.3)$$

where,

$$\varphi_\alpha^k(t, x) := \frac{(k+1)^{1-\alpha}}{\Gamma(\alpha)} (t^{k+1} - x^{k+1})^{\alpha-1} x^k, \quad (3.4)$$

It is clear that

$$\phi(x, y) \geq 0. \quad (3.5)$$

Integrating (3.5) with respect to  $x$  over  $(a, t)$ , yields

$$\begin{aligned} & 0 \leq \int_a^t \phi(x, y) dx \\ & = \int_a^t \varphi_\alpha^k(t, x) (f(y) g(x) h(x) + g(y) h(y) f(x) \\ & \quad - g(y) h(x) f(x) - h(y) f(y) g(x)) dx \\ & = J_a^{\alpha,k} [g(t) h(t)] f(y) + J_a^{\alpha,k} [f(t)] g(y) h(y) \\ & \quad - J_a^{\alpha,k} [h(t) f(t)] g(y) - J_a^{\alpha,k} [g(t)] h(y) f(y). \end{aligned} \quad (3.6)$$

Now, multiplying (3.6) by  $\varphi_\alpha^k(t, y)$ ,  $y \in (a, t)$ ,  $a < t \leq b$  and integrating with respect to  $y$  over  $(a, t)$ , we can write

$$\begin{aligned}
 0 &\leq \int_a^t \int_a^t \varphi_\alpha^k(t, y) \phi(x, y) dx dy \\
 &= \int_a^t \int_a^t \varphi_\alpha^k(t, y) \varphi_\alpha^k(t, x) (f(y)g(x)h(x) + g(y)h(y)f(x) \\
 &\quad - g(y)h(x)f(x) - h(y)f(y)g(x)) dx dy \\
 &= J_a^{\alpha,k} [g(t)h(t)] \int_a^t \varphi_\alpha^k(t, y) f(y) dy + J_a^{\alpha,k} [f(t)] \int_a^t \varphi_\alpha^k(t, y) g(y)h(y) dy \\
 &\quad - J_a^{\alpha,k} [h(t)f(t)] \int_a^t \varphi_\alpha^k(t, y) g(y) dy - J_a^{\alpha,k} [g(t)] \int_a^t \varphi_\alpha^k(t, y) h(y)f(y) dy \\
 &= 2J_a^{\alpha,k} [g(t)h(t)] J_a^{\alpha,k} [f(t)] - 2J_a^{\alpha,k} [h(t)f(t)] J_a^{\alpha,k} [g(t)]
 \end{aligned} \tag{3.7}$$

This implies that

$$J_a^{\alpha,k} [gh(t)] J_a^{\alpha,k} [f(t)] \geq J_a^{\alpha,k} [hf(t)] J_a^{\alpha,k} [g(t)] \tag{3.8}$$

The proof is completed.

Our next result is the following theorem, in which we use two fractional positive parameters.

**Theorem 8** *Let  $f, h$  and  $g$  be three positive continuous functions on  $[a, b]$ . Then, the following generalized fractional inequality*

$$\begin{aligned}
 &J_a^{\alpha,k} [h(t)f(t)] J_a^{\beta,k} [g(t)] - J_a^{\alpha,k} [g(t)] J_a^{\beta,k} [h(t)f(t)] \\
 &\leq J_a^{\alpha,k} [g(t)h(t)] J_a^{\beta,k} [f(t)] + J_a^{\alpha,k} [f(t)] J_a^{\beta,k} [g(t)h(t)],
 \end{aligned} \tag{3.9}$$

is valid for all  $a < t \leq b$ ,  $\alpha > 0$ ,  $\beta > 0$ ,  $k \geq 0$ .

**Proof.** Multiplying both sides of (3.5) by the quantity  $\varphi_\beta^k(t, y)$ ,  $y \in (a, t)$ ,  $a < t \leq b$ , then integrating the resulting inequality with respect to  $y$  over  $(a, t)$  we get

$$\begin{aligned}
 0 &\leq \int_a^t \int_a^t \varphi_\beta^k(t, y) \phi(x, y) dx dy & (3.10) \\
 &= \int_a^t \int_a^t \varphi_\beta^k(t, y) \varphi_\alpha^k(t, x) (f(y)g(x)h(x) + g(y)h(y)f(x) \\
 &\quad - g(y)h(x)f(x) - h(y)f(y)g(x)) dx dy \\
 &= J_a^{\alpha,k} [g(t)h(t)] \int_a^t \varphi_\beta^k(t, y) f(y) dy + J_a^{\alpha,k} [f(t)] \int_a^t \varphi_\beta^k(t, y) g(y)h(y) dy \\
 &\quad - J_a^{\alpha,k} [h(t)f(t)] \int_a^t \varphi_\beta^k(t, y) g(y) dy - J_a^{\alpha,k} [g(t)] \int_a^t \varphi_\beta^k(t, y) h(y)f(y) dy \\
 &= J_a^{\alpha,k} [g(t)h(t)] J_a^{\beta,k} [f(t)] + J_a^{\alpha,k} [f(t)] J_a^{\beta,k} [g(t)h(t)] \\
 &\quad - J_a^{\alpha,k} [h(t)f(t)] J_a^{\beta,k} [g(t)] - J_a^{\alpha,k} [g(t)] J_a^{\beta,k} [h(t)f(t)].
 \end{aligned}$$

This implies that

$$\begin{aligned}
 &J_a^{\alpha,k} [gh(t)] J_a^{\beta,k} [f(t)] + J_a^{\alpha,k} [f(t)] J_a^{\beta,k} [gh(t)] & (3.11) \\
 &\geq J_a^{\alpha,k} [hf(t)] J_a^{\beta,k} [g(t)] - J_a^{\alpha,k} [g(t)] J_a^{\beta,k} [hf(t)].
 \end{aligned}$$

Theorem 8 is thus proved.

**Remark 9** Applying Theorem 8 for  $\alpha = \beta$ , we obtain Theorem 7.

Now, we shall propose a new generalization of integral inequalities using a family of  $n$  positive functions defined on  $[a, b]$ .

**Theorem 10** Let  $f, h$  and  $g_i, i = 1, \dots, n$  be positive and continuous functions on  $[a, b]$ . Then, the following fractional inequality

$$\begin{aligned}
 &J_a^{\alpha,k} \left[ \prod_{i=1}^n g_i(t) \right] J_a^{\alpha,k} \left[ h(t)f(t) \prod_{i \neq q}^n g_i(t) \right] & (3.12) \\
 &\leq J_a^{\alpha,k} \left[ f(t) \prod_{i \neq q}^n g_i(t) \right] J_a^{\alpha,k} \left[ h(t) \prod_{i=1}^n g_i(t) \right],
 \end{aligned}$$

is valid for any  $a < t \leq b$ ,  $\alpha > 0$ ,  $k \geq 0$ .

**Proof.** Suppose that  $f, h$  and  $g_i, i = 1, \dots, n$  are positive continuous functions on  $[a, b]$ , then we can write

$$h(x) \frac{f(y)}{g_q(y)} + h(y) \frac{f(x)}{g_q(x)} \geq h(x) \frac{f(x)}{g_q(x)} + h(y) \frac{f(y)}{g_q(y)}, \tag{3.13}$$

for any fixed  $q \in \{1, \dots, n\}$  and for any  $x, y \in [a, t]$ ,  $a < t \leq b$ .

Denote

$$\begin{aligned} \phi_q(x, y) := & \\ \varphi_\alpha^k(t, x) \left( f(y) \prod_{i \neq q}^n g_i(y) h(x) \prod_{i=1}^n g_i(x) + h(y) \prod_{i=1}^n g_i(y) f(x) \prod_{i \neq q}^n g_i(x) \right. & \quad (3.14) \\ & \left. - \prod_{i=1}^n g_i(y) h(x) f(x) \prod_{i \neq q}^n g_i(x) - h(y) f(y) \prod_{i \neq q}^n g_i(y) \prod_{i=1}^n g_i(x) \right), \end{aligned}$$

for all  $x, y \in [a, t]$ ,  $a < t \leq b$  and for any fixed integer  $q \in \{1, \dots, n\}$ .

We have

$$\phi_q(x, y) \geq 0. \tag{3.15}$$

Now, integrating (3.15) with respect to  $x$  over  $(a, t)$ , we obtain

$$\begin{aligned} 0 & \leq \int_a^t \phi_q(x, y) dx \\ & = f(y) \prod_{i \neq q}^n g_i(y) J_a^{\alpha, k} [h(t) \prod_{i=1}^n g_i(t)] \\ & + h(y) \prod_{i=1}^n g_i(y) J_a^{\alpha, k} [f(t) \prod_{i \neq q}^n g_i(t)] \\ & - \prod_{i=1}^n g_i(y) J_a^{\alpha, k} [h(t) f(t) \prod_{i \neq q}^n g_i(t)] \\ & - h(y) f(y) \prod_{i \neq q}^n g_i(y) J_a^{\alpha, k} [\prod_{i=1}^n g_i(t)]. \end{aligned} \tag{3.16}$$

Next, multiplying both sides of (3.16) by  $\varphi_\alpha^k(t, y)$ ,  $y \in (a, t)$ , integrating the resulting inequality with respect to  $y$  from  $a$  to  $t$ , we can write

$$\begin{aligned} 0 & \leq \int_a^t \int_a^t \varphi_\alpha^k(t, y) \phi_q(x, y) dx dy \\ & = J_a^{\alpha, k} [f(t) \prod_{i \neq q}^n g_i(t)] J_a^{\alpha, k} [h(t) \prod_{i=1}^n g_i(t)] \\ & + J_a^{\alpha, k} [h(t) \prod_{i=1}^n g_i(t)] J_a^{\alpha, k} [f(t) \prod_{i \neq q}^n g_i(t)] \\ & - J_a^{\alpha, k} [\prod_{i=1}^n g_i(t)] J_a^{\alpha, k} [h(t) f(t) \prod_{i \neq q}^n g_i(t)] \\ & - J_a^{\alpha, k} [h(t) f(t) \prod_{i \neq q}^n g_i(t)] J_a^{\alpha, k} [\prod_{i=1}^n g_i(t)]. \end{aligned} \tag{3.17}$$

and consequently, we have

$$\begin{aligned} 0 & \leq 2J_a^{\alpha, k} \left[ f(t) \prod_{i \neq q}^n g_i(t) \right] J_a^{\alpha, k} \left[ h(t) \prod_{i=1}^n g_i(t) \right] \\ & - 2J_a^{\alpha, k} \left[ \prod_{i=1}^n g_i(t) \right] J_a^{\alpha, k} \left[ h(t) f(t) \prod_{i \neq q}^n g_i(t) \right]. \end{aligned} \tag{3.18}$$

The proof is completed.

Using two fractional parameters, we obtain the following generalization of Theorem 10.

**Theorem 11** *Let  $f, h$  and  $g_i, i = 1, \dots, n$  be positive continuous functions on  $[a, b]$ . Then, for any fixed  $q \in \{1, \dots, n\}$  and for all  $a < t \leq b, \alpha > 0, \beta > 0, k \geq 0$ , we have*

$$\begin{aligned}
 & J_a^{\alpha,k} \left[ \prod_{i=1}^n g_i(t) \right] J_a^{\beta,k} \left[ h(t) f(t) \prod_{i \neq q}^n g_i(t) \right] \\
 & + J_a^{\beta,k} \left[ \prod_{i=1}^n g_i(t) \right] J_a^{\alpha,k} \left[ h(t) f(t) \prod_{i \neq q}^n g_i(t) \right] \\
 & \leq J_a^{\alpha,k} \left[ f(t) \prod_{i \neq q}^n g_i(t) \right] J_a^{\beta,k} \left[ h(t) \prod_{i=1}^n g_i(t) \right] \\
 & + J_a^{\beta,k} \left[ f(t) \prod_{i \neq q}^n g_i(t) \right] J_a^{\alpha,k} \left[ h(t) \prod_{i=1}^n g_i(t) \right].
 \end{aligned} \tag{3.19}$$

**Proof.** Multiplying both sides of (3.16) by  $\varphi_\beta^k(t, y), y \in (a, t)$ , and integrating with respect to  $y$  from  $a$  to  $t$ , we obtain

$$\begin{aligned}
 0 & \leq \int_a^t \int_a^t \varphi_\beta^k(t, y) \phi_q(x, y) dx dy \\
 & = \int_a^t \int_a^t \varphi_\beta^k(t, y) f(y) \prod_{i \neq q}^n g_i(y) \varphi_\alpha^k(t, x) h(x) \prod_{i=1}^n g_i(x) dx dy \\
 & \quad + \int_a^t \int_a^t \varphi_\beta^k(t, y) h(y) \prod_{i=1}^n g_i(y) \varphi_{\alpha,\theta}^k(t, x) f(x) \prod_{i \neq q}^n g_i(x) dx dy \\
 & \quad - \int_a^t \int_a^t \varphi_\beta^k(t, y) \prod_{i=1}^n g_i(y) \varphi_\alpha^k(t, x) h(x) f(x) \prod_{i \neq q}^n g_i(x) dx dy \\
 & \quad - \int_a^t \int_a^t \varphi_\beta^k(t, y) h(y) f(y) \prod_{i \neq q}^n g_i(y) \varphi_\alpha^k(t, x) \prod_{i=1}^n g_i(x) dx dy.
 \end{aligned} \tag{3.20}$$

It follows that

$$\begin{aligned}
 0 & \leq J_a^{\alpha,k} \left[ f(t) \prod_{i \neq q}^n g_i(t) \right] J_a^{\beta,k} \left[ h(t) \prod_{i=1}^n g_i(t) \right] \\
 & \quad + J_a^{\beta,k} \left[ f(t) \prod_{i \neq q}^n g_i(t) \right] J_a^{\alpha,k} \left[ h(t) \prod_{i=1}^n g_i(t) \right] \\
 & \quad - J_a^{\alpha,k} \left[ \prod_{i=1}^n g_i(t) \right] J_a^{\beta,k} \left[ h(t) f(t) \prod_{i \neq q}^n g_i(t) \right] \\
 & \quad - J_a^{\beta,k} \left[ \prod_{i=1}^n g_i(t) \right] J_a^{\alpha,k} \left[ h(t) f(t) \prod_{i \neq q}^n g_i(t) \right].
 \end{aligned} \tag{3.21}$$

This completes the proof.

**Remark 12** *If we take  $\alpha = \beta$ , in Theorem 11, we obtain Theorem 10.*

## REFERENCES

- [1] S. Belarbi and Z. Dahmani, On some new fractional integral inequalities, *J. Inequal. Pure Appl. Math.* 10(3) (2009) pp 1-12.
- [2] V. L. Chinchane and D. B. Pachpatte, A note on some integral inequalities via Hadamard integral, *Journal of Fractional Calculus and Applications.* 4 (2013) 1-5.
- [3] Z. Dahmani, New inequalities in fractional integrals, *International Journal of Nonlinear Sciences.* 9(4) (2010) pp 493-497.
- [4] Z. Dahmani and N. Bedjaoui, New generalized integral inequalities, *J. Advan. Res. Appl. Math.* 3(4) (2011) pp 58–66.
- [5] Z. Dahmani and A. Benzidane, New inequalities using  $Q$ -fractional theory, *Bull. Math. Anal. Appl.* 4 (2012) pp 190-196 .
- [6] Z. Dahmani, New classes of integral inequalities of fractional order, *Le Matematiche.* (2014) pp 227–235.
- [7] R. Gorenflo and F. Mainardi, *Fractional calculus : integral and differentiable equations of fractional order*, Springer, Verlag, Wien, 1997).
- [8] M. Houas, Some inequalities for  $k$ -fractional continuous random variables, *J. Advan. Res. In Dynamical and Control Systems.* 7(4) (2015) pp 43-50.
- [9] M. Houas, Some integral inequalities involving Saigo fractional integral operators. Accepted.
- [10] M. Houas, Some weighted integral inequalities for Hadamard fractional integral Operators. Accepted.
- [11] U. Katugampola, New approach to a generalized fractional integral, *Appl. Math. Comput.* 218(3) (2011) pp 860–865.
- [12] P. Kumar, Inequalities involving moments of a continuous random variable defined over a finite interval, *Computers and Mathematics with Applications.* 48 (2004) pp 257-273.
- [13] W. Liu, Q. A. Ngo and V. N. Huy, Several interesting integral inequalities, *Journal of Math. Inequal.* 3(2) (2009) pp 201–212.
- [14] M. A. Noor, M. U. Awan and K. I. Noor, On some inequalities for relative semi-convex functions, *Journal of Inequal and Appl.* 332 (2013) pp 1-16 .
- [15] S. G. Samko, A. A Kilbas, and O. I. Marichev, *Fractional integrals and derivatives, Theory and Application*, Gordon and Breach Science, New York, 1993.
- [16] M. Z. Sarikaya and H. Yaldiz, Note on the Ostrowski type inequalities for fractional integrals. *Vietnam. J. Math.* 41(4), (2013) pp 2-6 .
- [17] M. Z. Sarikaya and H. Yaldiz, New generalization fractional inequalities of Ostrowski-Gruss type, *Lobachevskii Journal of Mathematics* 34(4) (2013) pp 326-331.
- [18] D. Ucar and A. Deniz, Generalizations of holder's inequalities on time scales, *Journal of Math. Inequal.* 9(1) (2015) pp 247–255.
- [19] H. Yildirim and Z. Kirtay, Ostrowski inequality for generalized fractional integral and related inequalities, *Malaya Journal of Matematik.* 2(3) (2014) pp 322-329.

# A problem of spherical cavity in an infinite generalized thermoelastic medium with double porosity subjected to moving heat source

Rajneesh Kumar <sup>a \*</sup>, Richa Vohra <sup>b †</sup>

<sup>a</sup> Department of Mathematics, Kurukshetra University, Kurukshetra, Haryana, India

<sup>b</sup> Department of Mathematics & Statistics, H.P. University, Shimla, HP, India

## ARTICLE INFO

### Article history :

Received May 2016

Accepted September 2016

### Keywords :

Double porosity ;

Lord-Shulman theory ;

Spherical cavity ;

Moving heat source.

## ABSTRACT

This paper is concerned with the investigation of thermoelastic interactions in an isotropic unbounded medium with spherical cavity due to the presence of moving heat source in context of linear theory of thermoelasticity with one relaxation time [1]. Laplace transform technique has been used to obtain the expressions for radial stress, equilibrated stresses and temperature distribution. A numerical inversion technique has been applied to recover the resulting quantities in the physical domain. The components of stress and temperature distribution are depicted graphically to show the effect of heat source velocity and the relaxation time parameters. Some particular cases are also deduced from the present investigation.

©2016 LESI. All rights reserved.

## 1. Introduction

Porous media theories play an important role in many branches of engineering including material science, the petroleum industry, chemical engineering, biomechanics and other such fields of engineering. Biot [2] proposed a general theory of three-dimensional deformation of fluid saturated porous salts. One important generalization of Biot's theory of poroelasticity that has been studied extensively started with the works by Barenblatt et al. [3], where the double porosity model was first proposed to express the fluid flow in hydrocarbon reservoirs and aquifers.

The double porosity model represents a new possibility for the study of important problems concerning the civil engineering. It is well-known that, under super-saturation conditions due to water of other fluid effects, the so called neutral pressures generate unbearable stress states on the solid matrix and on the fracture faces, with severe (so-

\*Email : rajneesh\_kuk@rediffmail.com

†Email : richavhr88@gmail.com

metimes disastrous) instability effects like landslides, rock fall or soil fluidization (typical phenomenon connected with propagation of seismic waves). In such a context it seems possible, acting suitably on the boundary pressure state, to regulate the internal pressures in order to deactivate the noxious effects related to neutral pressures; finally, a further but connected positive effect could be lightening of the solid matrix/fluid system .

Aifantis[4-7] introduced a multi-porous system and studied the mechanics of diffusion in solids Wilson and Aifantis [8] presented the theory of consolidation with the double porosity. Khaled et. al [9] employed a finite element method to consider the numerical solutions of the differential equation of the theory of consolidation with double porosity developed by Wilson and Aifantis [8]. Wilson and Aifantis[10]discussed the propagation of acoustics waves in a fluid saturated porous medium. The propagation of acoustic waves in a fluid-saturated porous medium containing a continuously distributed system of fractures is discussed. The porous medium is assumed to consist of two coexisting degrees of porosity and the resulting model thus yields three types of longitudinal waves, one associated with the elastic properties of the matrix material and one each for the fluids in the pore space and the fracture space.

Nunziato and Cowin [11]developed a nonlinear theory of elastic material with voids. Later, Cowin and Nunziato [12]developed a theory of linear elastic materials with voids for the mathematical study of the mechanical behavior of porous solids. They also considered several applications of the linear theory by investigating the response of the materials to homogeneous deformations, pure bending of beams and small amplitudes of acoustic waves. Nunziato and Cowin have established a theory for the behavior of porous solids in which the skeletal or matrix materials are elastic and the interstices are voids of material.

Beskos and Aifantis [13] presented the theory of consolidation with double porosity-II and obtained the analytical solutions to two boundary value problems. Khalili and Valliappan [14] studied the unified theory of flow and deformation in double porous media. Khalili and Selvadurai [15] presented a fully coupled constitutive model for thermo-hydro-mechanical analysis in elastic media with double porosity structure. Various authors [16-21] investigated some problems on elastic solids, viscoelastic solids and thermoelastic solids with double porosity.

Iesan and Quintanilla [22] used the Nunziato-Cowin theory of materials with voids to derive a theory of thermoelastic solids, which have a double porosity structure. This theory is not based on Darcy's law. In contrast with the classical theory of elastic materials with the double porosity, the double porosity structure in the case of equilibrium is influenced by the displacement field.

Youseff [23-25] investigated some problems of infinite body with a cylindrical cavity and spherical cavity in generalized thermoelasticity. Allam et al [26] considered the model of generalized thermoelasticity proposed by Green and Naghdi, to study the electromagneto-thermoelastic interactions in an infinite perfectly conducting body with a spherical cavity. Abd-Alla and Abo-Dahab [27] studied the effect of rotation and initial stress on an infinite generalized magneto-thermoelastic diffusion body with a spherical cavity. Zenkour and Abouelregal [28] studied the effects of phase-lags in a thermoviscoelastic orthotropic continuum with a cylindrical hole and variable thermal conductivity.

The present paper deals with thermoelastic interactions in an infinite double porous thermoelastic body with a spherical cavity subjected to moving heat source in context

of Lord-Shulman theory of thermoelasticity. Laplace transform has been applied to find the expressions for the components of stress and temperature distribution. The resulting quantities are obtained in the physical domain by using a numerical inversion technique. Variation of radial stress, equilibrated stresses and temperature distribution against radial distance are depicted graphically to show the effect of heat source velocity and relaxation time parameters. Some particular cases have also been deduced from the present investigation.

## 2. Governing equations

Following Iesan and Quintanilla [22] and Lord and Shulman [1]; the constitutive relations and field equations for homogeneous isotropic thermoelastic material with double porosity structure in the absence of body forces and extrinsic equilibrated body forces can be written as :

### Constitutive Relations :

$$t_{ij} = \lambda e_{rr} \delta_{ij} + 2\mu e_{ij} + b\delta_{ij}\varphi + d\delta_{ij}\psi - \beta\delta_{ij}T \tag{1}$$

$$\sigma_i = \alpha\varphi_{,i} + b_1\psi_{,i} \tag{2}$$

$$\chi_i = b_1\varphi_{,i} + \gamma\psi_{,i} \tag{3}$$

### Equation of motion :

$$\mu\nabla^2 u_i + (\lambda + \mu) u_{j,j} + b\varphi_{,i} + d\psi_{,i} - \beta T_{,i} = \rho \ddot{u}_i, \tag{4}$$

### Equilibrated Stress Equations of motion :

$$\alpha\nabla^2 \varphi + b_1\nabla^2 \psi - bu_{r,r} - \alpha_1\varphi - \alpha_3\psi + \gamma_1 T = \kappa_1 \ddot{\varphi}, \tag{5}$$

$$b_1\nabla^2 \varphi + \gamma\nabla^2 \psi - du_{r,r} - \alpha_3\varphi - \alpha_2\psi + \gamma_2 T = \kappa_2 \ddot{\psi}, \tag{6}$$

### Equation of heat conduction :

$$\left(1 + \tau_0 \frac{\partial}{\partial t}\right) \left(\beta T_0 \dot{u}_{j,j} + \gamma_1 T_0 \dot{\varphi} + \gamma_2 T_0 \dot{\psi} + \rho C^* \dot{T} - Q\right) = K^* \nabla^2 T \tag{7}$$

where  $\lambda$  and  $\mu$  are Lamé's constants,  $\rho$  is the mass density;  $\beta = (3\lambda + 2\mu) \alpha_t$ ;  $\alpha_t$  is the linear thermal expansion;  $C^*$  is the specific heat at constant strain,  $u_i$  is the displacement

components;  $t_{ij}$  is the stress tensor;  $\kappa_1$  and  $\kappa_2$  are coefficients of equilibrated inertia;  $\sigma_i$  is the components of the equilibrated stress vector associated to pores;  $\chi_i$  is the components of the equilibrated stress vector associated to fissures;  $\varphi$  is the volume fraction field corresponding to pores  $\psi$  and is the volume fraction field corresponding to fissures;  $K^*$  is the coefficient of thermal conductivity;  $Q$  is the heat source;  $\tau_0$  is the thermal relaxation time,  $\kappa_1$  and  $\kappa_2$  are coefficients of equilibrated inertia  $b, d, b_1, \gamma, \gamma_1, \gamma_2$  and are constitutive coefficients;  $\delta_{ij}$  is the Kronecker's delta;  $T$  is the temperature change measured from the absolute temperature  $T_0$  ( $T_0 \neq 0$ ); a superposed dot represents differentiation with respect to time variable  $t$ .

We take the moving heat source as :

$$Q = Q_0 H(r - R) \frac{\delta(r - vt)}{r} \tag{8}$$

where  $H(*)$  is the Heaviside unit step function,  $Q_0$  is the heat source strength and  $v$  is its velocity.

### 3. Formulation of the problem

We consider a perfectly conducting thermoelastic infinite body with double porosity having spherical cavity occupying the region  $R \leq r < \infty$  of an isotropic homogeneous medium. The spherical polar coordinates  $(r, \vartheta, \phi)$  are taken for any representative point of the body at time  $t$  and the origin of the coordinate system is at the centre of the spherical cavity. All the variables considered will be functions of the radial distance  $r$  and the time  $t$ . The initial conditions are given by

$$u = 0 = \dot{u}, \quad \varphi = 0 = \dot{\varphi}, \quad \psi = 0 = \dot{\psi}, \quad T = 0 = \dot{T} \quad \text{at } t = 0 \tag{9}$$

Due to spherical symmetry, the displacements components are of the form

$$u_r = u(r, t), \quad u_\vartheta = u_\phi = 0 \tag{10}$$

The components of stress tensor for a spherical symmetric system are

$$t_{rr} = 2\mu \frac{\partial u}{\partial r} + \lambda e + b\varphi + d\psi - \beta T \tag{11}$$

$$t_{\vartheta\vartheta} = 2\mu \frac{u}{r} + \lambda e + b\varphi + d\psi - \beta T \tag{12}$$

$$t_{r\vartheta} = t_{r\phi} = t_{\vartheta\phi} = 0 \tag{13}$$

$$\sigma_r = \alpha \frac{\partial \varphi}{\partial r} + b_1 \frac{\partial \psi}{\partial r} \tag{14}$$

$$\chi_r = b_1 \frac{\partial \varphi}{\partial r} + \gamma \frac{\partial \psi}{\partial r} \tag{15}$$

where

$$e = e_{rr} + e_{\vartheta\vartheta} + e_{\phi\phi} = \frac{\partial u}{\partial r} + \frac{2u}{r}, \tag{16}$$

$$e_{rr} = \frac{\partial u}{\partial r}, \quad e_{\vartheta\vartheta} = e_{\phi\phi} = \frac{u}{r}, \quad e_{r\vartheta} = e_{r\phi} = e_{\vartheta\phi} = 0 \tag{17}$$

We introduce the non-dimensional quantities as :

$$r' = \frac{\omega_1}{c_1} r, \quad u' = \frac{\omega_1}{c_1} u, \quad t'_{ij} = \frac{t_{ij}}{\beta T_0}, \quad \varphi' = \frac{\kappa_1 \omega_1^2}{\alpha_1} \varphi, \quad \psi' = \frac{\kappa_1 \omega_1^2}{\alpha_1} \psi$$

$$T' = \frac{T}{T_0}, \quad t' = \omega_1 t, \quad \sigma'_i = \left(\frac{c_1}{\alpha \omega_1}\right) \sigma_i, \quad \chi'_i = \left(\frac{c_1}{\alpha \omega_1}\right) \chi_i, \quad \tau'_0 = \omega_1 \tau_0, \quad Q'_0 = \frac{c_1 Q_0}{K^* \omega_1 T_0}$$

where  $c_1^2 = \frac{\lambda+2\mu}{\rho}$ ,  $\omega_1 = \frac{\rho C^* c_1^2}{K^*}$

Making use of dimensionless quantities given by (17) on Eqs. (4)-(7) and with the aid of Eqs. (8) and (16) yield (dropping primes for convenience)

$$\frac{\partial e}{\partial r} + a_1 \frac{\partial \varphi}{\partial r} + a_2 \frac{\partial \psi}{\partial r} - a_3 \frac{\partial T}{\partial r} = \frac{\partial^2 u}{\partial t^2} \tag{18}$$

$$a_4 \nabla^2 \varphi + a_5 \nabla^2 \psi - a_6 e - a_7 \varphi - a_8 \psi + a_9 T = \frac{\partial^2 \varphi}{\partial t^2} \tag{19}$$

$$a_{10} \nabla^2 \varphi + a_{11} \nabla^2 \psi - a_{12} e - a_{13} \varphi - a_{14} \psi + a_{15} T = \frac{\partial^2 \psi}{\partial t^2} \tag{20}$$

$$\left(1 + \tau_0 \frac{\partial}{\partial t}\right) \left(a_{16} \frac{\partial e}{\partial t} + a_{17} \frac{\partial \varphi}{\partial t} + a_{18} \frac{\partial \psi}{\partial t} + \frac{\partial T}{\partial t} - \frac{Q_0 H(r-R) \delta(r-\nu t)}{r}\right) = \nabla^2 T \tag{21}$$

where

$$a_1 = \frac{b\alpha_1}{\rho c_1^2 \kappa_1^2 \omega_1^2}, \quad a_2 = \frac{d\alpha_1}{\rho c_1^2 \kappa_1^2 \omega_1^2}, \quad a_3 = \frac{\beta T_0}{\rho c_1^2}, \quad a_4 = \frac{\alpha}{\kappa_1 c_1^2}, \quad a_5 = \frac{b_1}{\kappa_1 c_1^2}, \quad a_6 = \frac{b}{\alpha_1}, \quad a_7 = \frac{\alpha_1}{\kappa_1 \omega_1^2},$$

$$a_8 = \frac{\alpha_3}{\kappa_1 \omega_1^2}, \quad a_9 = \frac{\gamma_1 T_0}{\alpha_1}, \quad a_{10} = \frac{b_1}{\kappa_2 c_1^2}, \quad a_{11} = \frac{\gamma}{\kappa_2 c_1^2}, \quad a_{12} = \frac{d\kappa_1}{\kappa_2 \alpha_1}, \quad a_{13} = \frac{\alpha_3}{\kappa_2 \omega_1^2}, \quad a_{14} = \frac{\alpha_2}{\kappa_2 \omega_1^2},$$

$$a_{15} = \frac{\gamma_2 T_0 \kappa_1}{\alpha_1 \kappa_2}, \quad a_{16} = \frac{\beta c_1^2}{\rho C^*}, \quad a_{17} = \frac{\gamma_1 \alpha_1 c_1^2}{K^* \kappa_1 \omega_1^3}, \quad a_{18} = \frac{\gamma_2 \alpha_1 c_1^2}{K^* \kappa_1 \omega_1^3}$$

#### 4. Solution in the Laplace transform domain

Applying the Laplace transform defined by

$$\bar{f}(s) = L[f(t)] = \int_0^\infty f(t) e^{-st} dt \tag{22}$$

on the Eqs. (18)-(21), after some simplifications, we obtain

$$[\nabla^8 + B_1\nabla^6 + B_2\nabla^4 + B_3\nabla^2 + B_4] \bar{e} = \frac{f_1}{r} e^{-(s/\nu)r} \tag{23}$$

$$[\nabla^8 + B_1\nabla^6 + B_2\nabla^4 + B_3\nabla^2 + B_4] \bar{\varphi} = \frac{f_2}{r} e^{-(s/\nu)r} \tag{24}$$

$$[\nabla^8 + B_1\nabla^6 + B_2\nabla^4 + B_3\nabla^2 + B_4] \bar{\psi} = \frac{f_3}{r} e^{-(s/\nu)r} \tag{25}$$

$$[\nabla^8 + B_1\nabla^6 + B_2\nabla^4 + B_3\nabla^2 + B_4] \bar{T} = \frac{f_4}{r} e^{-(s/\nu)r} \tag{26}$$

$B_i, f_i ; i = 1, 2, 3, 4$  are given in the appendix.

Therefore, the solutions of the Eqs. (23)-(26), which is bounded at infinity, are given by

$$\bar{e} = \frac{A_1}{r} e^{-m_1 r} + \frac{A_2}{r} e^{-m_2 r} + \frac{A_3}{r} e^{-m_3 r} + \frac{A_4}{r} e^{-m_4 r} + \frac{D_1}{r} e^{-(s/\nu)r} \tag{27}$$

$$\bar{\varphi} = g_{11} \frac{A_1}{r} e^{-m_1 r} + g_{12} \frac{A_2}{r} e^{-m_2 r} + g_{13} \frac{A_3}{r} e^{-m_3 r} + g_{14} \frac{A_4}{r} e^{-m_4 r} + \frac{D_2}{r} e^{-(s/\nu)r} \tag{28}$$

$$\bar{\psi} = g_{21} \frac{A_1}{r} e^{-m_1 r} + g_{22} \frac{A_2}{r} e^{-m_2 r} + g_{23} \frac{A_3}{r} e^{-m_3 r} + g_{24} \frac{A_4}{r} e^{-m_4 r} + \frac{D_3}{r} e^{-(s/\nu)r} \tag{29}$$

$$\bar{T} = g_{31} \frac{A_1}{r} e^{-m_1 r} + g_{32} \frac{A_2}{r} e^{-m_2 r} + g_{33} \frac{A_3}{r} e^{-m_3 r} + g_{34} \frac{A_4}{r} e^{-m_4 r} + \frac{D_4}{r} e^{-(s/\nu)r} \tag{30}$$

$g_{1i}, g_{2i}, g_{3i}, g_{4i}$  are given in the appendix.

$$D_i = \frac{f_i v^8}{s^8 + B_1 s^6 \nu^2 + B_2 s^4 \nu^4 + B_3 s^2 \nu^6 + B_4 \nu^8} ; i = 1, 2, 3, 4 \tag{31}$$

Substituting Eqs. (27) into Eq.(16), we obtain

$$\bar{u} = -\frac{D_1}{r^2} \left( \frac{v^2}{s^2} + r \frac{v}{s} \right) e^{-(s/v)r} - \frac{1}{r^2} \sum_{i=1}^4 \frac{A_i}{m_i^2} (1 + rm_i) e^{-m_i r}$$

Making use of Eqs.(27)-(30),(32) in Eqs.(11),(14) ,(15) and with the help of Eqs.(17) and (22), we obtain the corresponding expressions for radial stress and equilibrated stresses as

$$\bar{t}_{rr}(r, s) = G_5(r)e^{-(s/v)r} + \sum_{i=1}^4 \left( -\frac{p_1}{r} \left( m_i^2 + \frac{2m_i}{r} + \frac{2}{r^2} \right) + p_2 + p_3g_{1i} + p_4g_{2i} - g_{3i} \right) A_i(s)e^{-m_i r} \tag{32}$$

$$\bar{\sigma}_r(r, s) = -G_6(r)e^{-(s/v)r} - \sum_{i=1}^4 (p_5g_{1i} + p_6g_{2i}) \left( \frac{m_i r + 1}{r^2} \right) A_i(s)e^{-m_i r} \tag{33}$$

$$\bar{\chi}_r(r, s) = -G_7(r)e^{-(s/v)r} - \sum_{i=1}^4 (p_6g_{1i} + p_7g_{2i}) \left( \frac{m_i r + 1}{r^2} \right) A_i(s)e^{-m_i r} \tag{34}$$

where

$$p_1 = \frac{2\mu}{\beta T_0}, \quad p_2 = \frac{\lambda}{\beta T_0}, \quad p_3 = \frac{b\alpha_1}{\beta T_0 \kappa_1 \omega_1^2}, \quad p_4 = \frac{d\alpha_1}{\beta T_0 \kappa_1 \omega_1^2}, \quad p_5 = \frac{\alpha_1}{\kappa_1 \omega_1^2}, \quad p_6 = \frac{b_1 \alpha_1}{\alpha \kappa_1 \omega_1^2}, \quad p_7 = \frac{\gamma \alpha_1}{\alpha \kappa_1 \omega_1^2},$$

$$G_5 = -\frac{1}{r} \left( p_1 D_1 \left( \frac{2v^2}{s^2 r^2} + \frac{2v}{sr} + 1 \right) + p_2 D_1 + p_3 D_2 + p_4 D_3 - D_4 \right),$$

$$G_6 = (p_5 D_2 + p_6 D_3) \left( \frac{s}{vr} + \frac{1}{r^2} \right), \quad G_7 = (p_6 D_2 + p_7 D_3) \left( \frac{s}{vr} + \frac{1}{r^2} \right)$$

### 5. Boundary conditions

We consider that the bounding plane ( $r = R$ ) of the cavity is traction free and subjected to thermal shock as follows :

$$t_{rr}(R, t) = 0, \quad \sigma_r(R, t) = 0, \quad \chi_r(R, t) = 0, \quad T(R, t) = T_0 H(t) \tag{35}$$

After applying Laplace transform on Eq.(36), we get

$$\bar{t}_{rr}(R, s) = 0, \quad \bar{\sigma}_r(R, s) = 0, \quad \bar{\chi}_r(R, s) = 0, \quad \bar{T}(s, t) = \frac{T_0}{s} = F_1 \text{ (say)} \tag{36}$$

Substituting the values of  $\bar{t}_{rr}$ ,  $\bar{\sigma}_r$ ,  $\bar{\chi}_r$  and  $\bar{T}$  from Eqs. (30), (33)-(35) in the boundary conditions (37) yield the corresponding expressions for radial stress, equilibrated stresses and temperature distribution as

$$\bar{t}_{rr}(r, s) = \frac{1}{\Gamma} (H_{11}\Gamma_1 \exp(-m_1r) + H_{12}\Gamma_2 \exp(-m_2r) + H_{13}\Gamma_3 \exp(-m_3r) + H_{14}\Gamma_4 \exp(-m_4r)) \tag{37}$$

$$\bar{\sigma}_r(r, s) = \frac{1}{\Gamma} (H_{21}\Gamma_1 \exp(-m_1r) + H_{22}\Gamma_2 \exp(-m_2r) + H_{23}\Gamma_3 \exp(-m_3r) + H_{24}\Gamma_4 \exp(-m_4r)) \tag{38}$$

$$\bar{\chi}_r(r, s) = \frac{1}{\Gamma} (H_{31}\Gamma_1 \exp(-m_1r) + H_{32}\Gamma_2 \exp(-m_2r) + H_{33}\Gamma_3 \exp(-m_3r) + H_{34}\Gamma_4 \exp(-m_4r)) \tag{39}$$

$$\bar{T}(r, s) = \frac{1}{\Gamma} (H_{41}\Gamma_1 \exp(-m_1r) + H_{42}\Gamma_2 \exp(-m_2r) + H_{43}\Gamma_3 \exp(-m_3r) + H_{44}\Gamma_4 \exp(-m_4r)) \tag{40}$$

where

$$\Gamma = \begin{vmatrix} H_{11} & H_{12} & H_{13} & H_{14} \\ H_{21} & H_{22} & H_{23} & H_{24} \\ H_{31} & H_{32} & H_{33} & H_{34} \\ H_{41} & H_{42} & H_{43} & H_{44} \end{vmatrix} \tag{41}$$

$\Gamma_i$  ( $i = 1, 2, 3, 4$ ) are obtained by replacing  $i^{th}$  column of (41) with  $[F_2 \ F_3 \ F_4 \ (F_5 + F_1)]^T$

$$\begin{aligned} H_{1i} &= \frac{p_1}{m_i^2} \left( \frac{m_i^2}{R} + \frac{2m_i}{R^2} + \frac{2}{R^3} \right) + p_2 + p_3g_{1i} + p_4g_{2i} - g_{3i}, \\ H_{2i} &= \left( \frac{m_i R + 1}{R^2} \right) (p_5g_{1i} + p_6g_{2i}), \quad H_{3i} = \left( \frac{m_i R + 1}{R^2} \right) (p_6g_{1i} + p_7g_{2i}), \quad H_{4i} = g_{3i}, \\ F_2 &= \frac{1}{R} \left( p_1D_1 \left( \frac{2v^2}{s^2R^2} + \frac{2v}{sR} + 1 \right) + p_2D_1 + p_3D_2 + p_4D_3 - D_4 \right) e^{-(s/v)R}, \\ F_3 &= (p_5D_2 + p_6D_3) \left( \frac{s}{vR} + \frac{1}{R^2} \right) e^{-(s/v)R}, \\ F_4 &= (p_6D_2 + p_7D_3) \left( \frac{s}{vR} + \frac{1}{R^2} \right) e^{-(s/v)R}, \quad F_5 = \frac{D_4}{R} e^{-(s/v)R} \end{aligned}$$

### 6. Particular cases

Case 6.1 If  $\tau_0 = 0$ , in Eqs. (38)-(41) yield the corresponding expressions for an infinite thermoelastic double porous body with a spherical cavity in the context of coupled theory of thermoelasticity.

Case 6.2 If  $b_1 = \alpha_3 = \gamma = \alpha_2 = \gamma_2 = d \rightarrow 0$  in Eqs.(38)-(41), we obtain the corresponding expressions for an infinite thermoelastic single porous body with a spherical cavity.

## 7. Inversion of the Laplace domain

In order to invert the Laplace transform, we adopt a numerical inversion method based on a Fourier series expansion [29]

By this method the inverse  $f(t)$  of the Laplace transform  $\bar{f}(s)$  is approximated by

$$f(t) = \frac{e^{\eta t}}{t_1} \left[ \frac{1}{2} \bar{f}(\eta) + \operatorname{Re} \sum_{k=1}^N \bar{f} \left( \eta + \frac{ik\pi}{t_1} \right) \exp \left( \frac{ik\pi t}{t_1} \right) \right], \quad 0 < t_1 < 2t$$

where  $N$  is sufficiently large integer representing the number of terms in the truncated Fourier series, chosen such that

$$f(t) = \exp(\eta t) \operatorname{Re} \left[ \bar{f} \left( \eta + \frac{iN\pi}{t_1} \right) \exp \left( \frac{iN\pi t}{t_1} \right) \right] \leq \varepsilon_1$$

where  $\varepsilon_1$  is a prescribed small positive number that corresponds to the degree of accuracy required. The parameter  $t_1$  is a positive free parameter that must be greater than the real part of all the singularities of  $\bar{f}(s)$ . The optimal choice of  $t_1$  was obtained to the criterion described in [29].

## 8. Numerical results and discussion

The material chosen for the purpose of numerical computation is copper, whose physical data is given by Sherief and Saleh [30] as,

$$\lambda = 7.76 \times 10^{10} Nm^{-2}, \quad C^* = 3.831 \times 10^3 m^2 s^{-2} K^{-1}, \quad \mu = 3.86 \times 10^{10} Nm^{-2}, \\ K^* = 3.86 \times 10^3 N s^{-1} K^{-1}, \quad T_0 = 293 K, \quad \alpha_t = 1.78 \times 10^{-5} K^{-1}, \quad \rho = 8.954 \times 10^3 Kgm^{-3}$$

The double porous parameters are taken as,

$$\alpha_2 = 2.4 \times 10^{10} Nm^{-2}, \quad \alpha_3 = 2.5 \times 10^{10} Nm^{-2}, \quad \gamma = 1.1 \times 10^{-5} N, \quad \alpha = 1.3 \times 10^{-5} N$$

$$\gamma_1 = 0.16 \times 10^5 Nm^{-2}, \quad b_1 = 0.12 \times 10^{-5} N, \quad d = 0.1 \times 10^{10} Nm^{-2}$$

$$\gamma_2 = 0.219 \times 10^5 Nm^{-2}, \quad \kappa_1 = 0.1456 \times 10^{-12} Nm^{-2} s^2, \quad b = 0.9 \times 10^{10} Nm^{-2}$$

$$\alpha_1 = 2.3 \times 10^{10} Nm^{-2}, \quad \kappa_2 = 0.1546 \times 10^{-12} Nm^{-2} s^2$$

The other non-dimensional parameters are taken as

$$Q_0 = 5.0, \quad t = 0.2, \quad R = 1.0, \quad \tau_0 = 0.1$$

The software MATLAB has been used to find the values of radial stress  $t_{rr}$ , equilibrated stresses  $\sigma_r$ ,  $\chi_r$  and temperature distribution  $T$ . The variations of these values with respect to radial distance  $r$  have been shown in figures (1)-(8). In figs.1-4, effect of thermal relaxation time is shown graphically. In all these figures, solid line and small dashed line correspond to Lord-Shulman(LS) theory of thermoelasticity for to coupled theory (CT) of thermoelasticity respectively. Also, the effect of heat source velocity is depicted graphically in figs. 5-8 for different values of heat source velocity parameters  $\nu = 0.2, 0.4$  and  $0.6$ .

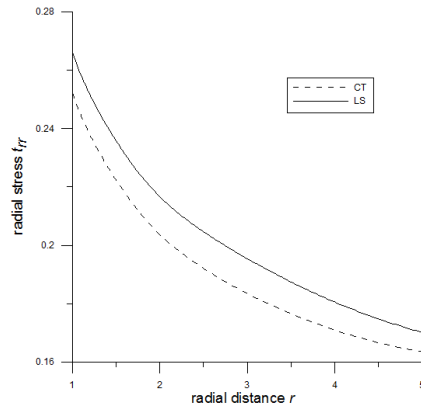


Fig. 1 – Variation of radial stress  $t_{rr}$  w.r.t. radial radial distance  $r$ .

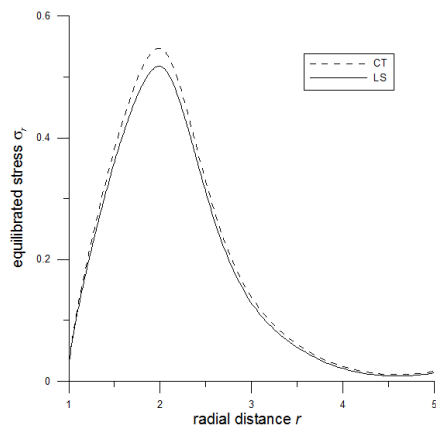


Fig. 2 – Variation of equilibrated stress  $\sigma_r$  w.r.t. radial distance  $r$ .

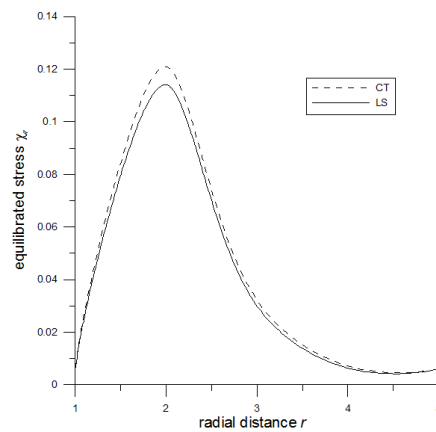


Fig. 3 – Variation of equilibrated stress  $\chi_r$  w.r.t. radial radial distance  $r$ .

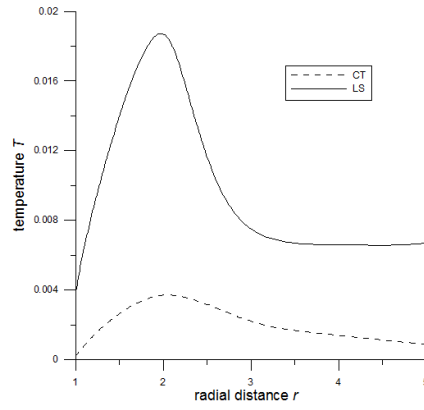


Fig. 4 – Variation of temperature distribution  $T$  w.r.t. radial distance  $r$ .

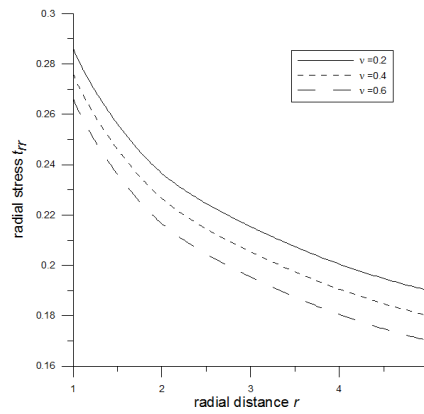


Fig. 5 – Variation of radial stress  $t_{rr}$  w.r.t. radial radial distance  $r$ .

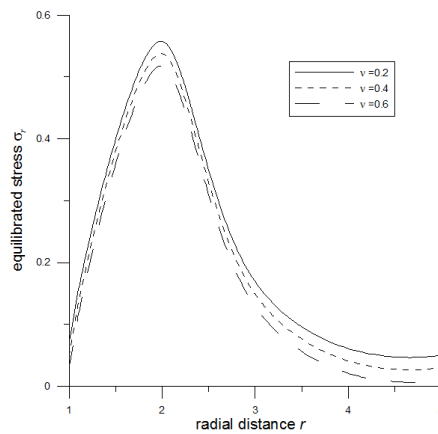
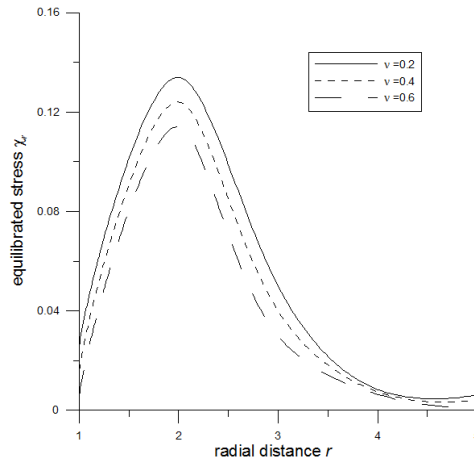
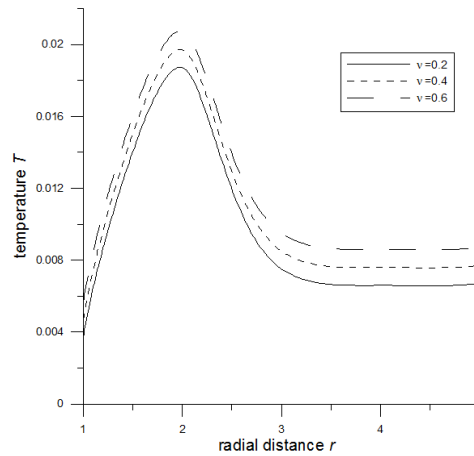


Fig. 6 – Variation of equilibrated stress  $\sigma_r$  w.r.t. radial distance  $r$ .



**Fig. 7** – Variation of equilibrated stress  $\chi_r$  w.r.t. radial  $r$ .



**Fig. 8** – Variation of temperature distribution  $T$  w.r.t. radial distance  $r$ .

Fig.1 shows that radial stress  $t_{rr}$  is maximum at the boundary surface of the spherical cavity and it decreases monotonically with increase in radial distance  $r$ . Also, it is found that the magnitude values of  $t_{rr}$  increases due to relaxation time parameter. The values of  $t_{rr}$  are more for LS theory in comparison to CT theory of thermoelasticity . From figs.2 and 3 , it is clear that equilibrated stresses  $\sigma_r$  and  $\chi_r$  increases for  $1 \leq r \leq 2$  and then decreases onwards as increases. The magnitude values of  $\sigma_r$  and  $\chi_r$  decreases due to relaxation time. It is evident that the values of  $\sigma_r$  and  $\chi_r$  are more for CT theory as compared to the values for LS theory of thermoelasticity. Fig.4 depicts that the values of temperature distribution  $T$  increase monotonically for  $1 \leq r \leq 2$ , decrease monotonically for  $2 \leq r \leq 3$  and then decrease very slowly and steadily with the increase in the value of radial distance  $r$ . It is also found that relaxation time parameter increases the values of  $T$ , the magnitude value of are more incase of LS theory than that of CT theory of

thermoelasticity.

Fig.5 represents that radial stress  $t_{rr}$  decreases monotonically with increase in radial distance  $r$ . Also, it is found that the magnitude values of  $t_{rr}$  decrease with the increase in the values of heat source velocity  $\nu$ . Figs.6 and 7 shows that equilibrated stresses  $\sigma_r$  and  $\chi_r$  increase for  $1 \leq r \leq 2$  and then start decreasing as  $r > 2$ . It is also clear that the magnitude values of  $\sigma_r$  and  $\chi_r$  decrease as the value of heat source velocity  $\nu$  increases. Fig.8 depicts that the values of temperature distribution  $T$  increase monotonically for  $1 \leq r \leq 2$ , decrease monotonically for  $2 \leq r \leq 3$  and then become almost stationary as  $r > 3$ . Also. it is found that as the velocity of heat source increases, the magnitude values of temperature distribution  $T$  increases also increases.

## 9. Concluding remarks

In this work, we have studied the problem of infinite thermoelastic medium with double porosity having spherical cavity in context of Lord-Shulman theory of thermoelasticity with one relaxation time subjected to moving heat source. Effect of thermal relaxation time and heat source velocity parameters are shown graphically on radial stress, equilibrated stresses and temperature distribution. All the field quantities are observed to be very sensitive towards the heat source velocity parameter. From figures, it is concluded that the magnitude values of radial stress and equilibrated stresses decrease with increase in the values of heat source velocity while a reverse trend is noticed in case of temperature distribution. The thermal relaxation time parameter has also a considerable effect on the all the physical quantities. The relaxation time parameter has both the increasing as well as decreasing effect on these quantities which shows that it is very important to take into account the relaxation time parameter.

This type of study is useful due to its application in geophysics and rock mechanics. The results obtained in this investigation should prove to be beneficial for the researchers working on the theory of thermoelasticity with double porosity structure. The introduction of double porous parameter to the thermoelastic medium represents a more realistic model for further studies.

## REFERENCES

- [1] Lord, H., Shulman, Y., 1967. A generalized dynamical theory of thermoelasticity, J. Mech. Phys. Solids 15, p. 299-309.
- [2] Biot, M.A., 1941. General theory of three-dimensional consolidation, J. Appl. Phys.12, p.155-164.
- [3] Barenblatt, G.I., Zheltov, I.P., Kochina, I. N., 1960. Basic Concept in the theory of seepage of homogeneous liquids in fissured rocks (strata), J. Appl. Math. Mech. 24, p. 1286-1303.
- [4] Aifantis, E. C., 1977. Introducing a multi –porous medium, Developments in Mechanics 8 , p. 209-211.
- [5] Aifantis, E. C., 1979. On the response of fissured rocks, Developments in Mechanics 10,p. 249-253.
- [6] Aifantis, E.C., The mechanics of diffusion in solids, T.A.M. Report No. 440, Dept. of Theor. Appl. Mech., University of Illinois, Urbana, Illinois (1980)

- [7] Aifantis, E.C., 1980. On the Problem of Diffusion in Solids, *Acta Mech.* 37, p. 265-296.
- [8] Wilson, R. K., Aifantis, E. C., 1984. On the theory of consolidation with double porosity, *Int. J. Engg. Sci.* 20(9), p. 1009-1035.
- [9] Khaled, M. Y., Beskos, D. E., Aifantis, E. C., 1984. On the theory of consolidation with double porosity-III, *Int. J. Numer. Anal. Meth. Geomech.* 8, p. 101-123.
- [10] Wilson, R. K., Aifantis, E. C., 1984. A Double Porosity Model for Acoustic Wave propagation in fractured porous rock, *Int. J. Engg. Sci.* 22 (8-10), p.1209-1227.
- [11] Nunziato, J.W., Cowin, S.C., 1979. A nonlinear theory of elastic materials with voids, *Arch. Rat. Mech. Anal.*, 72, p. 175-201.
- [12] Cowin, S.C., Nunziato, J. W., 1983. Linear elastic materials with voids, *J. Elasticity*, 13, p. 125-147.
- [13] Beskos, D. E., Aifantis, E. C., 1986. On the theory of consolidation with Double Porosity-II, *Int. J. Engg. Sci.* 24, p. 1697-1716
- [14] Khalili, N., Valliappan, S., 1996. Unified theory of flow and deformation in double porous media, *Eur. J. Mech. A, Solids.* 15, p. 321-336.
- [15] Khalili, N., Selvadurai, A. P. S., 2003. A Fully Coupled Constitutive Model for Thermo-hydro –mechanical Analysis in Elastic Media with Double Porosity, *Geophys. Res. Lett.* 30, p. 2268-2271.
- [16] Svanadze, M., 2005. Fundamental solution in the theory of consolidation with double porosity, *J. Mech. Behav. Mater.* 16, p. 123-130.
- [17] Svanadze, M., 2010. Dynamical Problems on the Theory of Elasticity for Solids with Double Porosity, *Proc. Appl. Math. Mech.* 10, p.209-310.
- [18] Svanadze, M., 2012. Plane Waves and Boundary Value Problems in the Theory of Elasticity for solids with Double Porosity, *Acta Appl. Math.* 122 ,p. 461-470.
- [19] Straughan, B. , 2013. Stability and Uniqueness in Double Porosity Elasticity, *Int. J. Eng. Sci.* 65,p. 1-8.
- [20] Svanadze, M., 2014. On the Theory of Viscoelasticity for materials with Double Porosity, *Disc. and Cont. Dynam. Syst. Ser. B.* 19(7), p. 2335-2352.
- [21] Svanadze, M., 2014. Uniqueness theorems in the theory of thermoelasticity for solids with double porosity, *Meccanica*, 49,p. 2099-2108.
- [22] Iesan, D., Quintanilla, R., 2014. On a theory of thermoelastic materials with a double porosity structure, *J. Therm. Stress.* 37, p. 1017-1036.
- [23] Youssef, H.M., 2005. Generalized thermoelasticity of an infinite body with a cylindrical cavity and variable material properties, *J. Therm. Stresses* 28, p.521–532.
- [24] Youssef, H. M., 2010. Generalized thermoelastic infinite medium with spherical cavity subjected to moving heat source, *Computational mathematics and modeling*, 21(2), p. 212-224.
- [25] Youssef, H. M., 2013. State space approach to two-temperature generalized thermoelasticity without energy dissipation of medium subjected to moving heat source, *Appl. Math. Mech.*, 34(1), p. 63-74.
- [26] Allam, M. N., Elsibai, K.A. , Abouelregal, A.E., 2010. Magneto-thermoelasticity for an infinite body with a spherical cavity and variable material properties without energy dissipation, *Int. J. Solids Struct.* 47, p. 2631–2638.
- [27] Abd-Alla, A. M., Abo-Dahab, S. M., 2012. Effect of Rotation and Initial Stress on an Infinite Generalized Magneto-Thermoelastic Diffusion Body with a Spherical Cavity,

- J. of Thermal Stresses 35, p. 892–912.
- [28] Zenkour, A. M., Abouelregal, A. E. , 2015. Effects of phase-lags in a thermoviscoelastic orthotropic continuum with a cylindrical hole and variable thermal conductivity, Arch. Mech., 67 (6) , p. 457–475.
- [29] Honig, G., Hirdes, U., 1984. A method for the numerical inversion of the Laplace transform, J. Comp. Appl. Math. 10, p.113-132.
- [30] Sherief, H., Saleh, H., 2005. A half space problem in the theory of generalized thermoelastic diffusion, Int. J. Solid. Struct. 42, p. 4484-4493.
- [31] Khalili, N., 2003. Coupling effects in double porosity media with deformable matrix, Geophys. Res. Lett. 30(22), DOI 10.1029/2003GL018544.

## Appendix

$$\begin{aligned}
 a_{19} &= s(1 + \tau_0 s), \quad a_{20} = s(1 + \tau_0 s)a_{16}, \quad a_{21} = s(1 + \tau_0 s)a_{17}, \quad a_{22} = s(1 + \tau_0 s)a_{18}, \\
 n_1 &= -(a_7 + s^2), \quad n_2 = -(a_{14} + s^2), \quad r_1 = a_5 a_{10} - a_4 a_{11}, \\
 r_2 &= a_4(a_{11} a_{19} - n_2) - a_{11} n_1 - a_7 a_{10} - a_5(a_{10} a_{19} + a_{13}), \\
 r_3 &= n_1(a_{11} a_{19} - n_2) + a_4(n_2 a_{19} - a_{15} a_{22}) + a_5(a_{13} a_{19} + a_{15} a_{21}) + \\
 &\quad a_7(a_{10} a_{19} + a_{13}) + a_9(a_{10} a_{22} - a_{11} a_{21}), \\
 r_4 &= n_1(n_2 a_{19} - a_{15} a_{22}) - a_8(a_{13} a_{23} + a_{15} a_{21}) - a_9(a_{13} a_{22} + n_2 a_{21}), \quad r_5 = a_6 a_{11} - a_5 a_{12}, \\
 r_6 &= -a_6(a_{11} a_{19} - n_2) + a_7 a_{12} + a_5(a_{19} a_{12} + a_{15} a_{20}) - a_9 a_{11} a_{20},
 \end{aligned}$$

$$\begin{aligned}
 r_7 &= -a_6(n_2 a_{19} - a_{15} a_{22}) - a_7(a_{12} a_{19} + a_{15} a_{20}) - a_8(a_{12} a_{22} + n_2 a_{20}), \\
 r_8 &= a_6 a_{10} - a_4 a_{12}, \quad r_9 = -a_6(a_{13} + a_{10} a_{19}) - n_1 a_{12} + a_4(a_{12} a_{19} + a_{15} a_{20}), \\
 r_{10} &= a_9(a_{13} a_{20} - a_{12} a_{21}) + n_1(a_{12} a_{19} + a_{15} a_{20}) + a_6(a_{13} a_{19} + a_{15} a_{21}), \\
 r_{11} &= a_{20}(a_4 a_{11} - a_5 a_{10}), \quad r_{12} = a_6(a_{11} a_{21} - a_{10} a_{22}) + a_{20}(n_1 a_{11} + a_7 a_{10}) \\
 &\quad + a_4(a_{12} a_{22} + n_2 a_{20}) + a_5(a_{13} a_{20} - a_{12} a_{21}), \\
 r_{13} &= a_7(a_{12} a_{21} - a_{13} a_{20}) + a_6(a_{13} a_{22} + n_2 a_{21}) + n_1(a_{12} a_{22} + n_2 a_{20}),
 \end{aligned}$$

$$\begin{aligned}
 B_1 &= (r_2 - s^2 r_1)/r_1, \quad B_2 = (r_3 - s^2 r_2 - a_1 r_5 + a_2 r_8 + a_3 r_{11})/r_1, \\
 B_3 &= (r_4 - s^2 r_3 - a_1 r_6 + a_2 r_9 + a_3 r_{12})/r_1, \quad B_4 = (-s^2 r_4 - a_1 r_7 + a_2 r_{10} + a_3 r_{13})/r_1,
 \end{aligned}$$

$$\begin{aligned}
 f_1 &= \zeta (r_1 s^6 + r_2 s^4 v^2 + r_3 s^2 v^4 + r_4 v^6)/\nu^6, \quad f_2 = -\zeta (r_5 s^4 + r_6 s^2 v^2 + r_7 v^4)/\nu^4 \\
 f_3 &= \zeta (r_8 s^4 + r_9 s^2 v^2 + r_{10} v^4)/\nu^6, \quad f_4 = \zeta (r_{11} s^4 + r_{12} s^2 v^2 + r_{13} v^4)/\nu^4, \quad \zeta = Q_0 H(r - R)/v,
 \end{aligned}$$

$$\begin{aligned}
 g_{1i} &= -\{r_5 m_i^4 + r_6 m_i^2 + r_7\} / \{r_1 m_i^6 + r_2 m_i^4 + r_4\}, \\
 g_{2i} &= \{r_8 m_i^4 + r_9 m_i^2 + r_{10}\} / \{r_1 m_i^6 + r_2 m_i^4 + r_3 m_i^2 + r_4\}, \\
 g_{3i} &= -\{r_{11} m_i^4 + r_{12} m_i^2 + r_{13}\} / \{r_1 m_i^6 + r_2 m_i^4 + r_3 m_i^2 + r_4\}; \quad i = 1, 2, 3, 4
 \end{aligned}$$